

AD A 1 0 6 9 9 8

12

LEVEL



RADC-TR-81-226
Final Technical Report
August 1981

weight

ULTRA-LIGHT MIRROR MANUFACTURING AND RADIATION RESPONSE STUDY

Eastman Kodak Company

Sponsored by
Defense Advanced Research Projects Agency (DoD)
ARPA Order No. 3503

APPROVED FOR PUBLIC RELEASE; DISTRIBUTION UNLIMITED

DTIC
ELECTE
NOV 5 1981
S
A

The views and conclusions contained in this document are those of the authors and should not be interpreted as necessarily representing the official policies, either expressed or implied, of the Defense Advanced Research Projects Agency or the U.S. Government.

MIC FILE COPY

ROME AIR DEVELOPMENT CENTER
Air Force Systems Command
Griffiss Air Force Base, New York 13441

81 11 04 068

This report has been reviewed by the RADC Public Affairs Office (PA) and is releasable to the National Technical Information Service (NTIS). At NTIS it will be releasable to the general public, including foreign nations.

RADC-TR-81-226 has been reviewed and is approved for publication.

APPROVED:



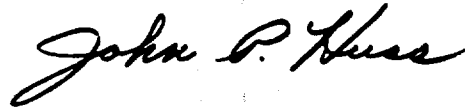
DORIS HAMILL, Capt, USAF
Project Engineer

APPROVED:



FRANK J. REHM
Technical Director
Surveillance Division

FOR THE COMMANDER:



JOHN P. HUSS
Acting Chief, Plans Office

If your address has changed or if you wish to be removed from the RADC mailing list, or if the addressee is no longer employed by your organization, please notify RADC (OCSE) Griffiss AFB NY 13441. This will assist us in maintaining a current mailing list.

Do not return copies of this report unless contractual obligations or notices on a specific document requires that it be returned.

ULTRA-LIGHTWEIGHT MIRROR MANUFACTURING
AND RADIATION RESPONSE STUDY

T.C. Fitzsimmons
David A. Crowe

Contractor: Eastman Kodak Company
Contract Number: F30602-81-C-0008
Effective Date of Contract: 6 November 1980
Contract Expiration Date: 31 March 1981
Short Title of Work: Radiation Response Study
Program Code Number: OL10
Period of Work Covered: 6 Nov 80 - 31 Mar 81

Principal Investigator: T.C. Fitzsimmons
Phone: 716 724-5579

Project Engineer: Doris Hamill, Capt, USAF
Phone: 315 330-3148

Approved for public release; distribution unlimited

This research was supported by the Defense Advanced Research Projects Agency of the Department of Defense and was monitored by Doris Hamill, Capt, USAF (OCSE), Griffiss AFB NY 13441 under Contract F30602-81-C-0008.

UNCLASSIFIED

SECURITY CLASSIFICATION OF THIS PAGE (When Data Entered)

REPORT DOCUMENTATION PAGE		READ INSTRUCTIONS BEFORE COMPLETING FORM
1. REPORT NUMBER RADC-TR-81-226	2. GOVT ACCESSION NO. AD-A206 998	3. RECIPIENT'S CATALOG NUMBER
4. TITLE (and Subtitle) ULTRA-LIGHTWEIGHT MIRROR MANUFACTURING AND RADIATION RESPONSE STUDY	5. TYPE OF REPORT & PERIOD COVERED Final Technical Report 6 Nov 80 - 31 Mar 81	6. PERFORMING ORG. REPORT NUMBER N/A
7. AUTHOR(s) T.C. Fitzsimmons David A. Crowe	8. CONTRACT OR GRANT NUMBER(s) F30602-81-C-0008 V V ARPA ORDER - 3573	
9. PERFORMING ORGANIZATION NAME AND ADDRESS Eastman Kodak Company (Apparatus Division) 901 Elmgrove Road Rochester NY 14050	10. PROGRAM ELEMENT, PROJECT, TASK AREA & WORK UNIT NUMBERS 62711E C5030109	
11. CONTROLLING OFFICE NAME AND ADDRESS Defense Advanced Research Projects Agency 1400 Wilson Blvd Arlington VA 22209	12. REPORT DATE August 1981	
14. MONITORING AGENCY NAME & ADDRESS (if different from Controlling Office) Rome Air Development Center (OCSE) Griffiss AFB NY 13441	13. NUMBER OF PAGES 126	15. SECURITY CLASS. (of this report) UNCLASSIFIED
16. DISTRIBUTION STATEMENT (of this Report) Approved for public release; distribution unlimited		15a. DECLASSIFICATION/DOWNGRADING SCHEDULE N/A
17. DISTRIBUTION STATEMENT (of the abstract entered in Block 20, if different from Report) Same		
18. SUPPLEMENTARY NOTES RADC Project Engineer: Doris Hamill, Capt, USAF		
19. KEY WORDS (Continue on reverse side if necessary and identify by block number) frit bonding lightweight mirrors space optics mirror blank fabrication ULE		
20. ABSTRACT (Continue on reverse side if necessary and identify by block number) This study investigates the requirements for making ultra-lightweight mirrors of Ultra-Low Expansion (ULE) fused silica by frit bonding. It includes a manufacturing assessment of the facilities needed to scale the mirror technology to 4 meters in diameter. It also includes a front surface flux loading thermal test of a .5M diameter frit bonded ULE mirror. The test was supported by detailed modeling and analysis.		

DD FORM 1 JAN 73 1473 EDITION OF 1 NOV 65 IS OBSOLETE

UNCLASSIFIED

SECURITY CLASSIFICATION OF THIS PAGE (When Data Entered)

403945

JB

TABLE OF CONTENTS

<u>Section</u>	<u>Title</u>	<u>Page</u>
	<i>Title Page</i>	<i>i</i>
	<i>Table of Contents.</i>	<i>ii</i>
	<i>List of Figures.</i>	<i>iii</i>
	<i>List of Tables</i>	<i>vi</i>
1.0	INTRODUCTION	1
1.1	Program.	1
1.2	Background	2
1.2.1	Ultra Lightweight Mirror Technology.	2
1.2.2	Lightweight Mirror Manufacturing	3
1.2.3	Frit Material and Processing	4
1.3	Summary.	8
1.3.1	Frit-Bonding Process Evaluation.	8
1.3.2	Mirror Blank Handling and Furnacing Analysis	8
1.3.3	Heat Flux Irradiation Testing.	8
2.0	CORNING GLASS WORKS SUBCONTRACT.	10
2.1	Frit Tasks	10
2.1.1	Frit Material Development.	10
2.1.2	Frit-Bonding Evaluation.	13
2.1.3	Conclusion and Recommendations	29
2.2	Mirror Blank Handling and Furnacing Analysis	30
2.2.1	Mirror Component Handling Analysis	30
2.3	Heat Load Testing and Analysis	43
2.3.1	0.5-Meter Performance Analysis	43
2.3.2	0.5-Meter Mirror Heat Load Test Configuration Evaluation	52
2.3.3	0.5-Meter Mirror Heat Load Test.	67
2.3.4	Heat Load Test Data Correlation and Scaling.	68
APPENDIX A	<i>Comparison by Couple Number.</i>	80
APPENDIX B	<i>Composite and Individual</i>	87
APPENDIX C	<i>Composite and Individual</i>	95
APPENDIX D	<i>Comparison by Clock Position</i>	103

<input type="checkbox"/> Accession Ref.	<input checked="" type="checkbox"/>
<input type="checkbox"/> NTIS G-81	<input checked="" type="checkbox"/>
<input type="checkbox"/> DTIC TAB	<input checked="" type="checkbox"/>
<input type="checkbox"/> Unannounced	
<input type="checkbox"/> Justification	
Pre	
Distrib	
Availability	
Dist	

A

LIST OF FIGURES

<u>Figure</u>	<u>Title</u>	<u>Page</u>
1.1-1	Work Breakdown Structure	1
1.2.1-1	Classical Lightweight Mirrors vs Ultra Lightweight Frit-Bonded Mirrors.	2
1.2.2-1	Corning Glass Works Mirror Fabrication Process	3
1.2.3-1	Kodak 0.5-Meter Diameter Ultra Lightweight Frit-Bonded Mirror	6
2.1.1-1	Mismatch vs Firing Plateau for Single and Double Fired U-A Frit	10
2.1.1-2	Channel-Strip Method for Core-Plate Bonding.	11
2.1.1-3	Apparatus Showing.	12
2.1.1-4	Photograph of Apparatus.	12
2.1.1-5	Force-Displacement Curves for Various Extraction Rates in the Frit Dip Process.	13
2.1.1-6	Peak Normal Extraction Force vs Extraction Rate for Frit Dip Process	13
2.1.2-1	Sealing Furnace.	14
2.1.2-2	Ell Maker.	16
2.1.2-3	Core-Maker Assembly Table.	17
2.1.2-4	Plate Handling Device.	18
2.1.2-5	Core Handling Device	18
2.1.2-6	Plate Handling into Turnover Yoke.	18
2.1.2-7	Plate Turnover Device.	18
2.1.2-8	Plate Acid Etch.	19
2.1.2-9	Core Acid Etch	19
2.1.2-10	Acid Etching System.	20
2.1.2-11	Frit Dip Application	22
2.1.2-12	Bottom Plate Assembly in Furnace	22
2.1.2-13	Core Assembly in Furnace	23
2.1.2-14	Top Plate Assembly in Furnace.	23
2.1.2-15	Frit Application Equipment - Automatic	24
2.1.2-16	Electric Frit Firing Furnace	25
2.2.1-1	Location of Vac-U-Lift Pads.	30
2.2.1-2	Cross Section of Vacuum Pad.	31
2.2.1-3	Glass Stress Versus Pad Radius and Lifting Force Versus Pad Radius.	32
2.2.1-4	Optimum Ring Support for 4.0-Meter Facesheet	33
2.2.1-5	Stress Model Flat Plate.	34
2.2.1-6	Core Lifting Method.	36
2.2.1-7	Coarse Model of Core Plate for Stress Calculation.	37
2.2.1-8	Refined Model of Core Plate for Stress Calculation	37
2.2.1-9	Model of Core Structure.	38
2.2.1-10	Out-of-Plane Force Caused by Misalignment.	38
2.2.1-11	Major Principal Stress Versus Direction of Applied Load	39
2.2.1-12	Distributed Stiffness Model of Core Structure.	39

<u>Figure</u>	<u>Title</u>	<u>Page</u>
2.3.1-1	NASTRAN Single Cell Model.	44
2.3.1-2	SATAN Single Cell Model.	44
2.3.1-3	Thermal Model Computer Plot.	45
2.3.1-4	Thermal Model Grid Point Numbering	45
2.3.1-5	Thermal Model Mask Area Details.	46
2.3.1-6	Structural Model Computer Plot	46
2.3.1-7	Structural Model Top Surface Detail.	47
2.3.1-8	Top Surface Temperatures--60 Seconds	48
2.3.1-9	Top Surface Temperatures Final Run--80 Seconds	48
2.3.1-10	Temperature Profiles Z-Direction 60 Seconds.	48
2.3.1-11	Temperature Profiles Z-Direction 80 Seconds.	48
2.3.1-12	Surface Deflection - Gravity Load.	49
2.3.1-13	Surface Deflections - 80 Second Exposure	49
2.3.1-14	Top Surface Deformations	49
2.3.2-1	ULE™ Ultra Lightweight Frit-Bonded Mirror.	52
2.3.2-2	0.5-Meter Diameter Frit-Bonded ULE Mirror.	53
2.3.2-3	Irradiation Response Test Configuration.	53
2.3.2-4	Mirror Test Position (First Orientation Baseline).	55
2.3.2-5	Irradiation Response Test.	56
2.3.2-6	Irradiation Response Test.	57
2.3.2-7	0.5-Meter Mirror Irradiation Test.	58
2.3.2-8	(a) Radial ΔT Front Plate, First Orientation, and (b) Radial ΔT Front Plate, Second Orientation.	59
2.3.2-9	(a) Radial ΔT Back Plate, First Orientation, and (b) Radial ΔT Back Plate, Second Orientation	59
2.3.2-10	(a) Axial ΔT Front & Back Plate, First Orientation Position 3 (b) Axial ΔT Front & Back Plate, First Orientation Position 9	60
2.3.2-11	(a) Axial ΔT Front & Back Plate, Second Orientation Position 6 (b) Axial ΔT Front & Back Plate, Second Orientation Position 12.	60
2.3.2-12	Irradiation Simulator.	63
2.3.2-13	Absorptance and Spectral Radiance Versus Wavelength 0.5-Meter Mirror Coating Irradiated by Tungsten Filament-Argon Quartz Lamps.	63
2.3.2-14	0.5-Meter Test Stand	66
2.3.2-15	0.5-Meter Mirror Irradiation Response Test Configuration.	67
2.3.4-1	Thermocouple Number 1 Cooldown	71
2.3.4-2	Faceplate Temperature Predicted by SATAN Single Cell Model	73
2.3.4-3	Faceplate Temperatures Predicted by SATAN Thermal Model (a) 2.4-Meter Mirror (b) 4.0-Meter Mirror.	78

<u>Figure</u>	<u>Title</u>	<u>Page</u>
<i>APPENDIX A</i> A-1 - A-10	Irradiation Response Tests	81
<i>APPENDIX B</i> B-1 - B-11	Irradiation Response Tests	87
<i>APPENDIX C</i> C-1 - C-11	Irradiation Response Tests	95
<i>APPENDIX D</i> D-1 - D-4	Irradiation Response Tests	103

LIST OF TABLES

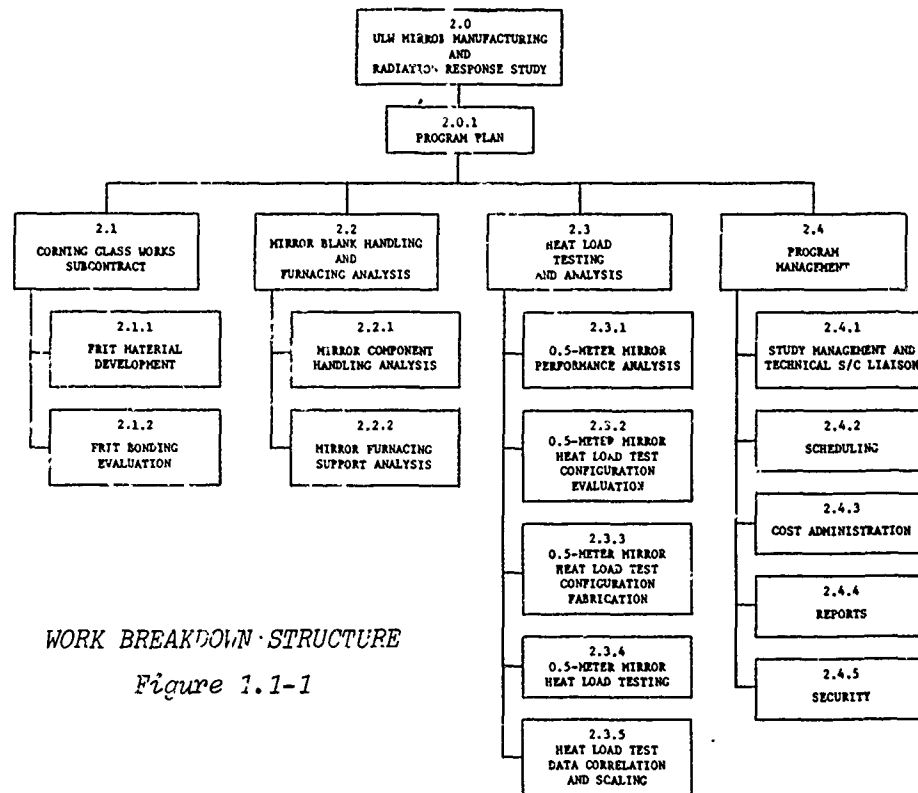
<u>Table</u>	<u>Title</u>	<u>Page</u>
1.2.3-1	Classical Versus Ultra Lightweight Mirror Blank Comparison	6
1.2.3-2	Ultra Lightweight Mirror Frit-Bonded Stability Test Program	7
2.2.1-1	4-Meter Monolithic Mirror Design	30
2.2.1-2	Core Stress Convergence Test	37
2.2.1-3	Core Stresses-Point Loads at Vent Hole	38
2.2.1-4	Core Reaction Forces	39
2.3.2-1	Irradiation Response Tests	54
2.3.2-2	Irradiation Response Test Thermal Data Radial Temperature, 80-Second Irradiation	61
2.3.2-3	Irradiation Response Test Thermal Data Axial Temperatures 80-Second Irradiation	61
2.3.2-4	Irradiation Heat Flux Uniformity Survey.	64
2.3.2-5	Irradiation Response Test Thermocouple Calibration . . .	65
2.3.3-1	Optical Data Summary	67
2.3.3-2	DPEA Evaluation.	68
2.3.3-3	4-Orientation Air Bag Test at Kodak.	68
2.3.4-1	Zernike Aberration Analysis, Analytical Results for a One-g Load Case and a V-Block Support.	69
2.3.4-2	Zernike Aberration Analysis, Test Results for a One-g Load Case and a V-Block Support.	69
2.3.4-3	Comparison of Predicted and Measured Temperature Increases.	71
2.3.4-4	Test Results	77
2.3.4-5	Comparison of Predicted and Measured Peak-to-Valley Deflections	77
2.3.4-6	2.4-Meter Monolithic Mirror Design	78
2.3.4-7	Predicted Peak-to-Valley Deflection of 2.4-Meter and 4.0-Meter Mirrors.	79

1.0 INTRODUCTION

This document constitutes the final report for the Ultra Lightweight Mirror Manufacturing and Radiation Response Study, sponsored by the Defense Advanced Research Projects Agency and conducted by Eastman Kodak Company under contract to Rome Air Development Center (RADC).

1.1 PROGRAM

To achieve the objective of the Ultra Lightweight Mirror Manufacturing and Radiation Response Study Statement of Work, a 21-week study was conducted by Eastman Kodak Company. This study centered in three major areas; frit-bonding process evaluation, mirror blank handling and furnacing analysis, and heat flux irradiation testing of a 0.5-meter diameter ultra lightweight mirror. The work breakdown structure for this study is shown in Figure 1.1-1.



WORK BREAKDOWN STRUCTURE

Figure 1.1-1

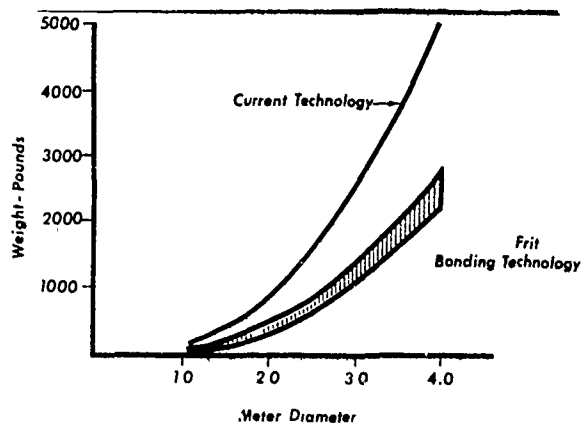
1.2 BACKGROUND

1.2.1 Ultra Lightweight Mirror Technology

In 1978, Kodak initiated a high technology mirror design program, in concert with Corning Glass Works, which culminated in the fabrication of a 0.5-meter diameter, ultra lightweight mirror. The design of this mirror was to incorporate technologies of ultra thin struts, thin facesheets, contour grinding, and frit bonding. These mirror design concepts maintain mirror rigidities comparable to existing state-of-the-art lightweight mirror structures so that it is possible to polish and test these mirrors without extending current

polish/test technology. Figure 1.2.1-1 is a plot of weight versus diameter comparing classical lightweight mirror designs to the advanced ultra lightweight designs. The upper curve represents classical mirrors. The curve has been scaled from 2.4-meter diameter (largest classical lightweight manufactured to date) to 4.0-meter diameter (Shuttle Cargo Bay limit) based on existing lightweight mirror technology.

The lower curve, labeled "Frit-Bonded Technology," represents a family of mirrors that satisfied the design constraints of blank manufacturing, optical polish/test, mounting, and launch in the various hostile environments in which these kinds of systems must survive. This family of mirrors does not represent a limit in technology, but instead represents conservative mirror designs for achieving realistic mirror weights for near-term systems. The Space Telescope mirror now weighs 1,650 pounds. Using Kodak's advanced technology, this same mirror could be produced in the 700 to 800 pound range, depending on system tradeoffs. Mirrors up to 4.0-meters in diameter can be reduced in weight from 5,500 pounds to approximately 2,600 pounds with the evolution of this technology.

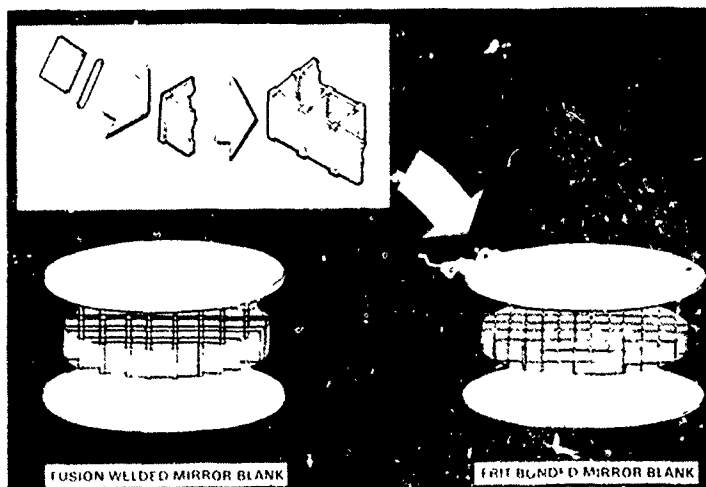


CLASSICAL LIGHTWEIGHT MIRRORS VS
ULTRA LIGHTWEIGHT FRIT-BONDED MIRRORS

Figure 1.2.1-1

1.2.2 Lightweight Mirror Manufacturing

In order to appreciate ultra lightweight mirror design, a discussion of lightweight mirrors--what they are and how they are manufactured--is needed. Currently, Corning Glass Works is the leading American manufacturer of lightweight mirrors. Corning builds lightweight mirror blanks of either fused silica or ULETM material (ULE, or Ultra Low Expansion, is a Corning Glass Works trademark for a material made of titanium-doped fused silica). The Corning process (which is shown in Figure 1.2.2-1) to make what we refer to as a classical or fusion-welded lightweight mirror blank, begins with a flame hydrolysis process in which fused silica or ULETM is deposited on a rotating table, in the presence of a gas flame, to form a glass boule. This glass boule is then machined into components referred to as struts and posts which are fusion welded together to form L-sections.



CORNING GLASS WORKS
MIRROR FABRICATION PROCESS

Figure 1.2.2-1

together to form L-sections. The glass fusion welding process melts the mating glass surfaces and forms a monolithic rectangular structure referred to as lightweight core. The core is machined plano-plano, rounded to the proper dimensions, and is then ready for assembling to faceplates which have been machined by a similar process.

Plates for blanks larger than the boule diameter are formed by stacking a number of boules in a furnace, fusing them together, then gradually flowing the plates out to achieve the proper diameter. Once the plates and core have been fabricated, the plate is assembled in a high-temperature furnace, the

core is assembled on top of the plate, and the second plate is then put in place. If the mirror is to be a plano-plano, it is fired front plate up, removed from the furnace, turned over, then returned to the furnace, and refired. If the blank is to be spherical, the second firing is done over a convex mold. The radius of the mold is generated to produce the desired radius of curvature in the blank after it is sagged or slumped to fit the mold. This mirror blank process has produced a large number of very successful mirror blanks, but due to the cross sectional dimension of the blank which is required to support the structure at the firing temperature, the high temperature firing process does limit the minimum weight of a blank. In other words, if the struts get too thin at the high temperature they will buckle or collapse; therefore, the faceplates must be thick (1.5 inches for the Space Telescope) at the blank stage to support their own weight over the cell center as the glass tends to soften and flow. This plate effect in the blank, which is referred to as quilting in plate thickness variation after the grinding process, will lead to gravity release figure effects.

Kodak recognized that one approach to reducing mirror blank weight was to find a process of bonding facesheets to cores without submitting the structure to the high temperature firing. Corning Glass Works has been involved for several years in an on-going program to develop an adhesive material (frit) which is designed to match the properties of their low coefficient glasses.

1.2.3 Frit Material and Processing

Frit is the generic name for a family of materials that have been in use in industry for a number of years. It is a ground glass material that is mixed with an appropriate vehicle, then fired at elevated temperatures. A typical example of frit use in industry today is bonding the faceplate to the television funnel or, in some cases, attaching head lamp faceplates to the reflectors. Frit is not a new material; in fact, the porcelain on your sink or stove is a frit-like material. What makes this material unique to this particular application is the fact that a frit has been found and developed by Corning Glass

Works that matches the parent mirror low expansion glasses. Strain mismatch between the frit and the glass is a two-step problem. The first problem is to reduce the mismatch to a level that will avoid structural failure during firing and subsequent use in assembly. Once it is established that there is not a stress/failure problem, the next step is to reduce the mismatch in strain to levels sufficiently low so that a long-term stable structure is produced. It is also desirable that the frit produce bond strengths equal to, or greater than, the bond strength achieved with the fusion welding, classical lightweight mirror fabrication process.

Frit and the frit process offer many advantages over the conventional approach. A dramatic decrease in weight is possible; core densities can be reduced from the current 10 percent in classical lightweight mirrors to something less than 5 percent.

Mirror distortion and dimensional change during firing are eliminated since frit fires at approximately 950°C, as opposed to 1700°C. Frit also offers a distinct advantage to the analyst since mirror math models do not have to accommodate mirror blank distortion. For all practical purposes, the one-g to zero-g transition effect on optical figures is eliminated because faceplate thickness variations are on the order of a few millimeters instead of the 0.6 to 0.8 centimeter differences which are typical of the classical lightweight mirror designs. The frit joints are also two to three times stronger than fusion-welded joints, resulting in a significant increase in the design allowable for mirrors. Frit mirror blanks come to the optical processor within a few millimeters of finished dimension, therefore eliminating the machining off of large amounts of glass (1.3 centimeters on the plates of the Space Telescope). The blanks can go directly from the optical processor into fine grind in preparation for polishing. Table 1.2.3-1 compares an advanced frit design mirror with the current technology example. The diameters of the two mirrors are the same (0.5 meter) and the rigidity or simply-supported

<i>Table 1.2.3-1</i> <i>CLASSICAL VERSUS ULTRA LIGHTWEIGHT</i> <i>MIRROR BLANK COMPARISON</i>		
MEASUREMENT	CURRENT CLASSICAL	FRIT-BONDED
DIAMETER	20 INCHES	20 INCHES
THICKNESS	5.0 INCHES	3 INCHES
RIGIDITY (SIMPLY SUPPORTED)	3.9×10^{-6} INCH	6.4×10^{-6} INCH
WEIGHT	33 POUNDS	9.0 POUNDS
PERCENT CORE	12.5	7.0
JOINT STRENGTH	2,800 PSI	>5,000 PSI

center of deflection is about the same, representing very rigid mirrors. The weight has been significantly decreased from 15 kilograms to 4 kilograms. For this particular mirror design, the percent of the core has gone from 12.5 to 6.7. Figure 1.2.3-1 shows a 0.5-meter diameter, ultra lightweight, frit-bonded mirror in existence at Kodak.

Under contract, Corning Glass Works fabricated the mirror blank to an advanced frit mirror design that was provided by Kodak. This mirror is representative of the advances in the state-of-the-art discussed earlier. The mirror blank was received at Kodak in 1978 and has been optically polished to a 0.024 wave rms (wave = 0.6328 \AA) using conventional polishing and test techniques. The test program objective was to verify the optical stability of frit-bonded, ultra lightweight mirrors.



*KODAK 0.5-METER DIAMETER
ULTRA LIGHTWEIGHT FRIT-BONDED MIRROR*

Figure 1.2.3-1

The first step following completion of mirror polishing was to establish the test configuration repeatability by conducting a series of optical tests, then analyzing the variability of these tests on a point-for-point basis in terms of optical surface error. Repeatability of the data and the test setup total range, point-to-point delta was found to be 0.007 waves rms at 0.6328 \AA

(Table 1.2.3-2). This was considered to be very good optical repeatability in the test setup and test data analysis, and was sufficient to evaluate optical stability of the mirror after exposure to a sequence of environmental tests.

The first test was a thermal cycle, during which the mirror was cycled ten times from -100°F to $+200^{\circ}\text{F}$.

Optical tests conducted before and after these cycles verified no measurable figure change. The purpose of the thermal cycle test was to induce thermal elastic deflection in the joints to try to emphasize any instability that might exist.

The mirror was also tested isothermally at 100°F , 70°F , and 0°F . The purpose of this test was to measure or detect any surface quilting due to the strain mismatch between the frit and the glass. Analysis had predicted that for these temperature changes, no quilting should be observed in the surface. This proved to be true; we saw no measurable quilting in the data.

A mechanical deflection test was run, also to flex the joints and to try to induce any instabilities that might be in the blank. The mirror was simply supported and a uniform 4-g load was applied ten times. The pre- and post-optical tests measured no optical figure change. The mirror was then introduced into a hard vacuum chamber at approximately 10^{-6} torr, with no change.

The impressive result of this testing is that when the optical test preceding the environmental tests and the optical test following the environmental testing were compared on a point-for-point basis, the result was 0.008 wave rms at 0.6328 \AA . This data shows that there was no measurable change in this mirror over the time period from the completion of optical processing to the present time.

TEST	RESULT
TEST BED REPEATABILITY	0.007 λ RMS
THERMAL CYCLE -100°F TO $+200^{\circ}\text{F}$	NO FIGURE CHANGE
ISOTHERMAL TEST AT 100°F	NO MEASURABLE QUILTING
ISOTHERMAL TEST AT 0°F	NO MEASURABLE QUILTING
4-G MECHANICAL DEFLECTION TEST	NO FIGURE CHANGE
HARD VACUUM TEST	NO FIGURE CHANGE

1.3 SUMMARY

This section presents a summary of the major accomplishments of the Ultra Lightweight Mirror Manufacturing and Radiation Response study.

1.3.1 Frit-Bonding Process Evaluation

Under a subcontract from Eastman Kodak Company, Corning Glass Works has studied the critical aspects of the frit-bonded mirror blank manufacturing process. As a part of this task a preliminary frit-firing furnace design has been completed, acid etching facilities and environmental impact studies are complete, a production-size lot (5 kilograms) of ULE™ frit material has been evaluated, and the mirror assembly techniques and mirror handling equipment have been identified.

1.3.2 Mirror Blank Handling and Furnacing Analysis

Both finite-element and closed form analysis were conducted to evaluate the stress and deflections induced into the mirror blank components by each of the critical handling steps. The results of this analysis show that mirror components up to 4.0-meters in size (Shuttle cargo-bay limit) can be handled safely and can be assembled to produce an ultra lightweight mirror blank.

1.3.3 Heat Flux Irradiation Testing

A 0.5-meter diameter, ultra lightweight, frit-bonded, ULE™ mirror has been irradiation tested and analyzed, and the test data has been scaled to typical ultra lightweight, 2.4-meter and 4.0-meter mirror designs. The 0.5-meter mirror absorbed a heat flux of 3.05 kw/m² for a period of 80 seconds. The optical figure of the mirror was interferometrically measured throughout the 80 second exposure and optical delta maps (start to end) were prepared.

The optical figure change induced by the thermal flux was interferometrically measured as 0.76 wave P-V (wave = 6328 angstroms) power and 0.0255 wave rms surface exclusive of power. This compares to a calculated power change of 1.02 wave P-V using the NASTRAN finite element mathematical model, and 1.1 wave P-V using a closed form analysis. This data has been scaled to 2.4-meter and 4.0-meter mirror designs and shows power changes of 1.07 wave and 0.94 wave P-V, respectively. The results of this task show that frit-bonded, ultra lightweight mirrors are extremely stable in hostile thermal environments and that they behave in a very predictable fashion.

2.0 CORNING GLASS WORKS SUBCONTRACT

Corning Glass Works (CGW) was contracted by Kodak to investigate the issues of frit material, frit application, component assembly, blank firing, and the facilities required for fabrication of large aperture, ULE™, frit-bonded mirrors. The task was divided into two areas: frit material development, an effort at the research laboratory and a frit bonding evaluation. The latter task was addressed by Corning's Canton plant and the manufacturing and engineering division.

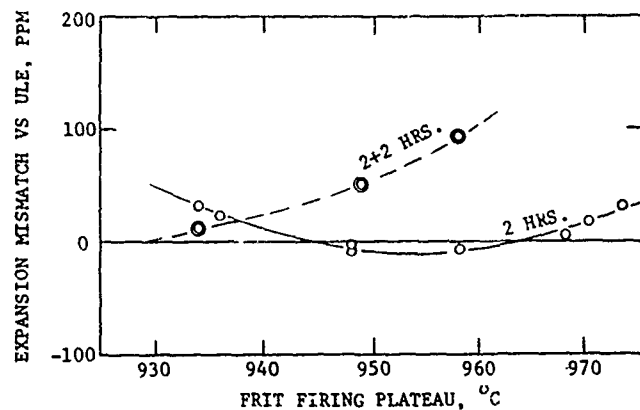
2.1 FRIT TASKS

2.1.1 Frit Material Development

The work accomplished in the research laboratory was in three areas: frit firing characteristics, alternatives to the frit dipping applications process, and measurement of the pull-out loads required for the core dipping process.

Corning made some proprietary adjustments in the ULE™ frit composition and processing in order to produce a 5-kilogram melt. The resulting frit has excellent firing characteristics, as shown in Figure 2.1.1-1. In addition to the excellent firing range, the T-sample test data for this frit has shown the typical break strength averaging well over 7000 psi.

T-samples were also used in evaluating a frit application technique as an alternative to the dip process. The concept was to apply dams to the plate



MISMATCH VS FIRING PLATEAU FOR
SINGLE AND DOUBLE FIRED U-A FRIT

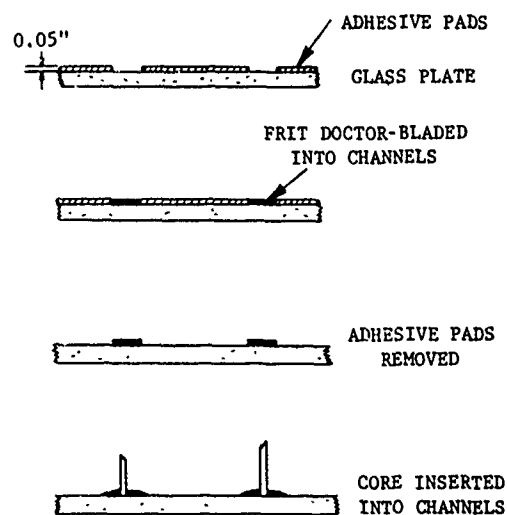
Figure 2.1.1-1

surfaces resulting in an orthogonal channel pattern which was the same dimension as the core structure. The channels, or streets, are then filled with frit material, the dams are removed, and the core is positioned into the channels as shown by Figure 2.1.1-2.

A total of twelve T-samples were constructed--eight channel strips and four regular dip--as a control group. The average break strengths and standard deviation are as follows:

	Channel strip	Dip
Average, psi	9860	9180
Standard deviation, psi	1100	1170

It was concluded, strictly from the joint strength point of view, that this is a viable application approach.



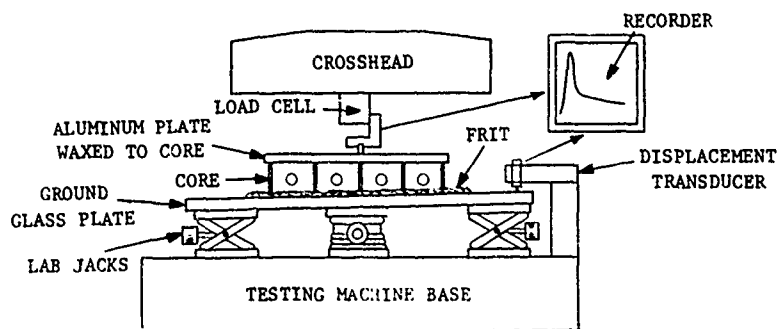
CHANNEL-STRIP METHOD
FOR CORE-PLATE BONDING

Figure 2.1.1-2

Data was also acquired from the laboratory regarding the load levels required to pull the core out of the frit after dipping. This data was needed to support the handling analysis of the core assembly.

Eastman Kodak Company supplied a plano-plano, 16-cell, lightweight glass core with 2-inch square cells, having 0.105-inch thick struts. The projected glass surface area of this core is 8.5 square inches. One of the plano surfaces of this core was joined to an aluminum plate, 9 inches by 9 inches by 1.5 inches, using beeswax. The plate was drilled and tapped at the center to accommodate the load cell.

The test configuration is shown on Figure 2.1.1-3. Figure 2.1.1-4 is a photograph of the equipment during actual testing. A large glass plate with fine ground surfaces was supported on the Tinius Olsen testing machine base and leveled, with respect to the core, by using three lab jacks. The

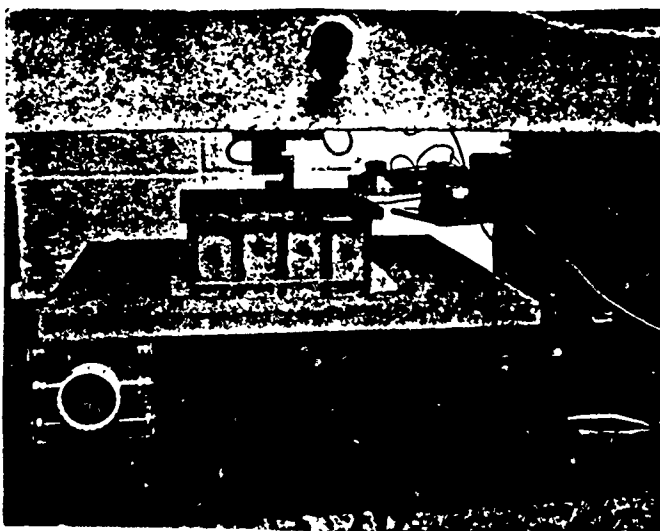


APPARATUS SHOWING

Figure 2.1.1-3

aluminum plate core assembly was bolted to the machine crosshead. This setup gave a rigid (hard) system to guarantee uniform core extraction at the programmed rate. A calibrated load cell and LVDT extensometer were connected to an x-y recorder, with 2 pounds and 0.15 inch used as full-scale readings, respectively.

The frit was applied by the typical squeegee method to the ground plate, covering an area somewhat larger than that of the core. The crosshead was lowered so that the leading surfaces of the core penetrated the frit layer sufficiently that a compressive force of 1 to 2 pounds could be maintained with the crosshead motion arrested. This assured that the core had bottomed and was in contact with the plane.



PHOTOGRAPH OF APPARATUS

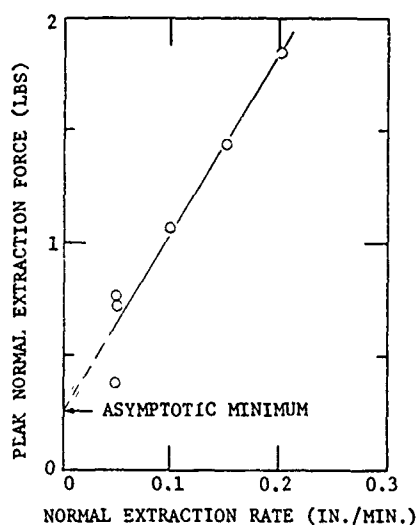
Figure 2.1.1-4

After waiting a few minutes to ensure that the frit had completely wetted the core, the crosshead was raised at a predetermined rate. The x-y recorder plotted the associated force-displacement function.

Force-displacement curves for four extraction rates are plotted in Figure 2.1.1-5. The force peaks at a displacement between 0.002 and 0.005 inch, depending on extraction rate. This pullout force is identified with adhesion.

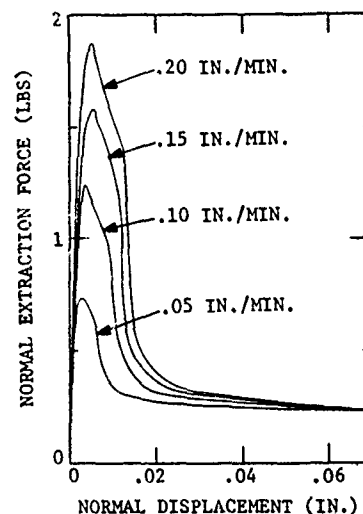
The force intercept seen in Figure 2.1.1-6, which is also apparent as the asymptotic minimum in Figure 2.1.1-5, is thought to be a combination of weight and surface tension for clinging frit.

The peak force plots linearly with extraction rate, as shown in Figure 2.1.1-6. Three different extractions were made at the 0.050 inch per minute rate. The low force point was the first run which turned out to be due to insufficient time



PEAK NORMAL EXTRACTION FORCE VS EXTRACTION RATE FOR FRIT DIP PROCESS

Figure 2.1.1-6



FORCE-DISPLACEMENT CURVES FOR VARIOUS EXTRACTION RATES IN THE FRIT DIP PROCESS

Figure 2.1.1-5

for the frit to wet the core. The subsequent runs were made after waiting for the frit to wet.

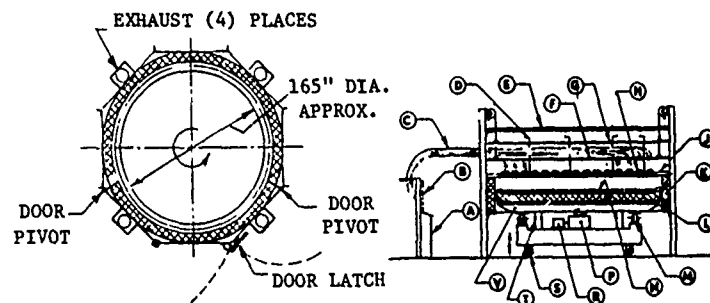
It should be noted that very uniform frit application was accomplished by this controlled extraction.

2.1.2 Frit Bonding Evaluation

The frit bonding evaluation was conducted as a joint effort by Corning's Canton manufacturing and engineering group. The evaluation includes a process sequence and equipment description, facilities modification, and environmental impacts. The current glass fabrication process

and the grinding of core components is unaffected by the design changes for fusion-bonded versus frit-bonded mirror blanks.

2.1.2.1 Process and Equipment Description - The anticipated approach for producing large aperture blank plates (more than 120 inches in diameter) is to fusion-weld (vertical seals) hexagonal pieces of ULE™ into the desired diameter. The equipment required is similar in design to existing equipment used for fusion-sealing large blanks. The plate parts are placed in the furnace (shown in Figure 2.1.2-1), which is heated sufficiently to achieve the vertical seal, then cooled rapidly to minimize further distortion.



SEALING FURNACE

Figure 2.1.2-1

Rapidly heating and cooling down this large furnace is a critical function. The existing furnaces in the Canton facility are not suitable for expansion to perform this operation. The proposed furnace will be equipped with natural gas and oxygen burners capable of providing temperatures in excess of 1700°C. This fuel mixture is introduced into the furnace through multiple burners which are individually controller by flow meters housed in panels mounted adjacent to the furnace.

The cavity of the furnace, which contains a rotating table to maintain uniform temperature gradients, is sufficient to fusion-seal plates for mirrors more than 120 inches in diameter. Since this furnace is similar to existing furnaces currently in use at Corning Glass Works, no new technology is required for the design. It is anticipated that this furnace will be designed and fabricated during 1981 under another DARPA contract.

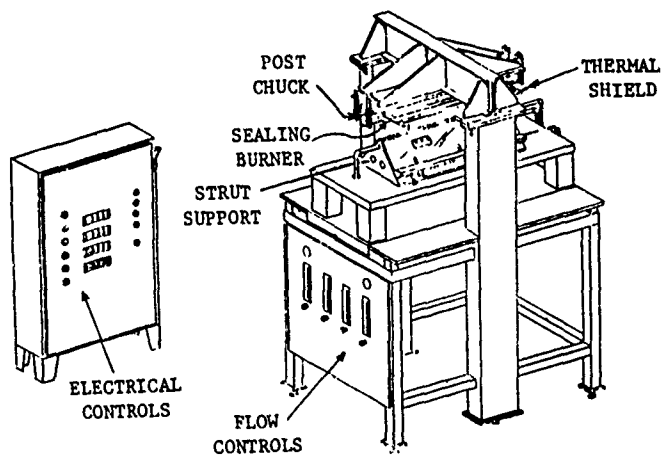
A grinder, which is necessary for shaping plates to close tolerances for frit assembly, is now on order and will be installed under a separate DARPA contract.

This machine will be manufactured by the Campbell Grinder Company. The design is basically that of a vertical boring mill with a 163-inch turntable, a 180-inch swing clearance, and a 49-inch vertical clearance. The machine consists of a steel base, which supports the turntable and its variable speed drive. The overhead steel bridge, straddling the base and turntable, will be equipped with dual variable-speed grinding spindles.

Electronic numerical controls will be provided for the grinding spindles to allow maximum flexibility in generating precise surface contours. According to the manufacturer's design specifications, the machine will be capable of generating surface contours to ± 0.001 inch of the mathematical curve. Digital readouts will indicate position on all axes to ± 0.005 inch to facilitate manual feed control and alignments, necessary to I.D. and O.D. grinding, and for set-up prior to automatic contour grinding of plates and cores to the tolerances necessary in construction of large, lightweight, frit-sealing blanks.

Cores for frit-sealed, large, lightweight mirror blanks differ primarily from fusion-sealed blanks in strut and post dimensions. Similar equipment is used both fusion or frit-bonded mirror construction; these include an ell-maker, core-maker, and core assembly table. A new ell-maker will be designed to accurately prefabricate the 30-inch long ells required to construct a large mirror core. The design will be based on both Corning's existing ell-makers and their operational experience, and will utilize the same ell manufacturing process.

The new ell-maker (Figure 2.1.2-2) will consist of a welded main frame; two stationary, water-cooled, sealing burners; thermal shielding; electrical and services controls; a post check; and a movable strut support used to align, clamp, and simultaneously lift and squash two struts into the post during burner firing to form an ell. Parts loading and unloading will be manual, with automatic sequence of burner ignition, firing and shutdown.



ELL MAKER

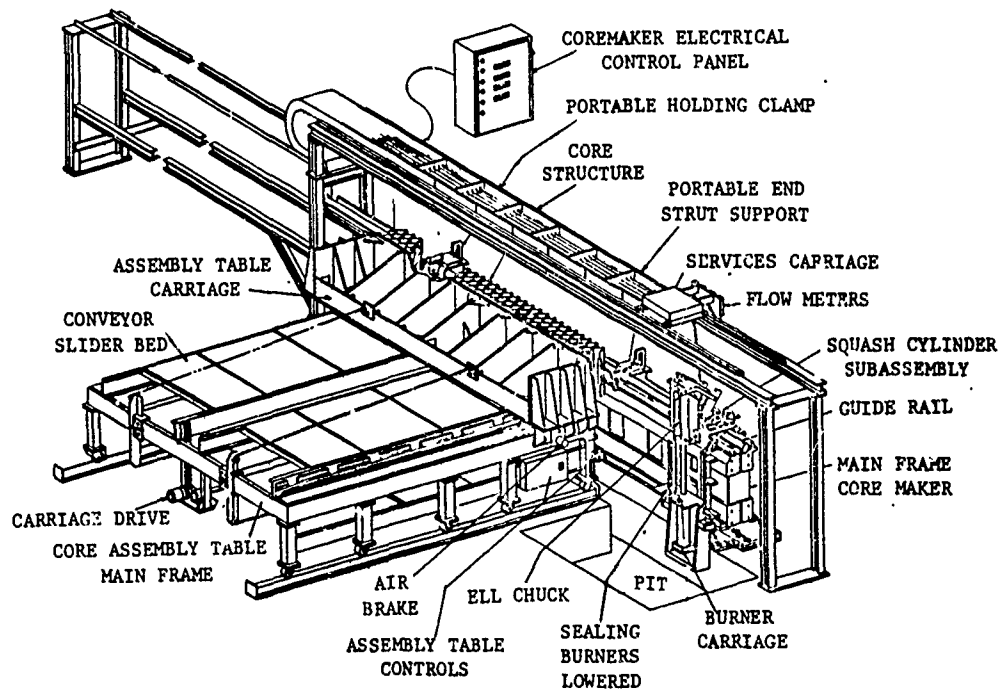
Figure 2.1.2-2

Current core-maker equipment is limited by physical dimensions at approximately 100-inch diameter blanks. Time and cost estimates for revising and updating the existing core-maker, including the core assembly table for large, frit-sealed blanks, has determined that new equipment will be needed.

The new machine (Figure 2.1.2-3) will be designed to build cores with a minimum of 4-inch-square cells, 30-inches deep, and 180-inches wide, when used in conjunction with a new core assembly table. The core-maker will be constructed with a welded main frame, approximately 25 feet long, with carriage guide and locating rails mounted to it. The ell holding chuck and squash cylinder assembly will have an integral burner carriage. The newly designed sealing burners will mount to the burner carriage. Electrical and service controls and the service support frame will be mounted as space constraints dictate. Miscellaneous features will include portable core holding clamps, supports for unfused end struts, and dial indicators for setups. Improvements to the equipment will include automatic burner ignition and microprocessor-controlled process sequence.

The core assembly table will be a new table similar in concept to Corning's existing monolithic conveyor table, but specifically designed for use with a new core-maker to assemble a mirror core 180 inches wide by 180 inches long.

The table will be comprised of a main frame, two wide conveyor slider beds, and a carriage weldment with a vertical graphite face 180 inches wide by 28 inches high, bridging both table slider beds. Two wide conveyor belts will be attached to the carriage and pulled over the slider beds, carrying the assembled core as the motorized carriage is retracted across the table.



CORE-MAKER ASSEMBLY TABLE

Figure 2.1.2-3

Two air brakes will clamp the carriage to the main frame during cell fusing. Wheels under the main frame will permit moving the assembly table a short distance away from the core-maker to facilitate finished core removal.

Core trimming operations are performed with existing abrasive equipment prior to the lapping and grinding operations. Core contour grinding is accomplished on the contour grinder machine.

The mirror will be assembled once, prior to cleaning and the frit application, to check dimensions and fit. At this point in the operation the mirror will consist of three parts which will be joined by frit: front plate, back plate, and core. These are removed from storage and moved to an acid-etching facility. Acid etching has been demonstrated to be necessary for surface preparation to maintain frit glass bond strength. The plate and core handling equipment are shown in Figures 2.1.2-4 through 2.1.2-7.

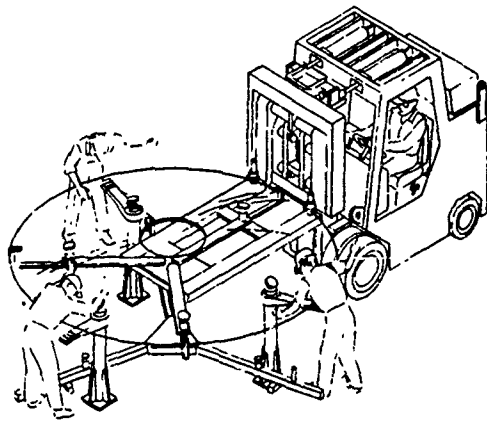
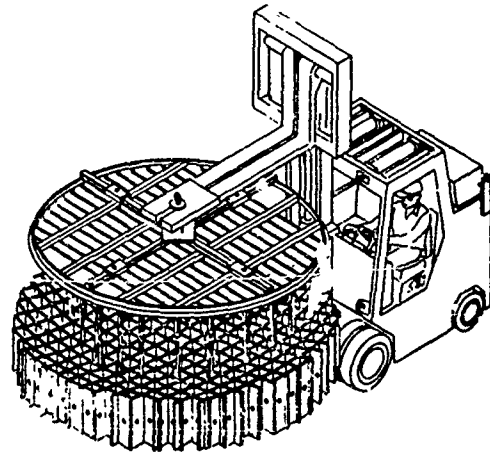


PLATE HANDLING DEVICE

Figure 2.1.2-4



CORE HANDLING DEVICE

Figure 2.1.2-5

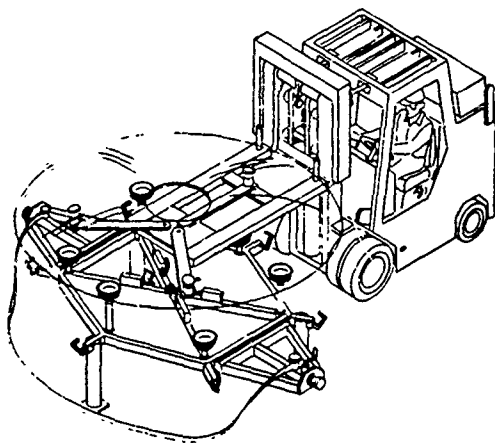


PLATE HANDLING INTO TURNOVER YOKE

Figure 2.1.2-6

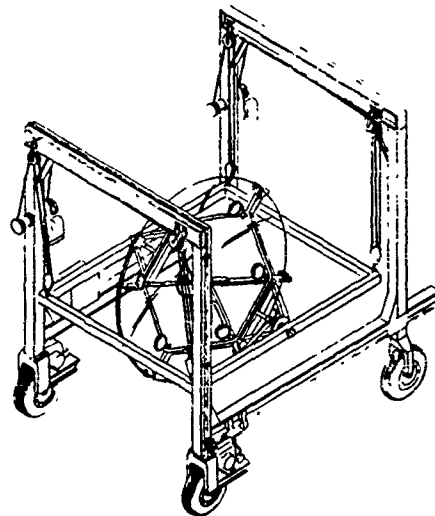


PLATE TURNOVER DEVICE

Figure 2.1.2-7

Etching will be accomplished by complete immersion of parts in a bath of mixed hydrofluoric and hydrofluorosilica acid (Figures 2.1.2-8 and 2.1.2-9). The complete etching process is shown in Figure 2.1.2-10. Support structures for the parts will require designs which specifically address minimum deflection of parts and acid attack resistance. Transfer to a second tank via an overhead crane precedes a complete rinse with de-ionized water. Drying is accomplished with heated air. Cleaned and etched parts will be protected with lens tissue and polyethylene. Acids for the single set of

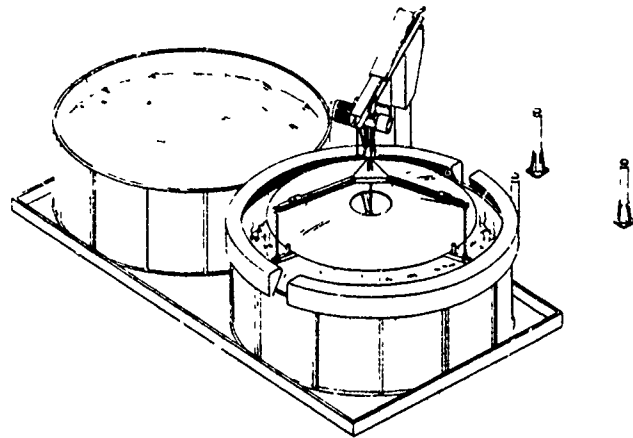
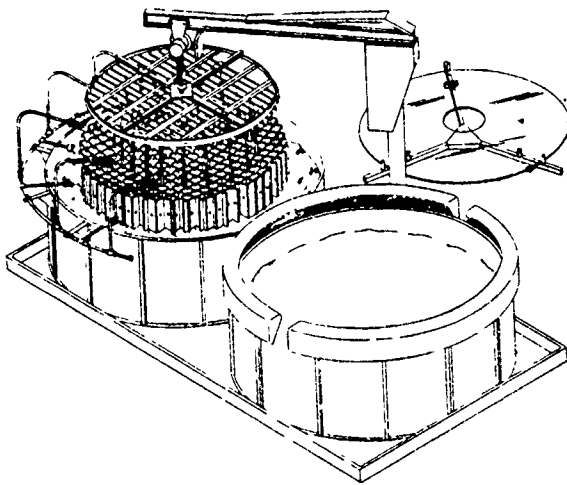


PLATE ACID ETCH

Figure 2.1.2-8

parts will be delivered premixed, then transferred to tanks. After use, the acid mixture and rinse water will be transferred to a tank truck for disposal.

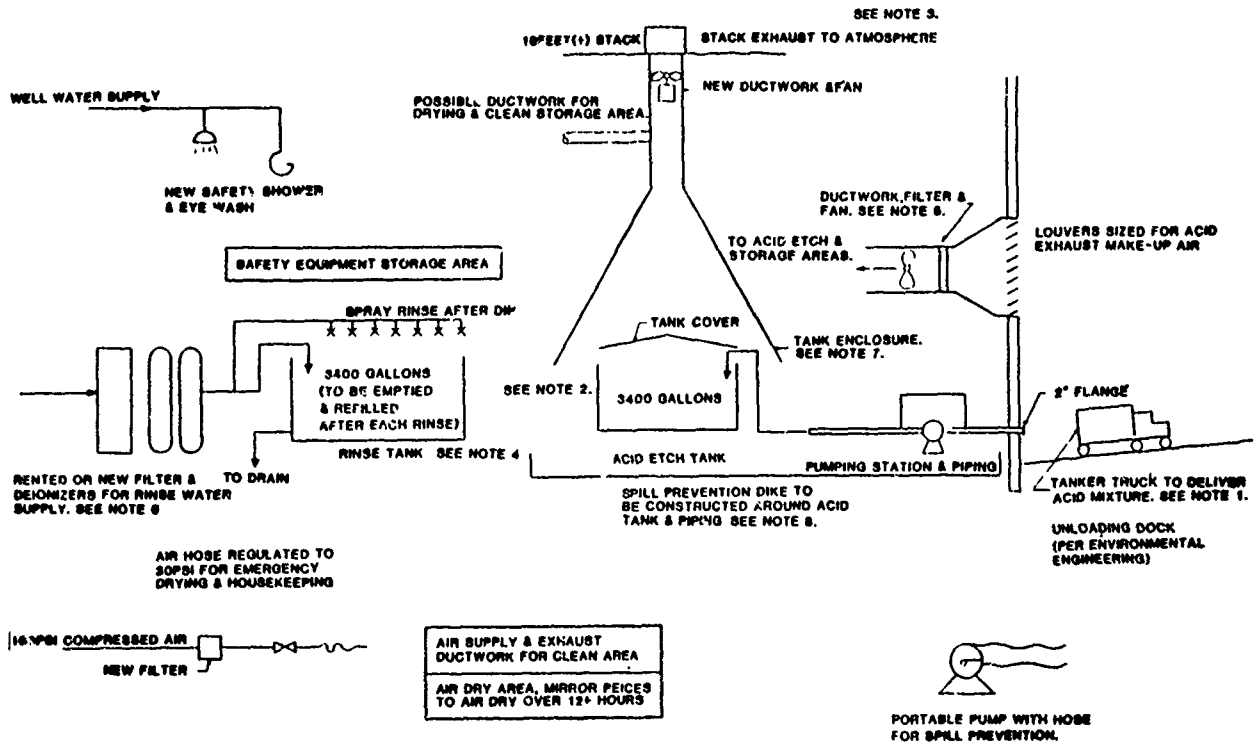


CORE ACID ETCH

Figure 2.1.2-9

of a glass blocking body contoured to match the core. Side one is dipped into the frit material, the core is turned by hand, then the second side of the core is dipped.

The frit material application process requires that frit be applied in metered amounts to provide coverage of plate-core contact areas and to achieve proper filleting along the strut edges. At present, the process involves multiple dipping of the core into a metered thickness of frit which has been applied to the surface



ACID ETCHING SYSTEM

Figure 2.1.2-10

Mirror blanks up to 20 inches in diameter have been successfully assembled in this manner.

The dip process produces acceptable mirror blanks. Scale-up of this process involves at least the following problems:

- Manual part handling becomes difficult and the risk increases as the mirror blank diameter increases.
- Touchup of frit starved areas becomes logistically more difficult.
- For large blanks, time required to apply frit and to assemble parts is critical to the frit exposure time.

- Component deflection becomes significant without specialized handling devices.
- Forces are required to pull core out of frit layer for larger diameters.

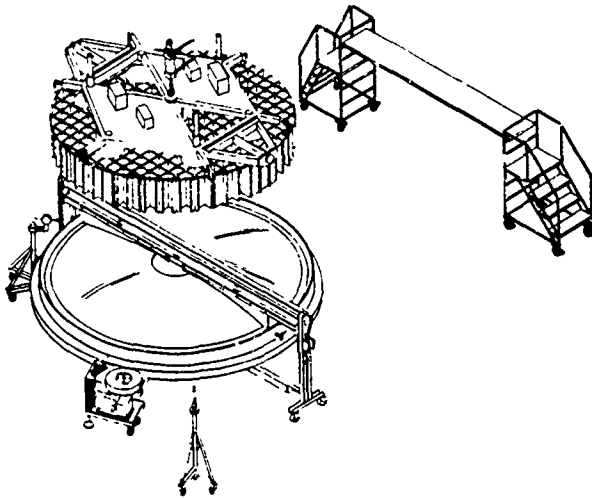
The frit process, using dip with single firing, appears to be scalable to the 40- to 60-inch diameter range, where hand dipping and turning of cores is practical. Handling and turnover aids would extend the range somewhat; however, definition of the limits would require further investigation.

With handling aids, it is expected that large cores with frit applied to one side cannot safely be turned over; thus, at larger diameters it becomes desirable to dip-apply frit to one side of the core, assemble the plate to this side, then complete the firing. The structure can then be turned in a box, using conventional methods. Frit is then dip-applied to the remaining core surface, assembled to the second plate, and fired again. Frits presently developed have the capability for limited multiple firings. The need to turn cores over with frit applied to one side is eliminated by this double firing. The additional firing does, however, reduce by one the potential frit firings now available for defect repair.

The additional risk in the double firing approach, coupled with the preceding concerns, suggested exploring an alternative to the dip process. Included in this report is the description of both a dip approach and some alternatives.

The double fire dip method begins with the application of a 0.050-inch thick frit layer to a glass blocking body, contoured to fit the surface of the core being fritted (Figure 2.1.2-11).

A doctor blade applied to a rotating body maintains frit thickness until just prior to dip, and may be utilized to smooth the frit layer between dips if multiple application is required. The core is suspended above the body on a multiple point support spider. The core is lowered into the frit until its



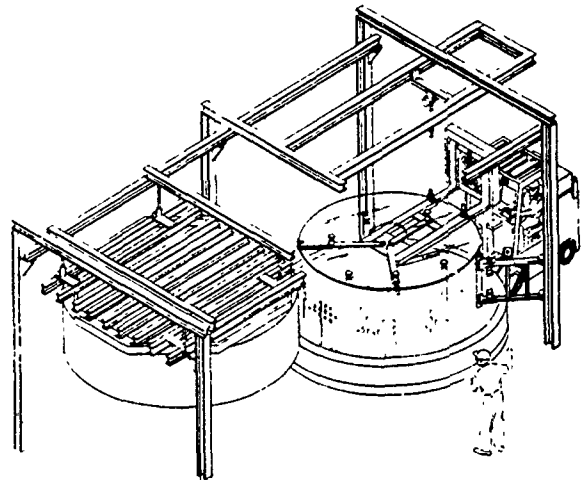
FRIT DIP APPLICATION

Figure 2.1.2-11

The fritted core is immediately positioned over the plate already mounted in the frit firing furnace. Figures 2.1.2-12 through 2.1.2-14 show the assembly sequence. Alignment jigs assure positioning of the core relative to the plate as it is lowered. Removal of core-supporting spider and alignment jigs allows positioning of the top half of the frit sealing furnace. After firing is complete, the back plate-core assembly is frit-sealed to the front plate in a similar manner.

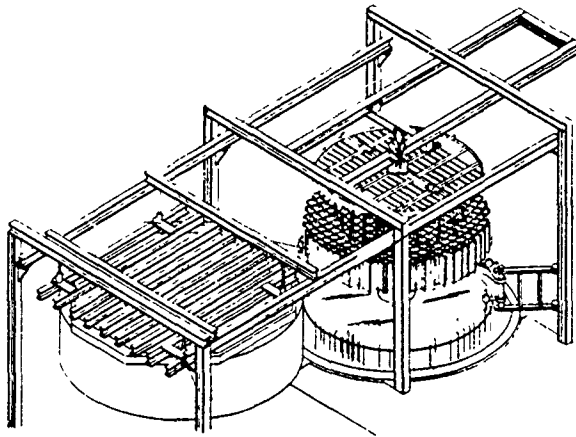
A single firing application technique would provide a controlled amount of frit in a predetermined pattern to the faceplates.

full weight is resting on the blocking body. Pullout from the frit is accomplished at an initial rate less than 0.2 inch (0.5 centimeter) per minute, which maintains pullout forces at less than 0.25 pounds per square inch of the core area, or approximately 150 pounds total. Shock absorbers, which are built into the support spider, prevent rapid release from frit and damp out any excess movement. A second dip of the same side and touchup of nonuniform areas completes application.



BOTTOM PLATE ASSEMBLY IN FURNACE

Figure 2.1.2-12



CORE ASSEMBLY IN FURNACE

Figure 2.1.2-13

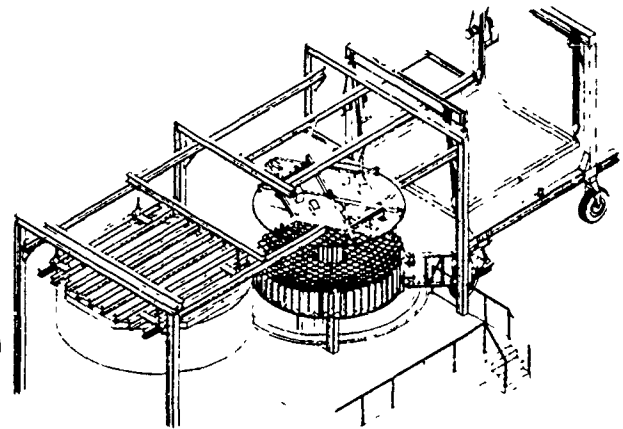
- Application to plates with ground channels dimensioned to retain the desired volume of frit, and subsequent assembly of core to fritted plates.

All of the above approaches are feasible, pending detail consideration in a preliminary engineering stage. The brief examination time allotted to this stage of feasibility engineering indicates that application to plates with automated nozzle equipment is the most likely to be successful.

The automated application equipment shown in Figure 2.1.2-15 will consist of a plate support, overhead gantry and positioning system for nozzle application, frit supply equipment and microprocessor control system. The plate support and overhead gantry are standard equipment with revisions for handling.

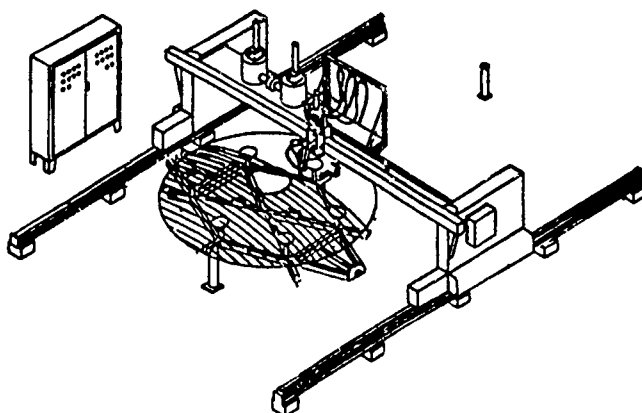
The potential frit application alternatives are as follows:

- Application to plates in core contact areas with automated nozzle equipment and subsequent assembly of core to fritted plates.
- Application to plates masked to avoid frit deposit in unwanted areas, removal of mask, and subsequent assembly of core to fritted plates.



TOP PLATE ASSEMBLY IN FURNACE

Figure 2.1.2-14



FRICT APPLICATION EQUIPMENT - AUTOMATIC

Figure 2.1.2-15

for frit application facing up. Frit will be applied in 0.500-inch wide by 0.050-inch deep bands in the square grid pattern where the core will contact the plate. This width is sufficient to allow for core manufacturing variations and expected mismatch. The depth provides sufficient volume to produce desired fillets. The application pattern will be either straight-line or zig-zag. Development work is required to define nozzle configuration, spacing, laydown pattern, and frit characteristics.

Frit is applied first to the back plate, which is transferred to the frit firing furnace. The core is assembled to the back plate in the frit firing furnace, utilizing alignment jigs. Frit is next applied to the convex side of the front plate, then turned prior to assembly to the core and back plate in the furnace.

The application equipment will be capable of frit laydown rates and location accuracies necessary for compatibility with assembly times and manufacturing tolerances. It is anticipated that frit touchup or repair should be minimal. This approach avoids the possible surface contamination with a surface masking approach, and eliminates the need to remove any parts for the plate surface.

Nozzle positioning robotics and software will require definition by preliminary engineering and will probably be specially designed using standard parts. Associated control equipment is in existence, but will require modification for this specific application.

The plates will be mounted in support fixtures with the sides

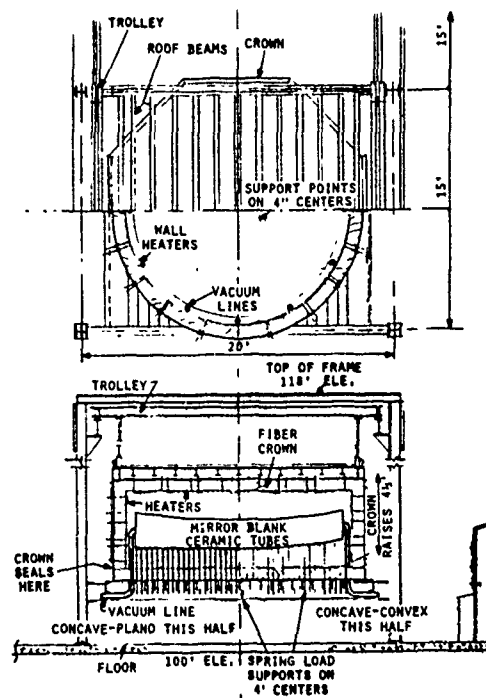
The mirror is fired in an electric furnace on a precision firing schedule. The initial portion of the cycle provides for the purging of frit vehicle vapors via a vacuum system. The actual firing cycle is an extension of demonstrated frit technology.

Design parameters for the frit sealing furnace are as follows:

- Ability to frit-seal assembled blanks and to anneal plates.
- Maximum mirror dimension is 160-inch diameter.
- Frit sealing temperature is 970°C.
- Annealing temperature is 1050°C.
- Mirror support is on 4-inch centers.
- Top fully removable for mirror assembly.

The furnace, shown in Figure 2.1.2-16, is intended to frit-seal plano, concave, or convex blanks of circular or oval form sized to maximum dimensions. It will have secondary capability to anneal parts for the large blanks.

The furnace cavity will be 5 feet high by 15 feet in diameter. The framework is constructed from structural steel, with cover plates of 1/8-inch steel plate. The furnace bottom will consist of structural tees for the support of the rod system. Clearance beneath the furnace will be a minimum of 33 inches to allow for adjustment, repairs and maintenance. Service catwalks will provide access to all external surfaces of the furnace.



ELECTRIC FRIT FIRING FURNACE

Figure 2.1.2-16

Control panels for holding meters, gauges, thermocouple temperature readout, and power display equipment will be required, as well as racks for the power packages. This equipment, including computer and microprocessors, will need an area free from the corrosive atmosphere of nearby glass forming processes.

The furnace will be designed to facilitate loading by forklift truck or overhead crane. Furnace crown and sidewalls will be removable as a unit.

Supports for the mirror or component parts during frit sealing or annealing will be 3/4-inch diameter refractory tubes through the furnace bottom. There will be 1352 of these tubes on a 4-inch by 4-inch center-to-center grid spacing. Tubes, which will be supported from below the furnace by compression springs, will have adjustment screws. Ceramic rods are adjusted to part contour prior to part loading. Adjustment range will be 8 inches. A spring constant $K = 40$ pounds-per-inch will give a normal deflection on each of the load points of about 1/4 inch at even loading. For a deviation of 0.001 inch the additional spring load will be 0.64 ounce.

A six-point load pickup system will be used to transfer the back plate from forklift to furnace support system. Three pickup posts will be raised or lowered by interconnected ballscrew jacks projecting through the furnace bottom. The mirror or plate will be kept level at all times.

A center support beam with three jacks will be installed under the furnace to prevent any sagging when the mirror is loaded.

Core and top plate loading will utilize core support spider and vacuum cups, respectively. A load will be applied to the top plate to maintain part alignment during firing. The crown design will include provision for additional top plate restraint similar to the bottom rod supports, if required.

The furnace crown is moved into position by overhead monorail, and is lowered with a system of four interlocked ball blank jacks and a drive motor.

Drive units will be interlocked to prevent blank or furnace damage through inadvertent movement.

Thermal insulation will be 2300⁰F alumina silica fibers in blanket form, mechanically attached to crown, floor, and side cover plates. The furnace will be electrically fired with nichrome elements mounted to all internal surfaces. Precise temperature control will be achieved by computer control of fifty 10-kilowatt heating zones. Fully redundant windings and total power capability will protect the heating cycle. Two thermocouples per zone will provide temperature sensing to provide an accurate temperature profile. Temperature variation is expected to be less than $\pm 1^{\circ}\text{C}$ within the furnace cavity.

A vacuum system will be used to withdraw frit vehicle volatiles from inside the mirror during the bake-out cycle of the frit firing sequence. Multiple exhaust points through the furnace bottom will be provided.

2.1.2.2 Facilities Modification and Environmental Impacts - The expansion of equipment and furnaces will require additional electrical supply equipment from the substations. It is currently feasible to make these additions. Costs and necessary equipment will be determined at preliminary engineering stages.

Water and gas services currently available at this Corning plant are sufficient to handle this project.

Although the existing building structure contains sufficient area for the process, relocation of existing equipment and services will be necessary.

The environmental impacts are centered on effluents from the glass manufacturer's process and the acid etch process. The volume of glass required for a single large lightweight mirror is not expected to impact glass forming emission rates. Multiple mirrors will have effects, however, as described in

Contract No. F-30602-80-C-0317, paragraph 3.6. The acid etching facility will have effects as described in the following paragraphs.

The acid etching system consists of one 3400-gallon rinse tank and one holding tank containing 50 percent (by weight) 50 percent HF and 50 percent (by weight) 30 percent H_2SiF_6 . The tank will be held at ambient temperature; it will be located inside the plant complex; and it will be ventilated with an exhaust hood and fan system. The tank will be filled and emptied by a tanker truck. Each frit-sealed, large, lightweight mirror will use and return 3400 gallons of acid mixture to the vendor.

Preliminary analysis indicates that there are several State and Federal environmental regulations which are applicable to the acid etching system and waste disposal.

The system must be designed to insure the safest possible work environment since the CGW policy for hydrofluoric acid requires that all plants/facilities with hydrofluoric acid installations be designed and engineered to include the safest possible conditions regarding layout, location, relations to other operations, storage and handling facilities, exhausting, diking, neutralizing, and disposal.

All necessary precautions will be included in the design to insure that no acid is introduced into the environment so that it reaches any nearby waters. The Federal Clean Water Act and Federal Environment Protection Agency (EPA) regulate designated hazardous substances which are subject to the EPA Spill Reporting and Clean-up Program. For each hazardous substance there is a specified minimum "reportable quantity," expressed in pounds/kilograms. For hydrofluoric acid this amount is 5000 pounds (2270 kilograms). If this minimum reportable quantity is spilled into a navigable waterway, an immediate cleanup procedure must be undertaken, and the Federal EPA must be notified. Failure to comply with these regulations can lead to substantial civil and criminal penalties. Furthermore, the company may be liable for, among other penalties, a judicially or administratively imposed penalty for the discharge itself, as well as the cleanup cost.

Acid spills of less than the Federal reportable quantity may still be reportable to the New York State Department of Environmental Conservation (NYSDEC). This is the case if the spill reaches a waterway, or if it spills into the plant wastewater system, causing the existing plant outfall to exceed its State wastewater discharge permit limit.

A NYSDEC air source permit must be obtained for an acid tank exhaust hood/fan/stack system before installation. This requirement should not present any difficulties. With the acid at ambient temperature and only one acid tank, it is unlikely that any control will be necessary.

Off-site disposal of the acid must comply with new Federal Resource Conservation and Recovery Act hazardous waste disposal rules and regulations. The waste acid will be shipped by manifest to a permitted hazardous waste treatment or disposal facility. Department of Transportation regulations will be complied with.

Overall governmental regulatory needs concerning the acid etch system and waste disposal are few, but necessary. Common sense and best engineering judgment will be used to provide a safe working environment and to insure compliance with all environmental regulations.

2.1.3 Conclusion and Recommendations

The conclusion of this study is that it is feasible to fabricate a large aperture, ultra lightweight, ULE™, frit-bonded, mirror blank. The study indicates that facility and environmental impact can be managed with existing technologies. Areas which will require further investigation and definition include the application technology, core fabrication scaleup, acid etching, and furnacing.

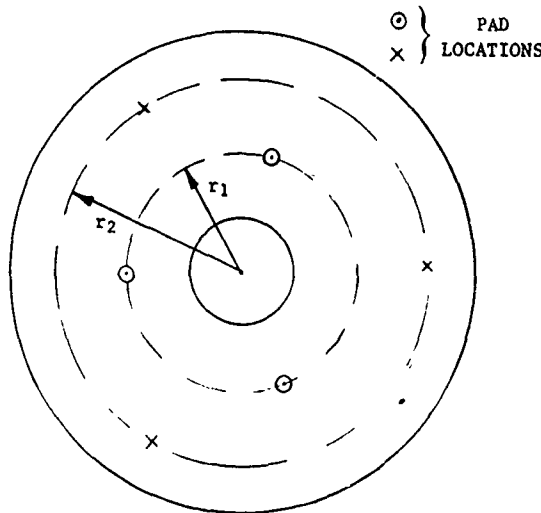
The development phase of this program will include sufficient hardware demonstration to insure the confidence and credibility for producing large aperture mirror blanks.

2.2 MIRROR BLANK HANDLING AND FURNACING ANALYSIS

2.2.1 Mirror Component Handling Analysis

During the fabrication of a mirror blank, it is necessary to handle the mirror facesheet and core structure before these components are bonded into a rigid mirror structure. Typical of a very large mirror design is the 4.0-meter monolithic mirror configuration shown in Table 2.2.1-1. The feasibility of the proposed handling methods will be checked, using the mirror design parameters shown in this table.

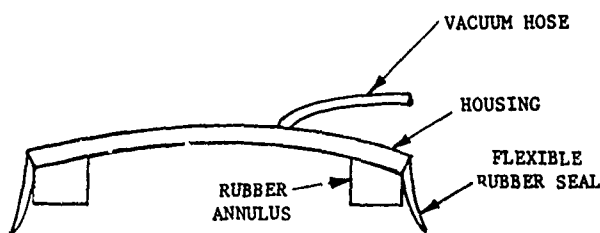
Table 2.2.1-1 4-METER MONOLITHIC MIRROR DESIGN	
MEASUREMENT	DIMENSION
FACEPLATE THICKNESS	0.5 INCHES
STRUT THICKNESS	0.08 INCHES
CELL SPACING	4.0 INCHES
EDGE THICKNESS	27 INCHES
OUTSIDE DIAMETER	160 INCHES
INSIDE DIAMETER	48 INCHES
WEIGHT	3000 LBS



LOCATION OF VAC-U-LIFT PADS
Figure 2.2.1-1

During assembly of this particular mirror, a 0.5-inch plate must be lifted. (In reality, the plate will be somewhat thicker than 0.5 inch since material will be removed during the polishing operation.) It is proposed that the plate be lifted by using a Vac-U-Lift lifter with six pads. These pads will be located on two different diameters, and will be equally spaced in the circumferential direction as shown in Figure 2.2.1-1.

A cross-sectional view of the vacuum pad is shown in Figure 2.2.1-2. As a partial vacuum is drawn, the glass plate is pressed against the rubber annulus, producing a lifting force. It is important to include the rubber annulus in the design to avoid applying highly localized loads on the glass. The metal



CROSS SECTION OF VACUUM PAD

Figure 2.2.1-2

housing is slightly curved to accommodate convex surfaces. This curvature is an added safety precaution to insure that the glass will not be drawn into contact with the metal housing due to vacuum-induced deformations. These vacuum pads are ball-bolt mounted

to a support arm which allows the pad to tilt. This gimbal effect minimizes bending stresses which may be introduced into the mirror during handling.

The dimensions of the pads determine the maximum load that can be lifted with this system, as well as the stresses produced in the material under the pad. The state of stress can be determined by representing this area as a circular plate simply supported at the edge and subjected to a uniform pressure. For this case, the maximum stress can be calculated using the following expression:

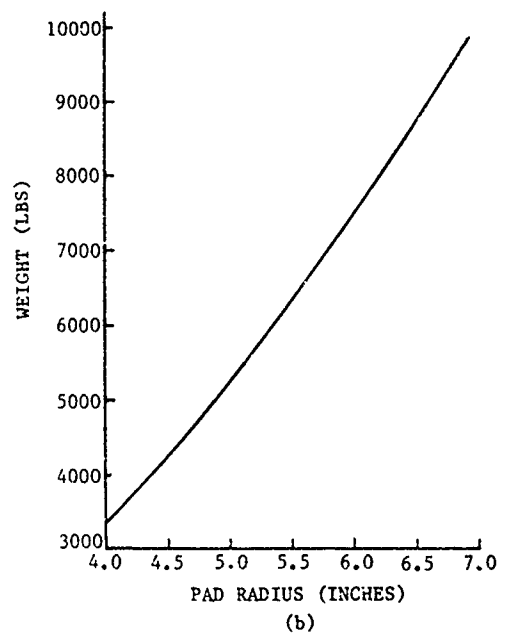
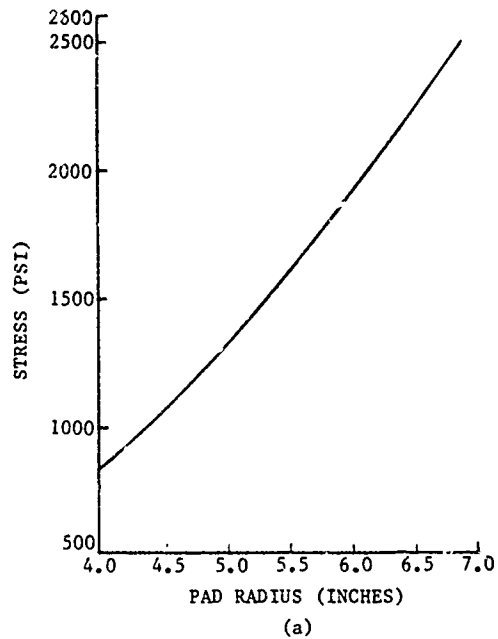
$$\sigma = \frac{3(3+\mu)qa^2}{8h^2}$$

where:

- μ = Poisson's ratio
- q = applied pressure (psi)
- a = pad radius (inches)
- h = plate thickness (inches)

The applied pressure is approximately 3/4 ATM, which is typical of vacuum levels produced in an existing Vac-U-Lift system. Graphs of glass stress versus pad radius, and maximum lifting force versus pad radius, are shown in Figure 2.2.1-3.

A good rule of thumb for mirror design is to keep stresses to approximately 1000 psi. Included within this allowable value are stress concentration factors resulting from the geometry of the core plate to faceplate interface of a



a. GLASS STRESS VERSUS PAD RADIUS
 b. LIFTING FORCE VERSUS PAD RADIUS

Figure 2.2.1-3

fusion-welded mirror. This allowable stress is overly restrictive for a thin sheet of glass that is continuous. Since the rupture stress for glass with an abraded surface is approximately 7000 psi, it is felt, for this situation, that the allowable stress can be increased to at least 2000 to 3000 psi without causing any problem. As shown in figure 2.2.1-3, a pad radius of 6.2 inches corresponds to a stress approximately 2000 psi and a lifting capacity of 8000 pounds.

This Vac-U-Lift system can also be used to lift a lightweight mirror. As noted in Table 2.2.1-1, the proposed 4.0-meter mirror weighs 3000 pounds. Since the maximum load capability of the lifting system is 3000 pounds, this particular mirror can be lifted by using only three pads. If this system is to be used to lift a lightweight mirror, the stresses produced under the vacuum pad must be determined. In order to approximate the state of stress under the pad, it will be assumed that the glass is clamped along points over the core plates and that a uniform pressure is applied to the faceplate. Using these assumptions, the maximum stress is given by the following expression:

$$\sigma = \frac{0.3078qb^2}{t^2}$$

$$\sigma = 217 \text{ psi}$$

where:

q = applied pressure, 11.025 psi

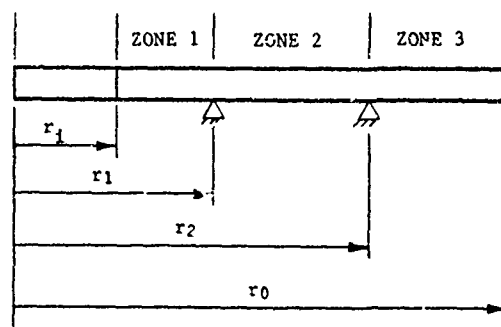
b = cell spacing, 4.0 inches

t = faceplate thickness, 0.5 inch

This is well below the 1000 psi allowable used in lightweight mirror design.

In addition to the stresses produced by the pressure differential, the glass will also be stressed due to gravity. Since the thin plate is much less rigid than a lightweight mirror, the gravity effects will be more critical for the case of handling the faceplate. It must also be noted that, in general, the mirror is required to safely withstand environmental loads that are more severe than handling loads.

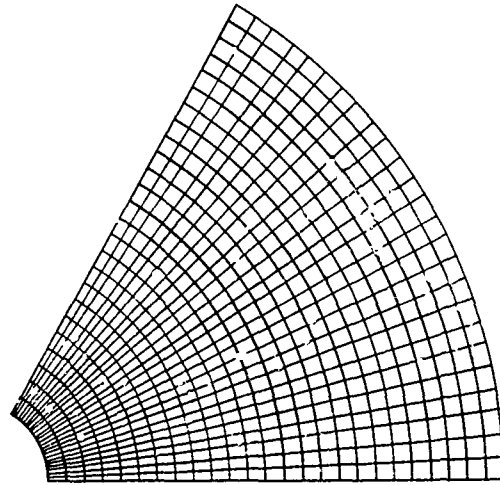
As shown in Figure 2.2.1-1, the pads are not located on the same radius. Since the deflection of the plate is dependent on the location of the pads, it is possible to locate these pads in an optimum fashion. To find the optimum location, it is assumed that the plate is supported on two rings (Figure 2.2.1-4). A simple finite element model was assembled to calculate plate deflections for various ring locations. The relative location of the rings was changed and the deflection in zones 1, 2, and 3 were compared. The optimum location is the one in which the maximum deflection in each zone is equal. For the 4-meter faceplate shown in Table 2.2.1-1, the optimum ring locations are at radii of 38 inches and 68 inches.



OPTIMUM RING SUPPORT FOR
4.0-METER FACESHEET

Figure 2.2.1-4

Having located the pads, stresses are calculated by using the finite element model shown in Figure 2.2.1-5. This model is a 60-degree segment in which symmetric boundary conditions are imposed on the edges to account for the remaining portion of the mirror. The pads are simulated by applying a uniform pressure over the pad area rather than "grounding" a single point. This technique minimizes stresses produced by the unrealistic single point boundary condition.



STRESS MODEL FLAT PLATE

Figure 2.2.1-5

This model will only be used to determine stresses for points outside of the pad area. The rubber annulus should effectively isolate the area inside the pads from stress produced by gravity loads. Although the model predicts large stresses in the pad area, this is a result of the support method chosen to simulate the pads. This method tends to smooth the stress distribution in the vicinity of the support points but it also forces all of the load to be carried by the material within the vacuum area. The only stresses that the material in the pad area will experience are those stresses needed to assure slope compatibility at the rubber annulus interface.

For a one-g load case, the maximum stress produced in the mirror is 975 psi. This occurs in an area immediately adjacent to the pad located on the 68-inch radius. The maximum stress is 686 psi in the area of the pad located on the 38-inch radius. A typical handling load requirement is 2.5 g's. This accounts for abrupt loads that may occur if the mirror is stopped suddenly. Since this is a linear system, the stresses can be scaled to simulate a 2.5-g load; thus, the maximum stress produced in the plate during handling is 2438 psi. This stress is within acceptable limits for a continuous piece of glass.

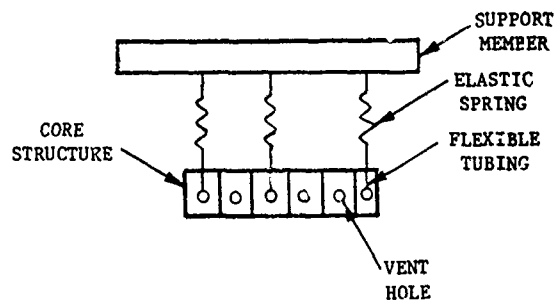
Since this Vac-U-Lift system has six pads, it would be advantageous if only three pads could support the glass plate. It would then be possible to independently power each set of vacuum pumps, thus providing a safety factor if service to a ring of pads should fail. Since the system is capable of lifting 8000 pounds, three pads are capable of holding the 3000 pound, 4.0-meter mirror, but a detailed analysis to determine mirror stresses in this situation would be required. It is possible to investigate the stresses for the flat plate with the model shown in Figure 2.2.1-5.

The weight of the mirror is supported by applying a uniform pressure over the pad area. For the case in which only the pads on the 38-inch radius are supporting the plate, the maximum 2.5-g induced stress is 6615 psi. In the case in which only the pads on the 68-inch radius are supporting the plate, the maximum 2.5-g induced stress is 4558 psi. The stresses produced by handling the plate with only three pads are not within the acceptable limits for a continuous piece of glass.

A Vac-U-Lift system, which employs six pads located on two diameters, can safely handle a large flexible flat plate similar to that used in a 4.0-meter monolithic mirror design. Although three pads are sufficient to support the weight of the glass plate, typical handling load levels will produce stresses which could fracture the plate.

After the mirror core is assembled, it is necessary to move this structure to other work stations for further processing, such as machining. Therefore, a method must be devised in which the core structure can be lifted in such a manner that the glass is not overstressed due to gravity loads. A proposed frit application method also requires that the core be dipped into the frit material, then withdrawn after the frit has time to adhere to the glass surface. Care must also be taken to assure that stresses produced by these adhesion forces are within acceptable limits.

The current method of lifting the core structure is shown in Figure 2.2.1-6. A flexible piece of tubing is inserted through the vent holes and attached to a rigid support member via an elastic spring. The spring produces a gimbal effect, while the flexible tubing assures an even load distribution at the glass interface. Although it is not necessary to lift the core structure at each vent hole, a sufficient number of points must be used to keep the stresses within acceptable limits.



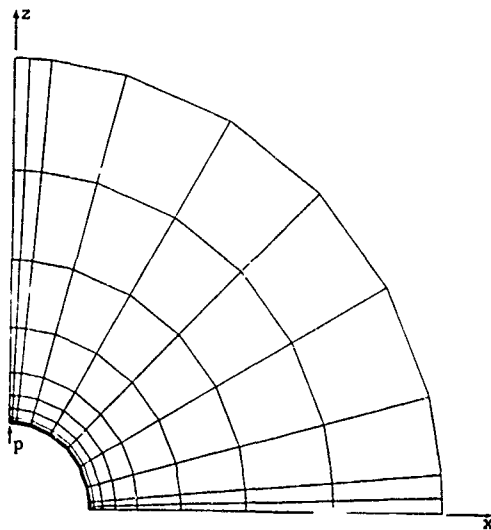
CORE LIFTING METHOD

Figure 2.2.1-6

Before the decision is made on the number of support points needed to lift the core structure, a reasonable estimate of misalignment error must be determined. Misalignment is a function of where the spring attaches to the lifting structure and where the flexible tubing interfaces with the core strut. A large separation between the lifting structure and the vent holes is beneficial since the direction of the load is dependent on the angle between the spring line of action and the core plate. A means of adjusting the location of the spring/lifting structure attachment point is also required. This can be accomplished by using an eye-bolt inserted into an oversized hole.

Distances between lifting points can be measured during assembly of the core structure. This information can then be used to locate the attachment points on the lifting structure. It is not unreasonable to keep the misalignment errors to less than 2 degrees with this method. Restraints must also be placed at the edges of the core structure to prevent swinging during movement of the structure.

2.2.1.1 Core Stresses - The stresses caused by lifting the core were evaluated, using the dimensions of the 4.0-meter design shown in Table 2.2.1-1, and a detailed model of the area around a vent hole (Figure 2.2.1-7) was generated.



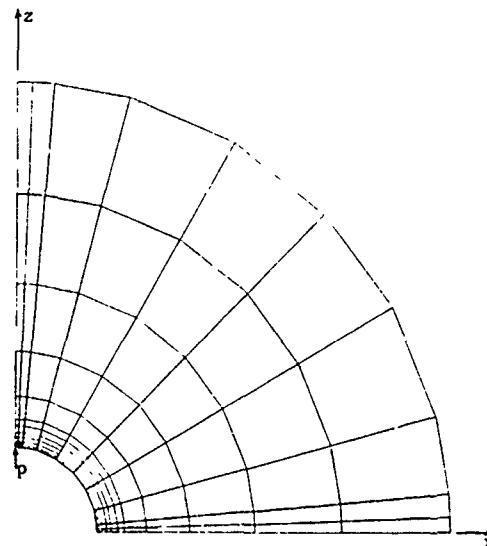
COARSE MODEL OF CORE PLATE
FOR STRESS CALCULATION

Figure 2.2.1-7

As expected, the highest stresses occurred in the same elements and maximum difference in stress magnitudes was only 0.22 percent, as shown in Table 2.2.1-2.

The results indicate that the element mesh of Figure 2.2.1-7 is sufficient. This model was then incorporated into a one-eighth-symmetric model of a section of the mirror core, as shown in Figure 2.2.1-9. Assuming the edges of the modeled core section to be simply supported, $+x$, $+y$, and $+z$ loads were applied separately at the top edge of the

Fixing the outer circumference boundary of this one-quarter-symmetric model, a $+z$ load was applied at the point indicated. More detail was added, as shown in Figure 2.2.1-8, to determine if the element mesh was fine enough to insure convergence of the results, and the same evaluation procedure was followed.

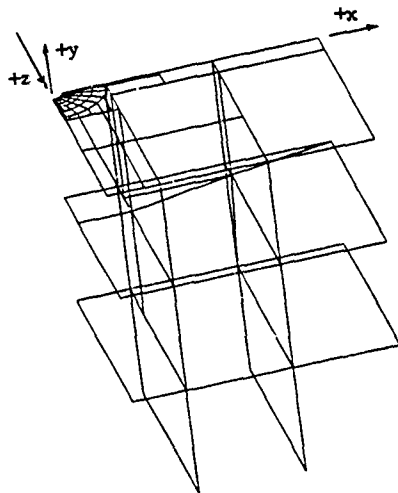


REFINED MODEL OF
CORE PLATE FOR
STRESS CALCULATION

Figure 2.2.1-8

Table 2.2.1-2
CORE STRESS CONVERGENCE TEST

	MODEL 1	MODEL 2	PERCENT DIFFERENCE
MAXIMUM TENSION (PSI)	50.03	49.92	0.22
MAXIMUM COMPRESSION (PSI)	-706.66	-706.45	0.03



MODEL OF CORE STRUCTURE
Figure 2.2.1-9

it is possible to determine stress as a function of the angle, ϕ , as shown in Figure 2.2.1-10. Results of this exercise, which are shown in Figure 2.2.1-11, can be used to determine misalignment tolerances.

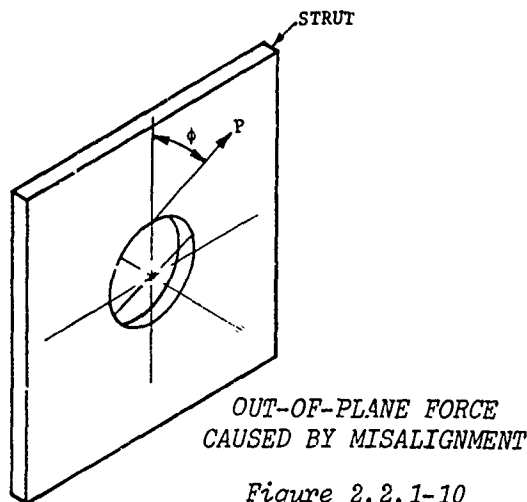


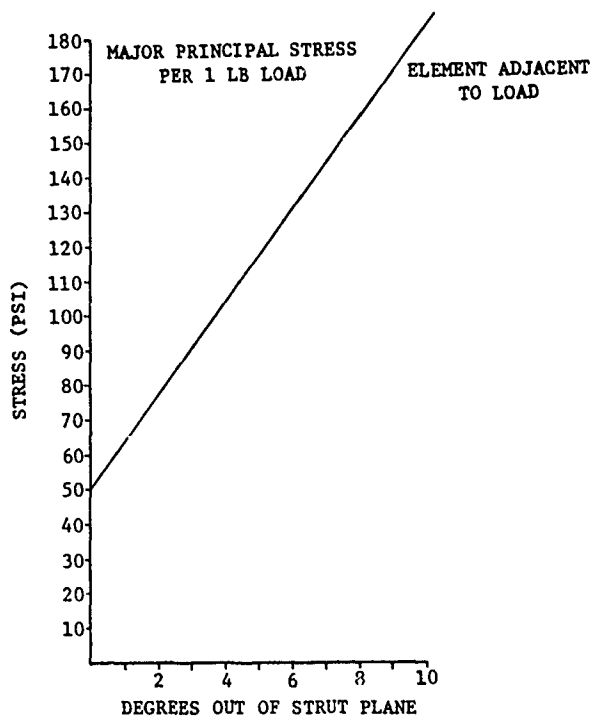
Figure 2.2.1-10

vent hole. Stress values in the mirror core were obtained by giving the grid points, which are located on the planes of symmetry, the appropriate symmetric or antisymmetric boundary conditions. The highest stresses for a one-pound load are summarized in Table 2.2.1-3.

It is evident from Table 2.2.1-3 that the core stresses are very sensitive to loads acting in a direction perpendicular to the core strut. Using these unit load cases,

LOAD CASE	MAXIMUM TENSILE (PSI)	MAXIMUM COMPRESSIVE (PSI)	MAXIMUM SHEAR (PSI)
+x	14.00	-376.81	192.96
+y	933.00	-933.00	508.00
+z	50.01	-707.14	304.88

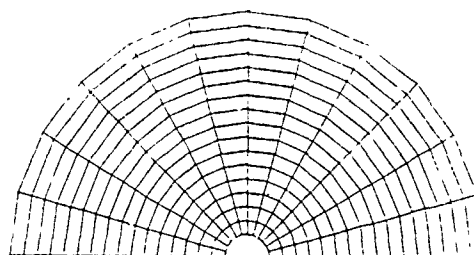
The loading at each point from which the mirror core is supported is determined by the use of the 180-degree model shown in Figure 2.2.1-12. This model uses the NASTRAN CQUAD4 plate element which makes it possible to directly input the membrane, bending, and shear stiffness properties associated with the 4.0-meter core structure. Forty-four points in the model were connected to ground using elastic springs.



MAJOR PRINCIPAL STRESS VERSUS DIRECTION OF APPLIED LOAD

Figure 2.2.1-11

In order to determine if the reaction force was dependent on the stiffness of the springs, a series of computer simulations were run in which the spring rate was varied from 100 pounds per inch to 10,000 pounds per inch. Results of this exercise are shown in Table 2.2.1-4.



DISTRIBUTED STIFFNESS MODEL OF CORE STRUCTURE

Figure 2.2.1-12

SPRING CONSTANT (LBS/IN.)	MAXIMUM REACTION FORCE (LBS)	MINIMUM REACTION FORCE (LBS)
100	31.319	31.298
1000	31.384	31.176
10000	31.965	30.047

This indicates that the reaction forces are not strongly influenced by the stiffness of the spring. There is only a 2 percent difference between the maximum reaction force obtained

when using 10,000 pounds per inch springs versus using 100 pounds per inch springs; however, the most uniform distribution occurs when using the most flexible springs. For the case in which 100 pounds per inch springs are used, there is virtually no difference between the maximum and minimum reaction forces. If it is necessary to use more support points, a reasonable estimate of the weight supported by each of these points can be determined

by dividing the total core weight by the number of support points. This also assumes that the support points are reasonably spaced. It may be necessary to use more support points if it is felt that the stresses produced by handling loads are not within acceptable limits.

From Figure 2.2.1-11, the stress produced by a 1-pound load for a 2-degree misalignment is 75 psi. Referring to Table 2.2.1-4, the reaction force for a system employing 44 points is 31.32 pounds; therefore, a 2.5-g handling load produces a tensile stress of 5873 psi, which is unacceptable. Since the finite element model accounts for stress concentrations resulting from the strut geometry, it is felt that the allowable glass stress can be raised to 2000 psi. Using this allowable, it is possible to determine the number of points required to lift the core structure. Assuming a 1400-pound core and a uniform distribution of weight between the lifting points, the number of support points can be calculated from the following expression:

$$\text{Number of points} = \frac{(2.5)(75)(1400)}{2000}$$

$$\text{Number of points} = 131$$

Since there are a large number of points and the alignment is critical, the lifting structure should be rectangular and should essentially resemble the core structure being handled.

A proposed method for applying the frit to the glass is via a "dipping" process. A uniform line load of 1 pound per linear inch is applied to the bottom of the core structure to simulate the adhesion loads produced during this process, and this load is reacted by "grounding" one point at the top of the vent hole. The maximum stress produced by this load is 26.8 psi. The actual magnitude of the load produced by the frit dip process was measured at Corning Glass Works. This force is dependent on the rate at which the core is removed from the frit. Various lifting rates, typical of the rates proposed for this procedure, were tested and the maximum measured load was 0.235 pound per inch. There is no stress problem for loads of this magnitude.

In conclusion, it is possible to handle a large core structure in a manner similar to the methods currently in use. A minimum of 131 lifting points must be used, and care must be taken to control the line of action of the lifting force.

2.2.2 Mirror Furnacing Support Analysis

In addition to being concerned specifically with the design of the furnace, careful attention must be paid to the manner in which the mirror blank is supported during the firing operation. If there are not enough points supporting the mirror blank, gravity-induced deformation will cause the faceplate to separate from the core, resulting in unacceptable bonding due to lack of frit viscous flow at the firing temperature. Coefficient of expansion variations through the faceplate thickness also produce thermal deformations that cause the faceplate to separate from the core.

It was decided to support the mirror blank on "soft" springs located on 4-inch centers. For points this closely spaced, gravity-induced deformations are negligible and, thus, are not an issue. The support springs should be soft to allow the mirror blank weight to be equally distributed between all points. It was shown in paragraph 2.2.1 that a spring rate of 100 pounds per square inch is sufficiently soft to permit relatively uniform distribution of load. The springs used in the furnace have a spring rate of 40 pounds per square inch. Another design feature of the support springs is that they must be adjustable to accommodate mirror blanks with curved back plates.

The thermal deformation of the faceplate can be offset by placing weights on the front surface of the mirror blank during the firing operation. In order to determine how much weight must be added, the thermal deformation must be calculated. Assuming the worst case, coefficient of thermal expansion variation between the front and back of the faceplate is 0.04×10^{-6} in./in./ $^{\circ}\text{C}$. If it is assumed that this variation is linear and that the edge of the plate is free to rotate, the sag can be calculated by using the following expression.

$$\text{sag} = \frac{a^2 \Delta \alpha T}{2h} \quad (1)$$

where:

- a = outside radius (inches)
- $\Delta \alpha$ = coefficient of expansion mismatch (inch/inch/ $^{\circ}\text{C}$)
- T = firing temperature ($^{\circ}\text{C}$)
- h = faceplate thickness (inches)

In order to estimate how much weight must be added, it is assumed that the plate is simply supported and that the weight is uniformly distributed across the front surface. For this case the sag is given by the following expression.

$$\text{sag} = \frac{3(5+\mu)(1-\mu)a^4 W}{16Eh^3 \pi (a^2 - b^2)} \quad (2)$$

where:

- a = outside radius (inches)
- b = inside radius (inches)
- W = weight (pounds)
- μ = Poisson's ratio
- E = Young's modulus (pounds per square inch)
- h = faceplate thickness (inches)

By equating equations 1 and 2, it is possible to solve for the weight needed to keep the faceplate in contact with the core structure during the firing operation.

$$W = \frac{8\Delta \alpha T E h^2 \pi (a^2 - b^2)}{3(5+\mu)(1-\mu)a^2} \quad (3)$$

For a typical 4.0-meter monolithic design, the faceplate thickness, and inside and outside radii are 0.5 inch, 24 inches, and 80 inches, respectively. Using these parameters, 157 pounds are needed to counteract the thermal deformation of the faceplate.

2.3 HEAT LOAD TESTING AND ANALYSIS

2.3.1 0.5-Meter Performance Analysis

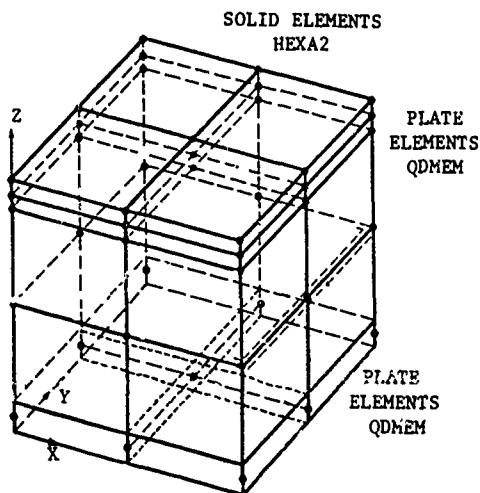
The thermoelastic response of a lightweight mirror is a function of the thermal gradients in the mirror as well as the stiffness of the mirror. For the test case being studied, it is assumed that the front surface of the mirror is uniformly irradiated over a 19-inch diameter and that all external surfaces are insulated. A thermal finite element analysis was performed to determine the temperature profile; this profile was then input to a structural model to determine the distortion of the mirror. The Zernike aberration content of the deflected surface was then analyzed using an optical evaluation program.

2.3.1.1 Finite Element Models - Three finite element models were generated.

- Single Cell Model - To check the effect of various thermal modeling parameters (Figure 2.3.1-1).
- Thermal Model - To provide temperature profiles at selected times (Figures 2.3.1-2, 3, and 4).
- Structural Model - To calculate distortion of the mirror due to gravity and thermal effects (Figures 2.3.1-5 and 6).

All finite element analyses were performed with MSC/NASTRAN through the Control Data Corporation CYBERNET time-sharing service.

Single Cell Model - A model of a single cell was developed to test the sensitivity of various modeling parameters used in the thermal analysis. The top plate was modeled with two layers of HEXA2 solid, eight-node elements. Both the core plates and bottom plate were modeled with QDMEM plate elements (see Figure 2.3.1-1). To determine the validity of this NASTRAN model, another more detailed single cell model was assembled (see Figure 2.3.1-2). This model was run using the SATAN thermal analysis program, which is based on finite difference rather than finite element theory. Both NASTRAN and SATAN

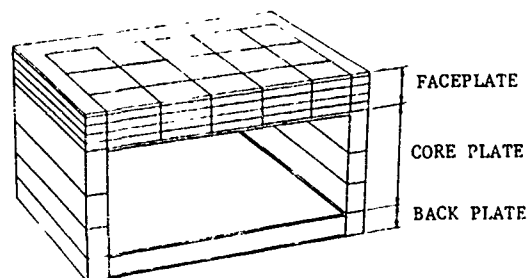


NASTRAN SINGLE CELL MODEL

Figure 2.3.1-1

single cell models predict the same temperature rise for the center cell point on the top surface; however, there is some difference between the in-plane temperature profile predicted by the two models. The NASTRAN model predicts approximately a 10°F difference between the center cell point and a point over the center of the core, while the SATAN model predicts a 6°F difference between these points. Both single cell models predict that the back plate temperature will not rise; thus, it is felt that the NASTRAN model is sufficiently accurate for the analysis.

Due to the relatively simple geometry of the mirror cell, radiation view factors were calculated in closed form. Two cases for radiation were investigated. In the first case, the inside of the cell was divided into six radiation surfaces (NASTRAN HBDY elements), one covering each interior face. In the second case each interior cell face was divided into four radiation surfaces, for a total of 24. Both cases were run for the thermal transient analysis to see if there was a significant difference in results. Temperatures calculated for the two cases varied by less than 1°F . It was therefore decided to use six radiation surfaces per cell in the full thermal model.

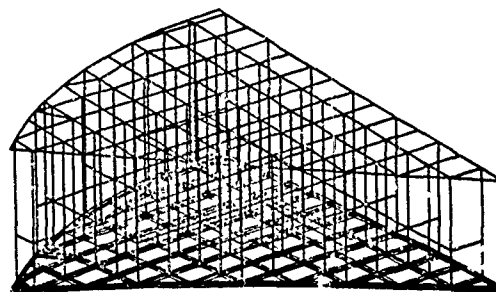


SATAN SINGLE CELL MODEL

Figure 2.3.1-2

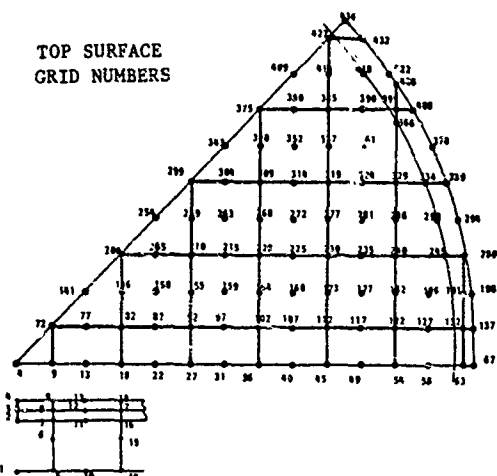
The sensitivity of the temperature results to the integration time step was also tested with the time step set equal to 1 second, 0.25 second, and 0.0625 second. There was still no significant variation in the results.

Thermal Model - The complete thermal model is shown in Figure 2.3.1-3. The top surface detail is shown in Figure 2.3.1-4. The HEXA2 and QDMEM elements were used with the addition of PENTA solid and TRIA3 triangular plate elements, as required, at the boundaries. HBDY elements were used to model the internal radiation, with six surfaces used per cell. HEDY elements were also overlayed on the top surface in order to absorb the applied heat flux.



THERMAL MODEL COMPUTER PLOT

Figure 2.3.1-3



THERMAL MODEL GRID POINT NUMBERING

Figure 2.3.1-4

A 45-degree segment of the total mirror was modeled (the smallest segment for circular symmetry), with the dividing lines of the mirror going through the cells along the X-axis and going diagonally through the cells at 45 degrees. It was assumed that there should be no net heat transfer across these lines in the actual mirror. The boundary conditions along the dividing lines for radiation were handled by putting a radiation surface of very low emissivity (0.01) across the open boundary acting as a reflector.

In the case of conduction, no special boundary conditions were required along the dividing lines.

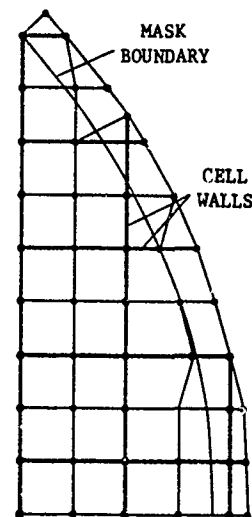
View factors were calculated for the cells, and the product of view factor and surface area was input in the form of a radiation matrix.

Heat flux was input to the top surface of the model through HBDY elements overlayed onto the top of the HEXA2 and PENTA elements. A mask covered a

0.50-inch ring around the outside of the top surface, blocking any radiation in the actual model. No heat flux was applied to elements under the mask. Where the mask cut across an element, the heat flux at the various nodes was varied appropriately. The mask area is shown in detail in Figure 2.3.1-5. QBDY1 and QBDY2 cards were used for heat flux input.

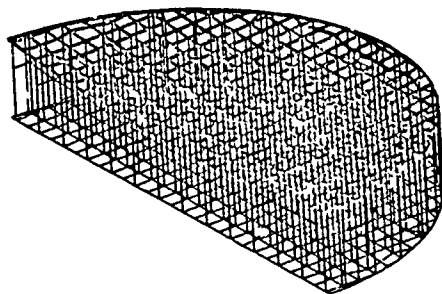
A post is located at each intersection of the cell walls in the mirror. The cell walls are 0.050-inch thick and the post cross section is 0.150-inch by 0.150-inch. The posts were not explicitly included in the model, but the cell walls were increased to 0.05583-inch thick to give an equivalent path of conduction.

The initial temperature of the model was set at 68°F. One-second time steps were used to 80 seconds.



THERMAL MODEL MASK AREA DETAILS

Figure 2.3.1-5

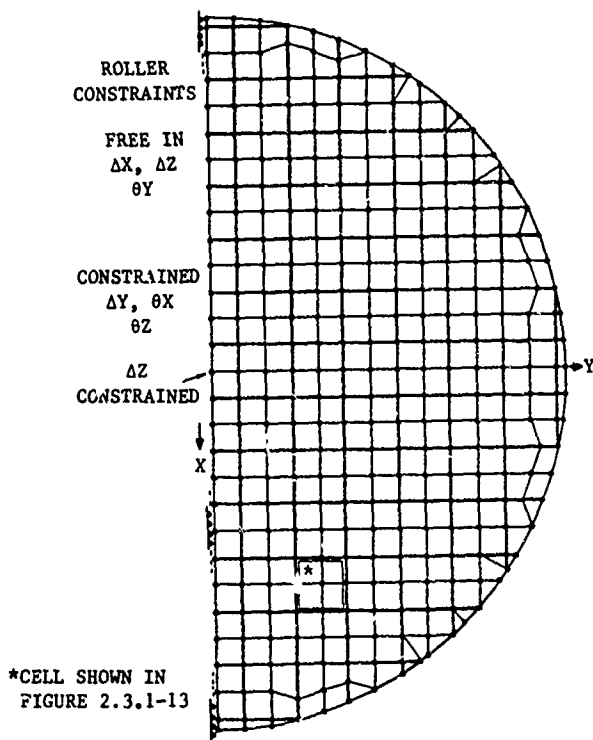


STRUCTURAL MODEL COMPUTER PLOT

Figure 2.3.1-6

Structural Model - A structural model of one half of the mirror was formed, as shown in Figures 2.3.1-6 and 2.3.1-7. The coordinate axes were changed to put the X-axis on the dividing line. Solid elements, HEXA and PENTA, were used to model the top plate. The same element distribution was used in the structural model as the thermal model. The plate elements used to model the cell walls and bottom plate were the QUAD4 and CTRIA3.

The mirror was modeled as resting on a pair of V-blocks, although only one V-block was included in the model. The V-block constraint was applied to



STRUCTURAL MODEL TOP SURFACE DETAIL

Figure 2.3.1-7

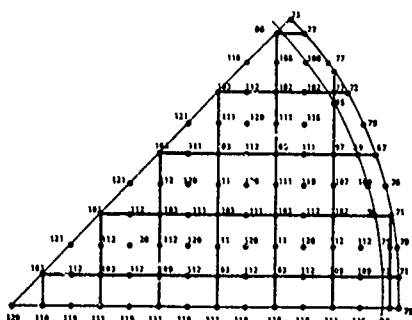
Temperature profiles from the thermal transient analysis were saved for 60 seconds and 80 seconds, and were used as input to the structural analysis. Because the structural model was four times the size of the thermal model, it was necessary to duplicate the temperatures from the thermal analysis for the structural model. A separate FORTRAN program was developed by STI for this purpose.

The structural model was run, in all cases, as a static analysis, NASTRAN solution 24.

Thermal Analysis Results - Temperatures at the top surface grid points are shown in Figures 2.3.1-8 and 2.3.1-9 for 60 seconds and 80 seconds, respectively. Temperatures through the thickness of the mirror (Z gradient) along the X-axis dividing line are shown in Figures 2.3.1-10 and 2.3.1-11.

the model at a point 45-degrees from the dividing line, and constrained displacement in the X-direction at the node on the bottom plate and the middle of the three nodes on the top plate. Only one of the three nodes of the top plate was constrained so that the top plate would still be free to rotate about its middle node. Along the dividing line, displacement was constrained in the normal (Y) direction. Rotations about the X- and Z-direction was applied at the center point of the dividing line (mirror center) at the top surface.

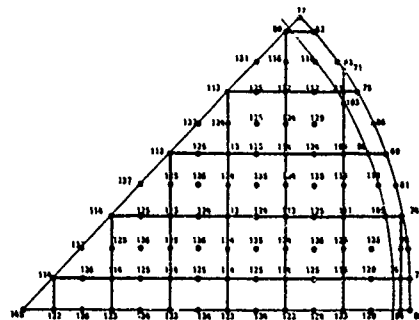
Loadings to the structural model included three separate cases: gravity load, two thermal loads, and a pressure load applied to the top surface.



NOTE: TEMPERATURES ROUNDED OFF TO THE NEAREST DEGREE

TOP SURFACE TEMPERATURES--60 SECONDS

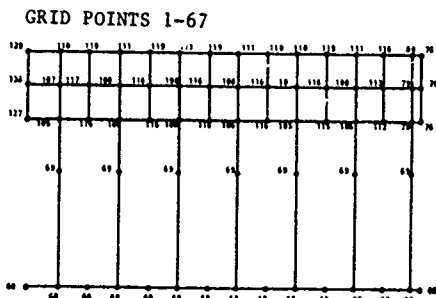
Figure 2.3.1-8



NOTE: TEMPERATURES ROUNDED OFF TO THE NEAREST DEGREE

TOP SURFACE TEMPERATURES
FINAL RUN--80 SECONDS

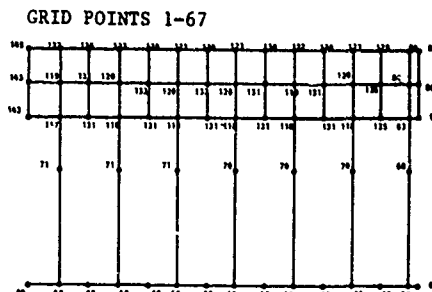
Figure 2.3.1-9



NOTE: TEMPERATURES ROUNDED OFF TO THE NEAREST DEGREE

TEMPERATURE PROFILES
Z-DIRECTION 60 SECONDS

Figure 2.3.1-10

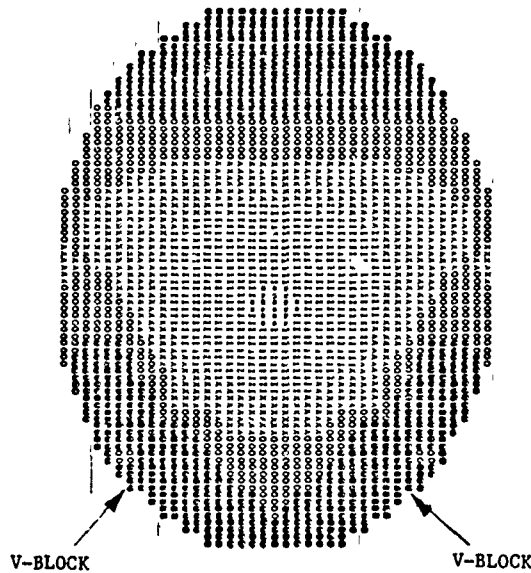


NOTE: TEMPERATURES ROUNDED OFF TO THE NEAREST DEGREE

TEMPERATURE PROFILES
Z-DIRECTION 80 SECONDS

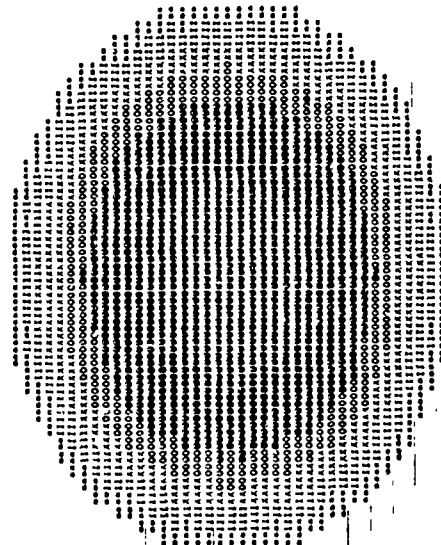
Figure 2.3.1-11

Structural Analysis Results - Plots of displacements in the Z-direction along the dividing lines are given in Figures 2.3.1-12 and 2.3.1-13 for the gravity load and temperature load cases. The top surface displacements for one cell (indicated in Figure 2.3.1-7) are shown in Figure 2.3.1-14.



SURFACE DEFLECTION - GRAVITY LOAD

Figure 2.3.1-12



SURFACE DEFLECTIONS - 80 SECOND EXPOSURE

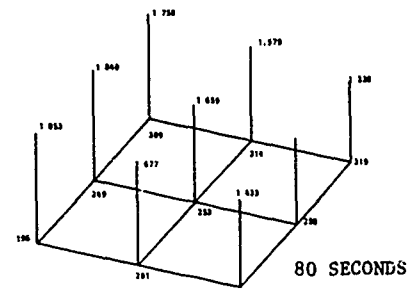
Figure 2.3.1-13

2.3.1.2 Discussion of Results -

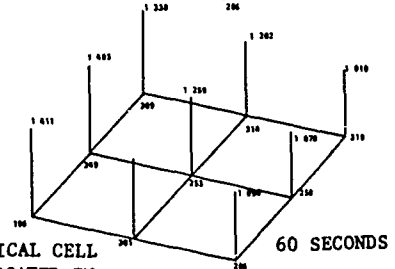
Single Cell Model - Cases comparing the relative effects of radiation and conduction showed that the finite element model predicted conduction to be the dominant mode of heat transfer; however, there appeared to be virtually no radiation heat transfer. Although preliminary analysis indicated that radiation is not a significant factor for an 80-second exposure, the radiation exchange predicted by NASTRAN was much less than anticipated.

In order to further test the radiation effects, the single cell radiation

Z DISPLACEMENTS,
10⁻⁶ INCHES



80 SECONDS



60 SECONDS

TYPICAL CELL INDICATED IN FIGURE 2.3.1-6

TOP SURFACE DEFORMATIONS

Figure 2.3.1-14

matrix was adjusted to include only radiation elements (HBDY) on the bottom side of the top plate and the top side of the bottom plate. The view factors were adjusted so that all radiant energy leaving a top plate element would be absorbed by the element directly opposite on the bottom plate. This had the effect of reducing the radiation exchange to a one-dimensional problem for each pair of radiation elements. A hand calculation was performed using the average temperature (at 80 seconds) of one element pair to calculate the net heat flux from top plate to back. The heat flux calculated by hand was an order of magnitude greater than the heat flux output by NASTRAN for the element pair at the same time (80 seconds).

It was observed that there was a temperature difference of about 9°F between the grid point on the top surface in the center of the cell and points on the top surface over the middle of the cell wall at 80 seconds. There was a temperature difference of about 18°F between the top surface mid-cell point and grid points on the top surface at the corners of the cell after 80 seconds. These temperature differentials were larger than anticipated. This is probably related to the small radiation heat exchange. If the radiation heat exchange is small, the mid-cell points must transfer more heat down through the cell by conduction, thus giving a larger temperature difference between the mid-point and the cell walls.

Thermal Model - The thermal model showed the same basic temperature distributions over the cells as the single cell model. Temperatures along the dividing lines were consistent with temperatures in the center of the model. An exception was the mirror center point, a cell midpoint, which had a temperature at the top surface of about 145°F compared to other typical mid-cell temperatures of about 135°F .

If the radiation heat transfer is less than expected, this would give a larger temperature difference between top plate and bottom.

Temperatures of points at or near the mask were significantly lower than those in the fully heated area. It should be noted that the mask caused an extremely high flux gradient across a number of elements. The accuracy of results at a loading discontinuity such as this cannot be expected to be as good as at an area a on the applied loading. This is characteristic of any finite element method. In addition, MacNeal-Schwendler has warned of problems with their PENTA and TRIA3 elements. Where a high flux gradient is applied, some nodes may actually drop in temperature. The same problems exist with the HEXA and QUAD4 elements. The HEXA and QUAD4 elements can be substituted, but no replacement elements are available for the PENTA and TRIA3.

Structural Model - The static deflection analyses performed with the structural model gave results which appeared to be consistent with the loadings used in each case.

a. Gravity Load

The results of this load case, with acceleration due to gravity acting in the X direction gave Z displacements shown in Figure 2.3.1-11. These deflections are with respect to a best fit plane. Due to the constraint put on the top surface midpoint, all displacements are relative to that point. Since the center of gravity is located toward the back plate of the mirror, gravity causes the mirror to both rotate and bend about the horizontal axis. In addition, the V-block constraints produce the triangular or trefoil pattern seen in this figure.

b. Thermal Load

The contour map of surface deformations for an 80-second exposure is shown in Figure 2.3.1-12. Surface deformations for a 60-second exposure are of the same general shape. The temperature differential between the front and back surface

of the mirror would produce this deflection pattern. From this figure, it appears that the in-plane gradients are not causing appreciable higher order aberrations. Also the variation in deflection across the top surface of each cell (quilting) does not appear to be as significant as the overall distortion (Figure 2.3.1-13).

A more detailed discussion of the results is presented in Section 2.3.4.

2.3.2 0.5-Meter Mirror Heat Load Test Configuration Evaluation

2.3.2.1 Introduction - Two irradiation response tests with the 0.5-meter diameter mirror were conducted at the Itek Corporation facility at Lexington, Massachusetts under Subcontract No. 60-2870-91760 (see Figures 2.3.2-1 and 2.3.2-2).

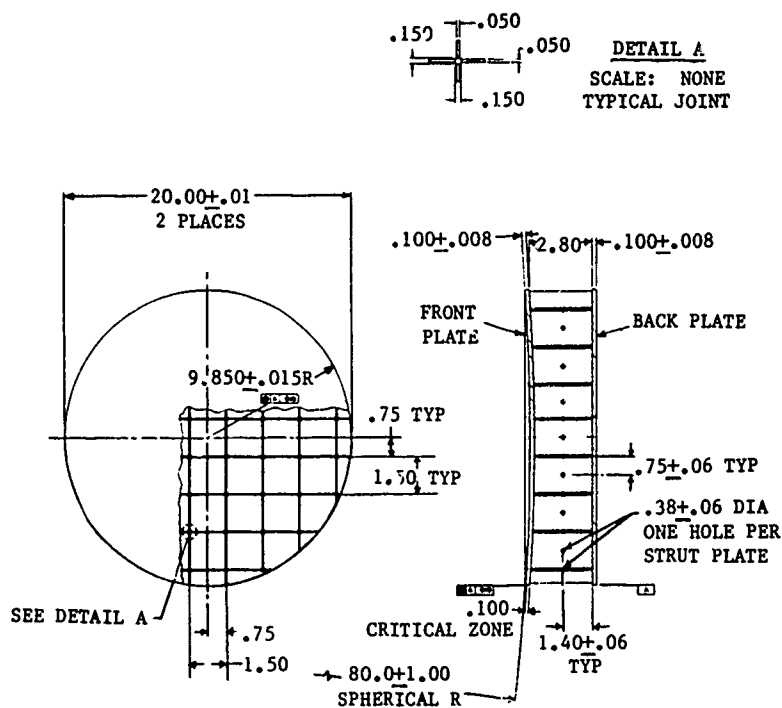
The primary objective of the test effort was to interferometrically measure and record the optical surface figure degradation of the 0.5-meter mirror during a period of thermal

irradiation. Each Test was performed in the low pressure Dynamic Resolution Test (DRT) chamber at the test site. An existing high intensity irradiation simulator, equipped with eight elliptical infrared in-line heater assemblies, was employed to simulate the thermal load characteristics.



ULETM ULTRA LIGHTWEIGHT FRIT-BONDED MIRROR

Figure 2.3.2-1

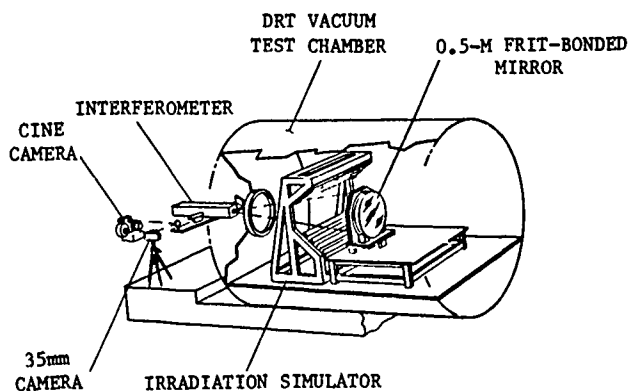


0.5-METER DIAMETER FRIT-BONDED ULE MIRROR
(80-INCH RADIUS OF CURVATURE)

Figure 2.3.2-2

Two motorized cameras (35mm SLK and 16mm CINE High Speed), shown in Figure 2.3.2-3, were used to record interferometric data during the 80-second test period. The mirror was thermally instrumented, and the thermal profile for each test was recorded.

2.3.2.2 Test Description - As shown in Table 2.3.2-1, identical test parameters were employed for each of the two irradiation response tests.



IRRADIATION RESPONSE TEST CONFIGURATION
(Photo shown in Figure 2.3.2-15)

Figure 2.3.2-3

Table 2.3.2-1
IRRADIATION RESPONSE TESTS

TEST PARAMETERS:		
• IRRADIATION DURATION PERIOD.	80 SECONDS	
• INCIDENT FLUX LEVEL.	4.5 KW/M ² @ 68.8% COATING ABSORPTIVITY	
• FLUX UNIFORMITY OVER MIRROR SURFACE. . . .	4.5 KW/M ² ± 15% ADJUSTED TO VACUUM LEVEL 15 MICRONS	
ACTUAL TEST CONDITIONS	FIRST ORIENTATION	SECOND ORIENTATION
• IRRADIATION DURATION	80 SECONDS	80 SECONDS
• AVERAGE INCIDENT FLUX LEVEL	4.43 KW/M ²	4.45 KW/M ²
• AVERAGE ABSORBED FLUX	3.05 KW/M ²	3.06 KW/M ²
ACTUAL TEST CONDITIONS	PRE-TEST SURVEY	POST-TEST SURVEY
• FLUX UNIFORMITY FOR MIRROR SURFACE AREA ADJUSTED VACUUM LEVEL 15 MICRONS	4.71 KW/M ² +11.9% -10.8%	4.86 KW/M ² +6.6% -10.6%

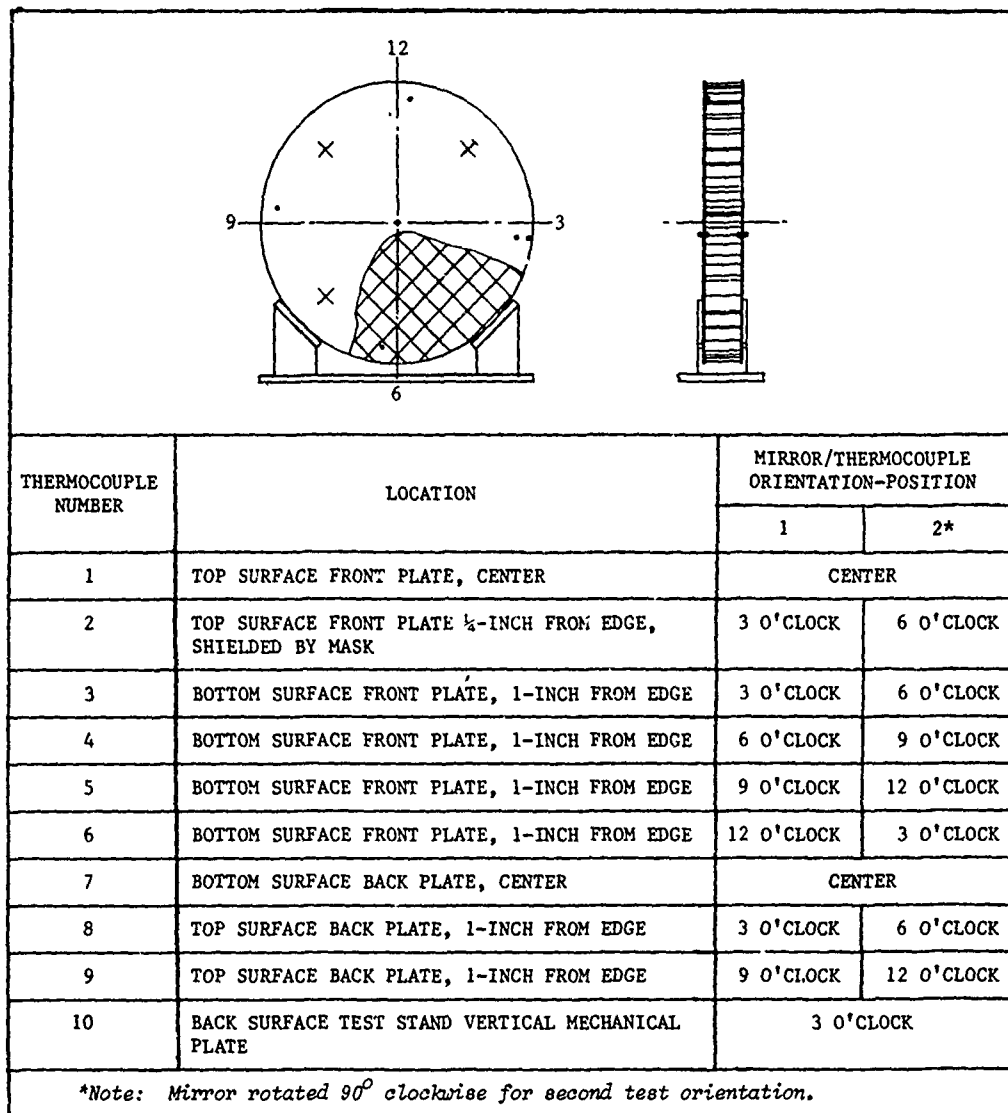
In the first test (first orientation), the mirror was positioned vertically with the orthogonal mirror core structure perpendicular to the mount support pads of the mirror test support. For the second test (second orientation), the

mirror was rotated 90 degrees clockwise to allow for interferometric averaging of the one-g, mount-induced load deformation of each orientation.

Each test period was preceded by a system and instrumentation checkout. This was followed by the chamber "pump down" to a pressure level of 15±10 microns for a period of mirror thermal stabilization to a test requirements of ±0.2⁰F for all thermocouple locations. At thermal equilibrium the vacuum pumps were shut off, and the test sequence was initiated. At this time, the 35mm SLR camera, the 16mm CINE camera, and the irradiation simulator lamps were powered simultaneously.

Thermal data was recorded at a scan rate of two channels per second for the first 180 seconds, and reduced to one ten channel scan per minute for the remainder of the monitoring period.

2.3.2.3 Thermal Data Acquisition and Summary - A ten channel Fluke 2200B Datalogger recorder was employed for thermal test data acquisition. Nine thermocouples were attached at selected mirror locations (Figure 2.3.2-4).



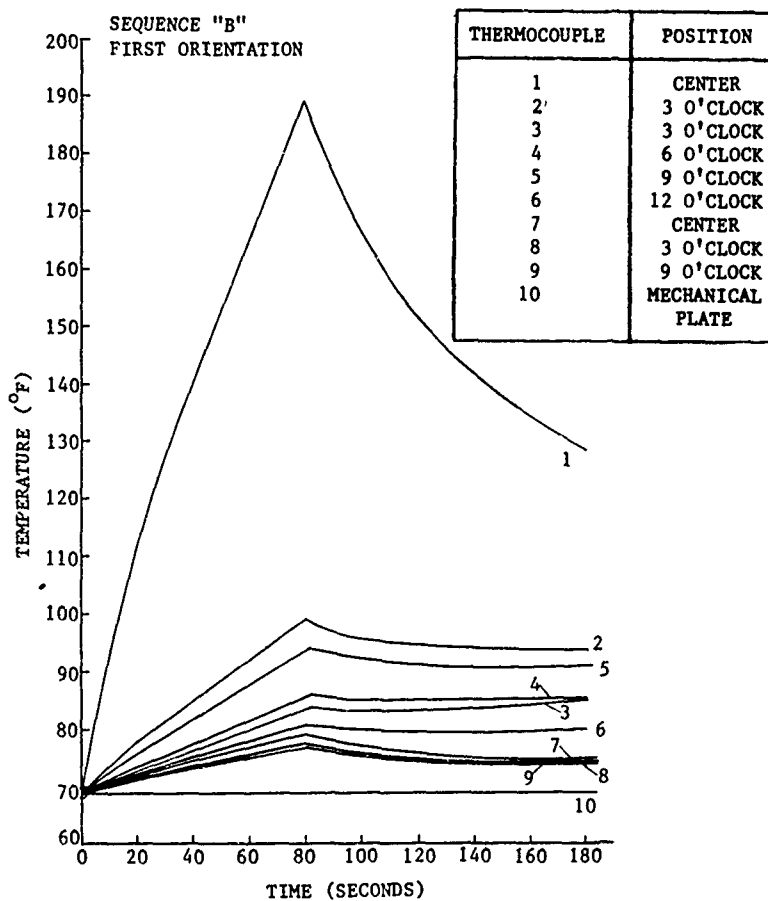
MIRROR TEST POSITION (FIRST ORIENTATION BASELINE)

Figure 2.3.2-4

Thermocouples 1 and 2 were attached to the front surface of the front plate at the center and 3 o'clock positions. Thermocouples 3, 4, 5, and 6 were

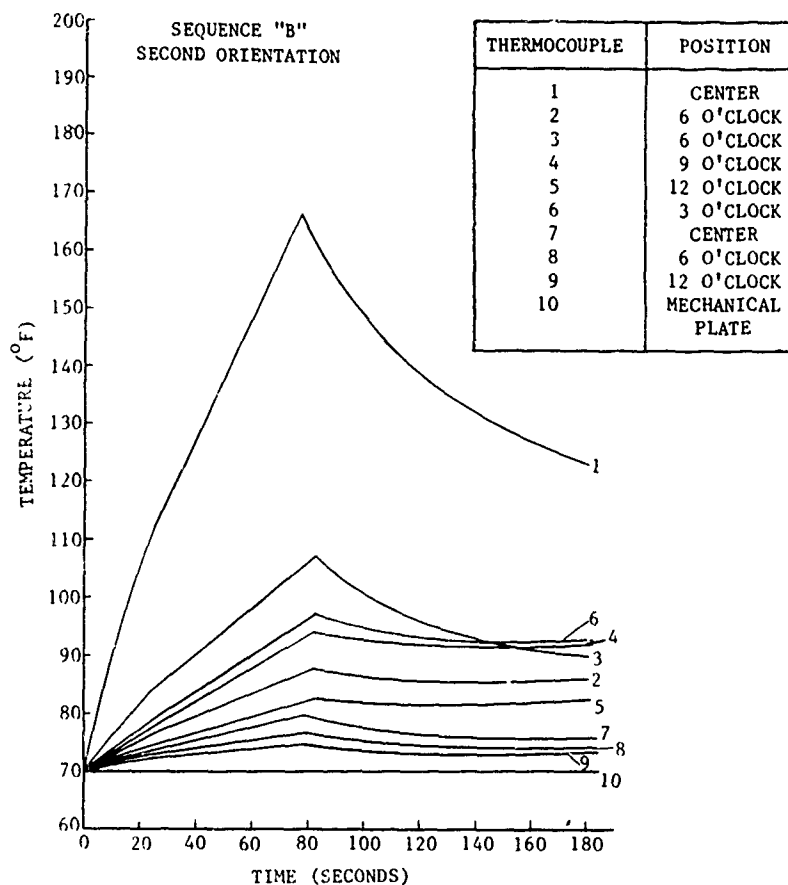
attached to the back surface of the front plate at the 3, 6, 9, and 12 o'clock positions. Thermocouples 8 and 9 were mounted on the front surface of the back plate at the 3 and 9 o'clock positions. Thermocouple 7 was mounted on the back surface of the back plate at the center position. Thermocouples 1 and 2 were primarily positioned to record front to back plate axial gradients for the nonirradiation portion of the tests. Each of the other thermocouples provide both axial and radial thermal gradient comparisons. The tenth thermocouple was attached to the rear surface of the mirror support stand vertical mechanical plate at 3 o'clock. This position was selected to monitor thermal load characteristics at the front surface of the insulation blanket interleaved between the mechanical plate and mirror edge.

Thermal data plots for each test are displayed in Figures 2.3.2-5 and 2.3.2-6. Two significant data dissimilarities are exhibited between the two tests. Peak temperatures for the front plate center and six o'clock positions were 21.8°F lower and 19.7°F higher, respectively, for the second test. A review of thermal data from two preliminary tests, shown in Figure 2.3.2-7, exhibited correlative data substantiating the first test center position thermal profile. A comparison of the remaining



IRRADIATION RESPONSE TEST

Figure 2.3.2-5



IRRADIATION RESPONSE TEST

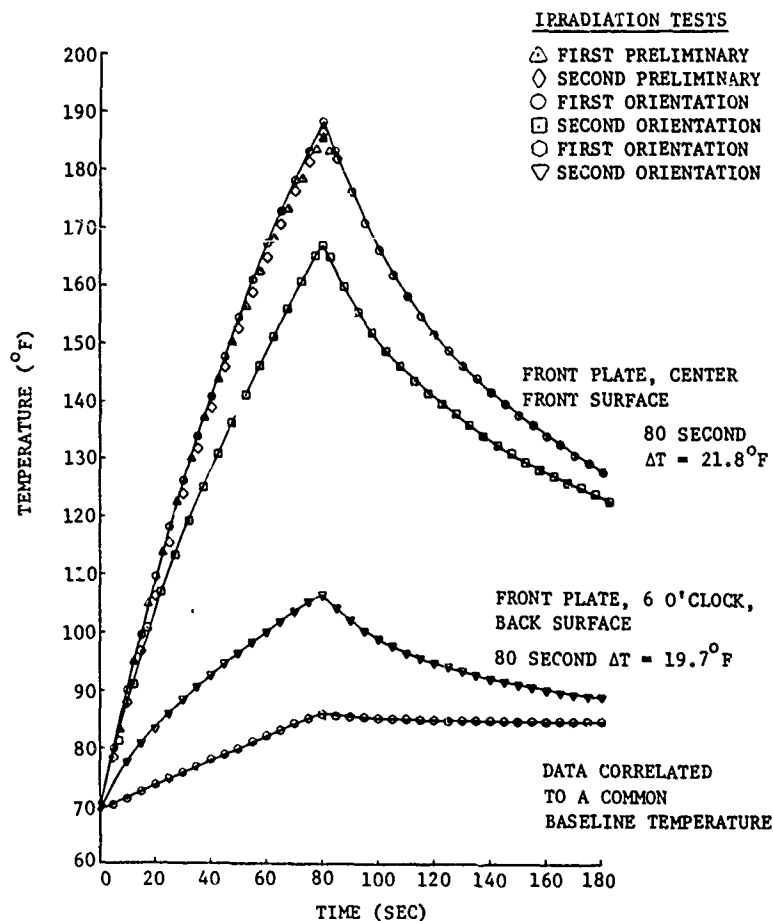
Figure 2.3.2-6

data points for the two orientation tests indicated that the average temperature for the second test was actually slightly higher, a fact substantiated by flux transducer measurements shown in Table 2.3.2-1.

Considerable effort was expended to provide a uniform irradiation flux level for the test series. Analysis of the thermal data, displayed in Figures 2.3.2-8 through 2.3.2-11, showed significant variations

in recorded radial and axial temperatures. A reassessment of the irradiation simulator uniformity calibration procedure indicates the following:

1. The procedure did not accurately simulate the view factor of the recessed mirror mounting position in the support stand.
2. The wide angle view factor of the flux transducer translates to a full aperture averaging device at the calibration frame position.
3. The horizontally-mounted irradiation simulator lamp assemblies produced horizontal zonal bands of higher intensity irradiation locally on the mirror surface.

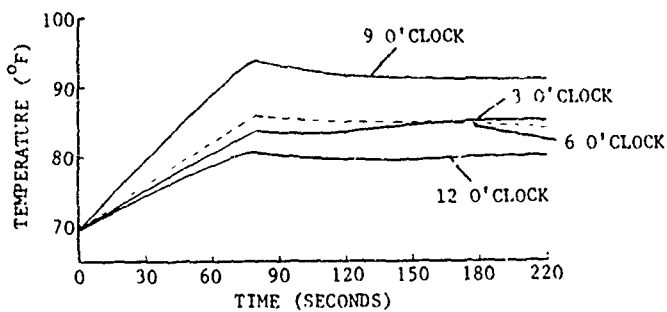


0.5-METER MIRROR IRRADIATION TEST

Figure 2.3.2-7

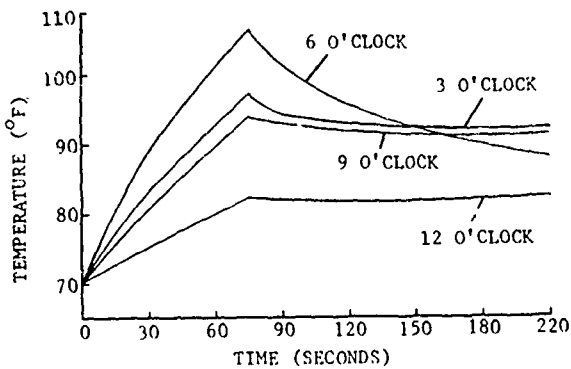
Consequently, it has been concluded that:

1. The test mirror was subjected to similar irradiation flux levels for each test.
2. The change in thermal data values for the center and 6 o'clock positions was caused by a gravity-induced downward repositioning of one or more irradiation lamp assemblies in the interval between tests.

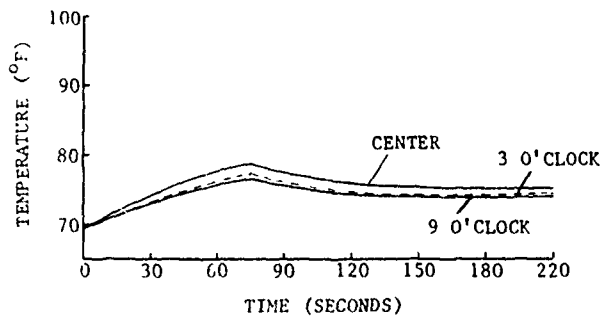


(a) RADIAL AT FRONT PLATE, FIRST ORIENTATION

← Figure 2.3.2-8

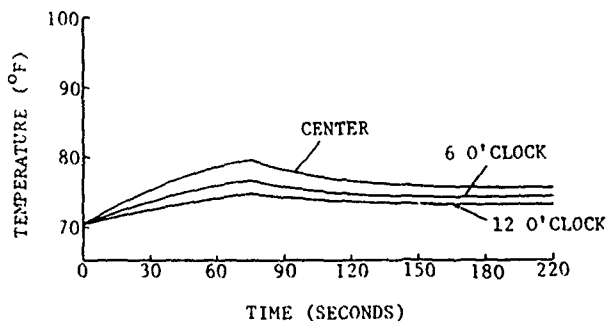


(b) RADIAL AT FRONT PLATE, SECOND ORIENTATION

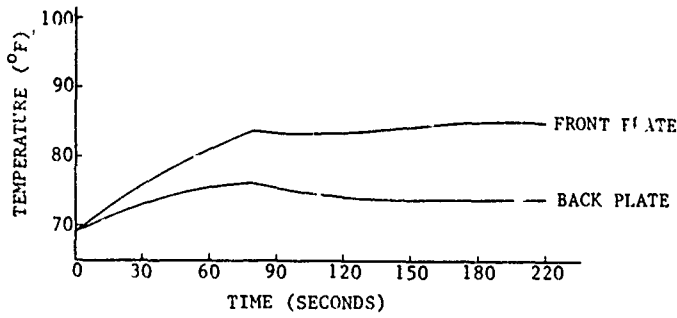


(a) RADIAL AT BACK PLATE, FIRST ORIENTATION

Figure 2.3.2-9 →

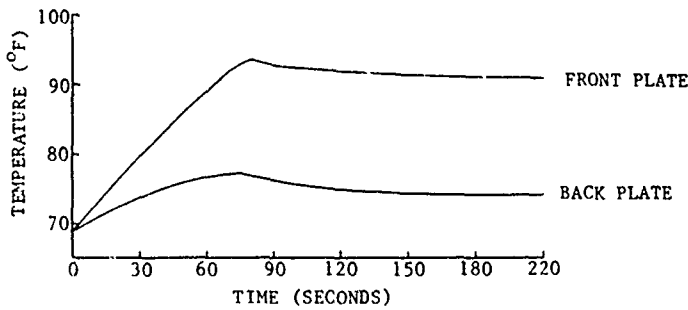


(b) RADIAL AT BACK PLATE, SECOND ORIENTATION

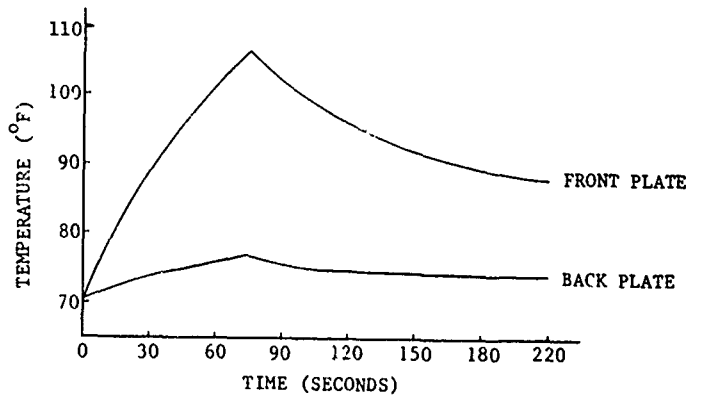


(a) AXIAL ΔT FRONT & BACK PLATE, FIRST ORIENTATION POSITION 3

← Figure 2.3.2-10

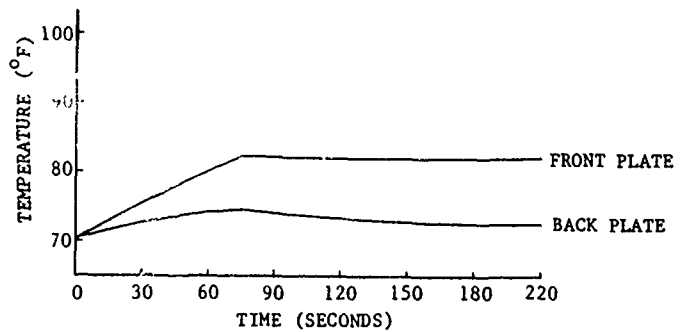


(b) AXIAL ΔT FRONT & BACK PLATE, FIRST ORIENTATION POSITION 9



(a) AXIAL ΔT FRONT & BACK PLATE, SECOND ORIENTATION POSITION 6

Figure 2.3.2-11 →



(b) AXIAL ΔT FRONT & BACK PLATE, SECOND ORIENTATION POSITION 12

Tables 2.3.2-2 and 2.3.2-3 show radial and axial thermal deltas, respectively, for both the first and second test orientations.

2.3.2.4 Test Equipment Description -

Dynamic Resolution Test (DRT) Chamber - The DRT is a large, cylindrical, walk-in vacuum chamber which is equipped with a full-diameter access

Table 2.3.2-2

*IRRADIATION RESPONSE TEST THERMAL DATA
RADIAL TEMPERATURE, 80-SECOND IRRADIATION*

THERMOCOUPLE POSITION	FRONT PLATE TEMPERATURE (°F)		BACK PLATE TEMPERATURE (°F)	
	FIRST ORIENTATION	SECOND ORIENTATION	FIRST ORIENTATION	SECOND ORIENTATION
CENTER			79	80
3 O'CLOCK	84	97	77	
6 O'CLOCK	86	106		77
9 O'CLOCK	94	94	71	
12 O'CLOCK	81	82		74
MAXIMUM GRADIENT	13	24	8	6
AVERAGE TEMPERATURE	89	95	76	77
AMBIENT TEMPERATURE	69		70	

Table 2.3.2-3

*IRRADIATION RESPONSE TEST
THERMAL DATA
AXIAL TEMPERATURES
80-SECOND IRRADIATION*

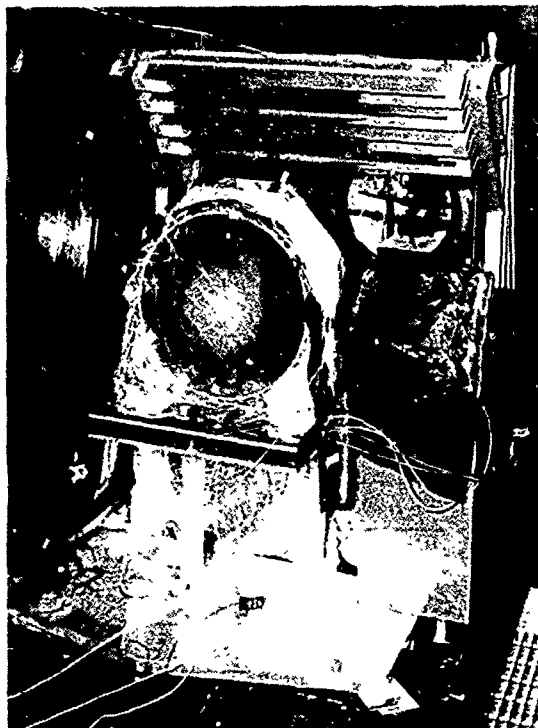
	TEMPERATURE (°F)	
	FIRST ORIENTATION 3 O'CLOCK	SECOND ORIENTATION 6 O'CLOCK
FRONT PLATE	84	106
BACK PLATE	76	77
ΔT	8	29
	FIRST ORIENTATION 9 O'CLOCK	SECOND ORIENTATION 12 O'CLOCK
FRONT PLATE	94	82
BACK PLATE	77	75
ΔT	17	7

door, electrical power, instrumentation, and liquid pass-through port capability. A 19-inch diameter by 1.25-inch thick optical window is mounted to the rear wall for interferometric evaluations. A substantial interferometer mounting block is located exterior to the chamber window position. The chamber and mounting block are attached to a common vibration-isolated platform. Each irradiation response test was conducted at a pressure level of 15 ± 10 microns.

Interferometer and Recording Cameras - An itek Laser Unequal Path Interferometer (LUPI) was positioned outside the chamber optical window at the center of curvature of the 0.5-meter mirror (see Figure 2.3.2-3). The LUPI, which was aligned normal to the window, used a 1.5-inch diameter central aperture window area. The test beam leaving the interferometer was collimated with the primary fiducial image plane inside the interferometer approximately 2 inches in back of the $f/2.8$ diverger lens. The existing beam was split into two equal-intensity beams, then folded into two motorized recording cameras. The fiducial image planes were reimaged onto the two film planes using relay lenses to each camera. Data was recorded by imaging the 0.5-meter mirror aperture interferograms simultaneously on a 35mm Single Lens Reflex camera, operating at 3 frames per second, and a 16mm CINE camera, operating at 190 frames per second. Interferometric data was recorded in this manner to allow for figure reduction at discrete intervals (35mm SLR) and to allow a particular fringe to be followed throughout the 80-second test interval. Following a particular fringe enables the axial displacement of the mirror surface to be measured. Knowing the axial movement and the total fringe focus change provides a basis to calculate test mirror radius change.

Quartz Lamp Irradiation Simulator - The irradiation simulator, shown in Figure 2.3.2-12, consists of eight elliptical, infrared, in-line, heater assemblies mounted to a support structure. Each assembly contains a 36-inch long, tungsten filament, argon quartz lamp with a maximum power rating of 3.8 kilowatts at 560 volts. The spectral radiance of the lamps for the test series was calculated; the resulting radiance, as a function of wavelength, is shown in Figure 2.3.2-13. Also shown in this figure is the average coating absorption values for two witness samples, which were coated at the same time as the 0.5-meter mirror.

The spectral radiance was calculated from 0.4 to 4.0 microns and is adjusted to account for coating absorption and quartz transmission. The irradiance peaks at approximately 3.1 microns and falls to about 0 at 4.2 microns because of the low transmission value of quartz beyond 4.2 microns.

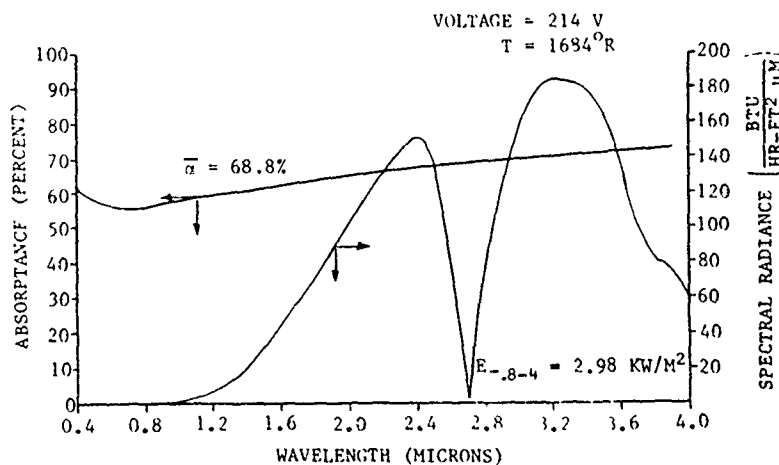


IRRADIATION SIMULATOR
(Photo of Figure 2.3.2-14)
Figure 2.3.2-12

Each coordinate position was spaced at 5-inch intervals from the operational axis of the simulator assembly. A Medtherm, Type 64-05-20T flux transducer, with a range of 0.5 Btu/ft²-sec (0 to 56.8 kw/m²) and a signal output of 0 to 10 mv, was employed for the uniformity adjustments. A pre-test uniformity survey,

The irradiance of 3.40 kw/m² over the 0.4 to 4.0 micron bandwidth becomes 4.94 kw/m² incident when divided by the coating absorption of 0.688. This value compares favorably with the average adjusted mirror flux value of 4.44 kw/m² monitored at the transducer position during tests 1 and 2.

Irradiation Calibration Frame - The calibration frame was assembled to allow accurate horizontal and vertical coordinate positioning of a heat flux transducer. This provides a means to monitor the average flux density at each reference point for calibrating the irradiation uniformity of the simulator lamp assemblies.



ABSORPTANCE AND SPECTRAL RADIANCE VERSUS WAVELENGTH
0.5-METER MIRROR COATING IRRADIATED BY
TUNGSTEN FILAMENT-ARGON QUARTZ LAMPS

Figure 2.3.2-13

shown in Table 2.3.2-4, established an average flux level of 0.287 mv, transducer output = 2.77 kw/m². A post-test survey indicated the average flux level to be 0.298 mv, transducer output = 2.86 kw/m². Multiplying the ambient pressure values by a 1.7 air-to-vacuum shift factor results in values of 4.71 and 4.86 kw/m², respectively. The variations in survey results can be attributed to mirror alignment errors in repositioning the calibration frame after the second test.

MIRROR PLANE
HEAT FLUX TRANSDUCER SURVEY POSITION
COORDINATES RELATIVE TO 0.5 M MIRROR POSITION

TRANSDUCER POSITION	PRE-TEST SURVEY TRANSDUCER OUTPUT MV	POST-TEST SURVEY TRANSDUCER OUTPUT MV
1	.285	.289
2	.269	.283
3	.291	.306
4	.292	.311
5	.289	.314
6	.271	.288
7	.256	.266
8	.282	.294
9	.292	.307
10	.288	.301
11	.261	.276
12	.293	.291
13	.306	.309
14	.321	.317
15	.306	.308
16	.289	.292
17	.289	.305
*18	.226	.232
FLUX UNIFORMITY	.287 ^{+11.9%} -10.8%	.298 ^{+6.6%} -10.6%
POSITIONS 1-17	(2.77 KW/M ² ^{+11.9%} -10.8%)	(2.86 KW/M ² ^{+6.6%} -10.6%)

**Low pressure transducer reference position*

Table 2.3.2-4

IRRADIATION HEAT
FLUX UNIFORMITY SURVEY

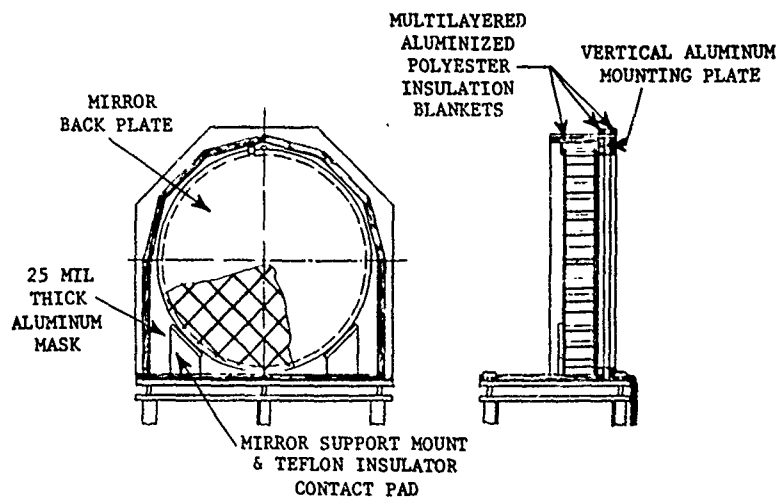
Thermal Data Acquisition System - A ten-channel Fluke 2200B Datalogger recorder was used to monitor the test mirror thermal data points for each test. A ten-channel scan rate of five seconds was used for the first 180 seconds of the test period, with a reduction to one minute intervals for the remainder of the test period. Copper/Constantan Type "T" thermocouples were securely attached to each data point surface, with compliant Fiberglass-backed, pressure-sensitive tape. Each thermocouple was characterized at two temperature levels, 73.7⁰F (ambient) and 212⁰F. Thermocouple accuracy values for each temperature level were 73.71±0.04⁰F and 211.17±0.22⁰F average correction.

Mirror Support Stand Assembly - The support stand assembly (Figure 2.3.2-13 and Table 2.3.2-5) was basically comprised of two structural components: a three-legged pedestal mount and an alignment adjustable mirror support stand. The pedestal was hard mounted to a substantial aluminum baseplate to maintain position integrity. The support stand consisted of an aluminum baseplate and a vertical mechanical plate insulated on each major surface with a 0.5-inch thick, 50-layer, aluminized

Table 2.3.2-5 IRRADIATION RESPONSE TEST THERMOCOUPLE CALIBRATION				
DATA ACQUISITION SYSTEM-FLUKE 2200B DATA LOGGER THERMOCOUPLES-TYPE "T", COPPER/CONSTANTAN				
DATA REPRESENTS FIVE SAMPLE AVERAGE FOR TWO CALIBRATION TEMPERATURE LEVELS 73.71 ⁰ F AND 212 ⁰ F				
THERMOCOUPLE NUMBER	73.71 ⁰ F		212 ⁰ F	
	TEMPERATURE VALUE	CORRECTION FACTOR	TEMPERATURE VALUE	CORRECTION FACTOR
1	73.68	+0.03	210.94	+0.23
2	73.60	+0.11	210.96	+0.21
3	73.70	+0.01	211.26	-0.09
4	73.68	+0.03	211.04	+0.13
5	73.70	+0.01	211.28	-0.11
6	73.70	+0.01	211.38	-0.21
7	73.70	+0.01	211.34	-0.17
8	73.70	+0.01	211.08	+0.09
9	73.80	+0.09	211.18	-0.01
10	73.80	+0.09	211.28	-0.11
MEAN	73.71	+0.04 AVERAGE CORRECTION	211.17	+0.22 AVERAGE CORRECTION
CORRECTIONS ARE TO MEAN VALUE				

polyester blanket. A 25-millimeter thick aluminum mask was interfaced between the inner insulation blanket and the front plate surface of the test mirror.

All vertical assembly components were configured with a 19-inch diameter opening, as shown by Figure 2.3.2-13. Two mirror support mounts provided 90-degree, V-block contact support for the test mirror. Each mount was thermally isolated from the baseplate with 0.25-inch thick Teflon insulators.

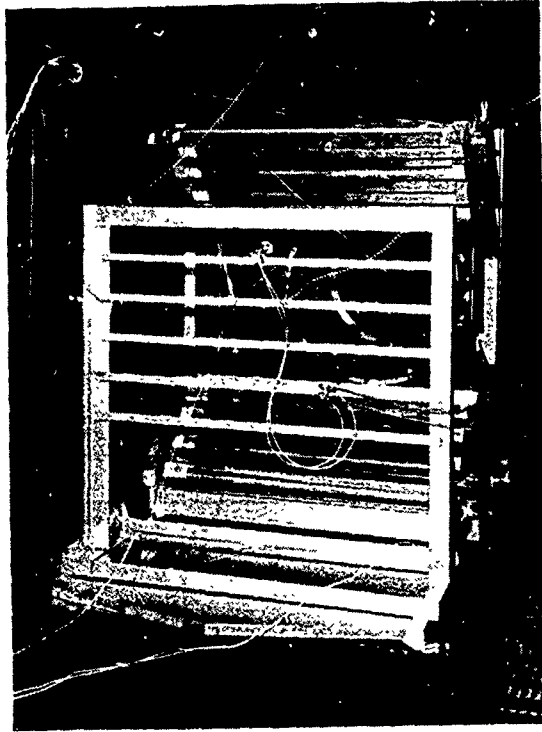


0.5-METER TEST STAND
(Photo shown in Figure 2.3.2-12)

Figure 2.3.2-14

The mirror contact surfaces of each mount were also fabricated from 0.5-inch thick Teflon. Each mirror mount surface, viewing the bottom edge segment of the mirror, was also insulated with aluminized polyester material. Additional blankets were used to isolate the mirror edge from the baseplate and peripheral random reflected energy.

Thermocouple 10 was positioned on the mirror side of the vertical mechanical plate, 0.5-inch inboard of the aperture edge at the 3 o'clock position. In the test, monitoring of thermocouple 10 indicated a 0.5°F increase in mechanical plate temperature for each test period. The thermal insulation rating for the blanket material was $0.021 \text{ Btu/hr./ft}^2\text{-}^{\circ}\text{F}$ at a pressure of 10 microns. Consequently, the thermal transfer to the 0.5 peripherally masked edge of the mirror would be insignificant. Figure 2.3.2-14 shows the back of the mirror, mounted in the test support stand with the multilayer insulation in place. Also shown is the top of the irradiation lamp stand assembly, the chamber viewport, and the test interferometer.



0.5-METER MIKROKOR IRRADIATION
RESPONSE TEST CONFIGURATION
(Photo of Figure 2.3.2-3)

Figure 2.3.2-15

The point is that in spite of the large measured rotational and axial gradients (Figures 2.3.2-2 and 2.3.2-3), there was little optical surface degradation, nor was there evidence of thermoelastic surface quilting due to the small coefficient of expansion (CTE) mismatch between the ULETM and frit (see Table 2.3.3-2).

The ultra lightweight, ULETM frit mirror was also tested on-back, on an air bag, to verify that there was no optical instability induced by either the

2.3.3 0.5-Meter Mirror Heat Load Test

The optical data acquisition during the 80-second irradiation interval was accomplished with a 16mm CINE and a motorized 35mm camera, as previously described. The configuration was an on-edge, two-orientation, vacuum irradiation test conducted at Itek Corporation. Table 2.3.3-1 summarizes the optical data summary for the two-orientation test.

It is important to note that the actual rms of the surface changed very little in magnitude (indicating an excellent optical surface even after irradiation) but the 0.026 wave rms delta reflects the nonuniformity in the irradiation energy.

Table 2.3.3-1
OPTICAL DATA SUMMARY

	RMS*	P-V*
FIRST ORIENTATION AVERAGE	0.047 λ	0.31 λ
SECOND ORIENTATION AVERAGE	0.048 λ	0.36 λ
DELTA--FIRST MINUS SECOND	0.026 λ	0.26 λ

* This is surface quality at 6328 \AA over a 19" clear aperture.

<i>Table 2.3.3-2</i> <i>DPEA EVALUATION</i>		
	RMS*	P-V*
START AVERAGE	0.006	0.021
80-SECOND AVERAGE	0.002	0.007
DELTA START - 80 SECOND	0.005	0.015
* Surface at 6328 Å		

chrome coating application or the surface irradiation. There was no measurable optical change in the 20-inch diameter, ULE™ frit mirror as a result of either the coating or irradiation exposure (see Table 2.3.3-3).

The point-for-point delta maps, as shown, are within the test error established and reported earlier for the on-back test setup.

2.3.4 Heat Load Test Data Correlation and Scaling

Results of the analyses and tests have been presented in previous sections. Thermocouples measure surface temperatures, which can be compared directly to the predicted temperatures, but mirror deformation, measured during the test, is given in terms of Zernike aberrations and the finite element model calculates surface deflections. Since these cannot be directly compared, the finite element results are processed in order to express the surface deflections in terms of Zernike aberrations.

<i>Table 2.3.3-3</i> <i>4-ORIENTATION AIR BAG TEST AT KODAK</i>		
	RMS*	P-V*
PRE-CHROME COAT	0.023	0.214
CHROME COAT (PRE-IRRADIATION)	0.023	0.251
CHROME COAT (POST-IRRADIATION)	0.023	0.257
CHROME COAT STRIPPED	0.021	0.192
DELTA (PRE-, POST-COAT)	0.008	0.085
DELTA (PRE-, POST-IRRADIATION)	0.005	0.048
DELTA (PRE-COAT TO POST-IRRADIATION & CHROME STRIP)	0.005	0.048
* This is surface data at 6328 Å for a 19" clear aperture.		

The gravity-induced deformation of the mirror was calculated in order to check the validity of the finite element model. Any uncertainty in the heat transfer aspects of the analysis is thus eliminated, and only the accuracy of the deflection model is tested. Analysis and test results are shown in Tables 2.3.4-1 and 2.3.4-2, respectively, for the one-g. When analyzing the test results, it should be noted that focus and coma errors are not only caused

Table 2.3.4-1

ZERNIKE ABERRATION ANALYSIS, ANALYTICAL RESULTS FOR A ONE-G LOAD CASE AND A V-BLOCK SUPPORT

ABERRATION	FUNCTIONAL P-V (WAVES AT 6328 Å)	RESIDUAL RMS (WAVES AT 6328 Å)
INPUT ARRAY*	-0.001	0.0013
PRIMARY SPHERICAL	0.0012	0.0013
PRIMARY COMA	0.0039	0.0013
PRIMARY ASTIGMATISM	0.0039	0.0010
PRIMARY TREFOIL	0.0034	0.008
PRIMARY TETRAFOIL	0.0018	0.007

**Tilt, bias, and defocus have been removed.*

by distortion of the optical surface, but can also be caused by setup errors; thus, comparison should be made between individual aberrations or between the residual rms after power has been removed.

Test results show that the input array is 0.013 wave as compared to the analytical prediction of 0.0013 wave.

Both test and analysis

essentially agree that there is very little error produced by the on-edge configuration, and both test and analysis show that the major aberrations are primary astigmatism and primary trefoil. The finite element model is, therefore, representative of the actual mirror.

2.3.4.1 Temperature

Correlation - Thermocouple output for the two tests are shown in Figures 2.3.2-5 and 2.3.2-6. Thermocouple number 1, which is located in the center of the mirror, measured significantly higher temperatures in the first orientation test than in the second test. Since the output from this thermocouple will be used to determine mirror surface temperature; it is important to determine which of these two outputs is correct.

Table 2.3.4-2

ZERNIKE ABERRATION ANALYSIS, TEST RESULTS FOR A ONE-G LOAD CASE AND A V-BLOCK SUPPORT

ABERRATION	FUNCTIONAL P-V (WAVES AT 6328 Å)	RESIDUAL RMS (WAVES AT 6328 Å)
INPUT ARRAY*	-	0.013
PRIMARY ASTIGMATISM	0.03	0.012
PRIMARY COMA	0.01	0.011
PRIMARY TREFOIL	0.02	0.011
PRIMARY SPHERICAL	0.00	0.011
PRIMARY TETRAFOIL	0.01	0.011

**Tilt, bias, and defocus have been removed.*

During pre-test checkout, the mirror was irradiated several times, and output from thermocouple number 1 was monitored. A graph of the temperature measured during the pre-test checkouts and the temperatures measured during the first and second orientation tests is shown in Figure 2.3.2-7. It is apparent from this figure that temperatures measured during the first orientation test were correct. Since the flux transducer indicated that the same heat load was applied to the mirror for both tests, it is postulated that one of the elliptical reflectors rotated between the two tests, producing a different load profile in the second test. If this particular reflector concentrated most of the lamp output at the center of the mirror, a rotation would redirect the heat away from this area; this would result in the lower temperatures recorded by thermocouple number 1 in the second test. If this occurred, it is also reasonable to expect differences to be recorded by the thermocouple around the edge of the mirror. Since a rotation of the reflector would result in more heat being directed to the 6 o'clock mirror position, it is expected that this area would be hotter in the second test. Examination of the output from thermocouples located at this position verifies this hypothesis; thus, a rotation of an elliptical reflector is a feasible explanation of the temperature differences measured in the two tests.

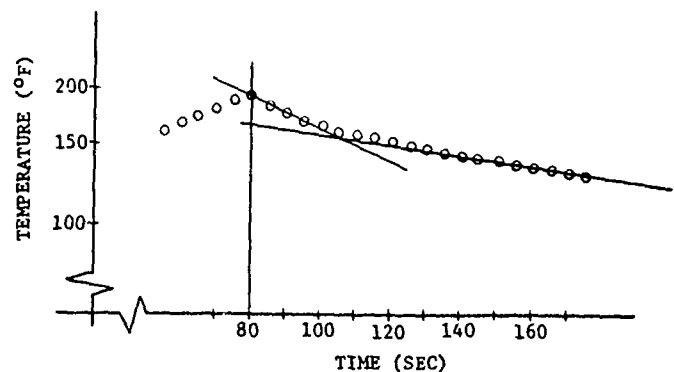
Examination of the temperatures of points on the mirror edge show that this area of the mirror is significantly lower in temperature than the center of the mirror. Both the finite element model, as well as simple closed form analysis, indicate that temperatures recorded by the thermocouples are realistic.

Both the NASTRAN thermal model and the SATAN single cell thermal model predict that the point of the vertex of the optical surface will have a 95°F temperature rise at the end of 80 seconds, and that the back plate will remain at a constant temperature. The NASTRAN results indicate that the points over the core are significantly lower in temperature than the point in the cell center. Although it is true that there will be a difference in temperature between these two points, it is felt that there is a problem in that the NASTRAN model

overstates this temperature differential. The SATAN single cell model shows that points over the core are indeed lower in temperature than a point in the cell center, but not to the degree indicated in the NASTRAN model.

During the test, the temperature recorded by thermocouple number 1 is caused by an increase in glass temperature as well as self-heating of the thermocouple itself. After the heat load is removed, the thermocouple will record two different cool-down rates. At first the temperature will drop off at a relatively fast rate, which is due to the thermocouple dissipating directly absorbed heat, then the temperatures will drop at a slower rate as the glass continues to cool. In order to estimate the mirror temperature at the end of 80 seconds, a plot of temperature versus time was made on semi-log paper; the two characteristic cool-down rates are shown in Figure 2.3.4-1.

Extrapolating back from the glass cool-down portion of this curve, the peak glass temperature is estimated to be 165°F, or a 95°F temperature increase, which is in excellent agreement with analysis. Examination of the thermocouples on the back plate, however, shows that this plate is heated to 76°F, which does not agree with analysis. Analysis and test results are summarized in Table 2.3.4-3.



THERMOCOUPLE NUMBER 1 COOLDOWN

Figure 2.3.4-1

POSITION	ANALYSIS	TEST
FRONT PLATE	95°F	95°F
BACK PLATE	0°F	6°F
GRADIENT	95°F	88°F

To explain this discrepancy between the predicted and measured back plate temperature increase, it is assumed that during the test some heat transmitted through the faceplate and was subsequently absorbed by the coating on the back surface of the back plate. The effect is to reduce the front-to-back temperature gradients in the mirror.

In order to validate this assumption, it is necessary to measure both the reflectivity and the transmittance of the chrome coating.

2.3.4.2 Deflection Correlation - Results of the NASTRAN analysis indicate that 99 percent of the surface deformation produced by the test load is defocus. Assuming an average coefficient of thermal expansion of $40 \times 10^{-9}/^{\circ}\text{C}$, the NASTRAN model predicts a peak-to-valley focus error of 1.097 wave (λ) ($\lambda = 0.6328 \mu\text{m}$). The coefficient of thermal expansion is a measured value for a standard ULE™ specimen that was heated to 950°C to simulate a frit firing. The finite element model does not account for any frit effects. To estimate this effect, the total amount of frit between the faceplate and core was calculated, and an effective frit thickness was determined by spreading the frit over the surface area of the mirror. It is estimated that there is 0.37 cubic inch of frit, which corresponds to an effective thickness of 0.00117 inch.

The SATAN model indicates that the temperature increase in the glass at the frit joint area is 77°F . Using these values, a thermal moment is calculated and used to determine how much the mirror deflects as a result of heating the frit material. The thermal moment and the resulting sag is calculated using the following expressions:

$$M_T = \frac{\alpha \Delta T t_f E d}{(1-\nu)}$$

$$\text{sag} = \frac{M_T D^2 (1-\nu)}{8 E I_{\text{eff}}}$$

where:

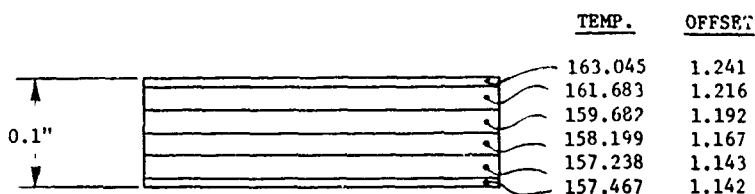
- α = average CTE ($^{\circ}\text{C}$)
- ΔT = temperature increase ($^{\circ}\text{C}$)
- t_f = effective frit thickness (in.)
- E = Young's modulus (psi)

- d = offset from neutral axis (in.)
 μ = Poisson's ratio
 D = clear aperture (in.)
 I_{eff} = effective bending inertia per unit width (in.³)

Substituting the appropriate values into these expressions results in a frit-induced sag of 0.083 wave, which reduces the predicted sag to 1.014 waves.

An approach similar to the method used to calculate frit-induced deformations can be used to predict deformations caused by uniformly irradiating the front surface of a mirror. This method provides both a check on the NASTRAN results and a method of scaling to different size mirrors. The SATAN single cell thermal model is used to calculate the temperature profile which is needed to calculate the thermal bending moment. This bending moment can then be substituted into the sag expression, and the results can be modified to account for both frit-induced deformations and the unheated edge.

As noted in Figure 2.3.1-2, the mirror faceplate thickness is divided into six layers. An average temperature for each layer and the distance from the center of the individual layer to the neutral axis



FACEPLATE TEMPERATURE PREDICTED
BY SATAN SINGLE CELL MODEL

Figure 2.3.4-2

are used to calculate the thermal moment. The additional moment produced by heating the core is not considered and, since the back plate remained at a constant temperature, there is no contribution from this part of the mirror. Figure 2.3.4-2 shows the average temperature and neutral axis offset of each layer in the faceplate.

The following expression is used to calculate the thermal bending moment that is used in the sag equation.

$$M_T = \frac{\alpha E}{(1-\nu)} \sum_{i=1}^6 t_i \Delta T_i d_i$$

where:

- t_i = thickness of the i th layer (in.)
- ΔT_i = temperature increase of the i th layer ($^{\circ}\text{C}$)
- d_i = neutral axis offset of the i th layer (in.)

Using the information provided in Figure 2.3.4-2 to calculate the thermal moment and substituting this value into the sag expression results in a peak-to-valley deflection of 1.257 waves.

In order to compare this to the finite element results, the effect of the unheated edge must be taken into account. The effect of the unheated edge is to reduce the expansion of the faceplate, thus reducing the thermal moment. To estimate this effect, consider the faceplate to be divided into two zones. The inner zone is heated to temperature, T_1 , and the outer zone is heated to temperature, T_2 . As the inner zone attempts to expand, a pressure is developed, the magnitude of which is given by the following expression.

$$p = \frac{E\alpha(\Delta T_1 - \Delta T_2)(b^2 - a^2)}{2b^2}$$

where:

- ΔT_1 = temperature rise of inside zone ($^{\circ}\text{C}$)
- ΔT_2 = temperature rise of outside zone ($^{\circ}\text{C}$)
- a = 9.5 inches
- b = 10 inches

The peak-to-valley deflection produced by this pressure is:

$$\text{sag} = \frac{pt_p dR^2}{2EI_{\text{eff}}}$$

Substituting into the above expression results in a 0.05 wave deflection. Adding this to the 0.033 wave sag produced by fric effects results in a total modification of 0.133 wave. This closed form approach therefore predicts a peak-to-valley deflection of 1.124 wave.

During the test, with the interferometer located at the center of curvature of the mirror, interferograms were taken with both a 35mm still camera and a 16mm movie camera running at 190 frames per second. In analyzing the interferograms, the Zernike polynomial designated "*defocus*" (or *sag*), is directly associated with the sag in the wavefront entering the interferometer; this sag in the wavefront is related to the distance between the interferometer and the center of curvature of the mirror. If the distance between the interferometer and the mirror vertex remains fixed, a change in the Zernike defocus term (before and after test) is directly related to the mirror deformation since the mirror center of curvature moves relative to the interferometer. A variation in the interferometer-to-mirror vertex distance also affects the defocus term, however, so that the mirror sag cannot be uniquely determined without knowledge of the change in interferometer-to-mirror vertex spacing.

The mirror vertex-to-interferometer motion can be determined by noting the fringe motion past a reference point on the mirror surface. As an example, whenever a full fringe moves past the mirror vertex, the mirror vertex-to-interferometer distance must have moved a distance wave/2. The direction can be found by physically moving the interferometer toward or away from the mirror, and noting the direction of fringe motion. Some reflection will show that mirror tilt and decenter are irrelevant to the above argument; they will only affect the number and shape of the fringes observed over this aperture.

This method requires continual tracking of fringe motion since one fringe cannot be differentiated from any other. In this test, the fringe motion was recorded with the 16mm movie camera.

The relation between the sag change in the wavefront produced by a motion of the interferometer located in the vicinity of focus is:

$$\delta \text{sag} = \delta l \sin^2 \frac{y}{R}$$

where:

δsag = sag change over the half aperture y

δl = change in mirror vertex to interferometer separation

y = half aperture of mirror

R = mirror radius of curvature

From the above argument:

$$\delta l = \frac{N\lambda}{2}$$

where:

N = number of fringes passing the mirror vertex

$$\delta \text{sag} = \frac{N\lambda}{2} \sin^2 \frac{y}{R}$$

or

$$= \frac{N}{2} \sin^2 \frac{y}{R}$$

where:

δsag is expressed in waves

In this test $y = 9.5$ inches, $R = 80$ inches

$$\delta \text{sag} = 0.0071 N$$

(The equivalent surface sag is one-half the above wavefront sag.)

The defocus term extracted from the interferogram, therefore, must be modified to determine mirror deformation. Mirror translation can either add to or subtract from the sag produced by mirror deformation. In this test the

shape of the fringes requires that the defocus produced by mirror translation is to be added to the total change in sag extracted from the interferogram.

Table 2.3.4-4 summarizes the results. Averaging the 16mm results from tests 1 and 2 results in a measured sag of 0.77 wave. The analysis and test results are summarized in Table 2.3.4-5.

The NASTRAN and closed form results correspond favorably, and there is reasonable agreement with the test results.

<i>Table 2.3.4-4</i>			
<i>TEST RESULTS</i>			
ORIENTATION	TOTAL DEFOCUS CHANGE (λ)	COMPUTED EQUIVALENT SAG FROM FRINGE MOTION (λ)	MIRROR SAG CHANGE (λ)
● 1st ORIENTATION			
60 SEC - 35mm	0.27	0.085	0.36
- 16mm	--	0.085	--
80 SEC - 35mm	--	0.186	--
- 16mm	0.52	0.186	0.71
● 2nd ORIENTATION			
60 SEC - 35mm	0.40	0.126	0.53
- 16mm	--	0.126	--
80 SEC - 35mm	0.57	0.181	0.75
- 16mm	0.64	0.181	0.82

<i>Table 2.3.4-5</i>	
<i>COMPARISON OF PREDICTED AND MEASURED PEAK-TO-VALLEY DEFLECTIONS</i>	
METHOD	PEAK-TO-VALLEY DEFLECTION ($\lambda = 6328\text{\AA}$)
NASTRAN	1.014 λ
CLOSED FORM	1.124 λ
TEST	0.770 λ

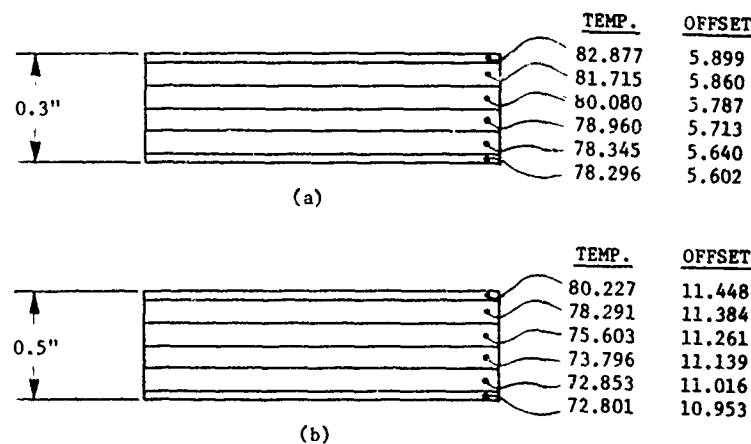
It was necessary to count fringes from the 16mm movie film and there was quite a bit of jitter in the movie. Although the error associated with the fringe count is hard to determine, this area is most likely to be the cause of the discrepancy between test and analysis. The close agreement between the NASTRAN analysis and the closed form analysis justifies using the closed form approach to scale the results to larger size mirrors.

2.3.4.3 Scaling - In the previous section, a technique was described which can be used to predict the peak-to-valley deflection of mirrors subjected to heat loads applied to the optical surface. This method will be used to predict the deformation of both 2.4-meter and 4.0-meter mirrors, in which

the optical surface absorbs a heat load of 0.0849 kilowatt per square meter for a duration of 100 seconds. The design of the 4-meter mirror was shown in Table 2.2.1-1; the 2.4-meter mirror design is given in Table 2.3.4-6.

For both mirrors, the temperature of the back plate remained constant; therefore, the thermal moment is produced by thermal expansion of the faceplate. Figure 2.3.4-3 summarizes the results of the SATAN thermal analysis. Effective inertia-per-unit width is calculated from the cross section of the mirror unit cell. For this cross section, the mirror plates form the flanges of an I-beam and the core strut forms the web. Since the 4-meter diameter mirror has a flat back, the bending inertia is a function of mirror radius; for this design,

Table 2.3.4-6 2.4-METER MONOLITHIC MIRROR DESIGN	
MEASUREMENT	DIMENSION (INCHES)
FACEPLATE THICKNESS	0.30
STRUT THICKNESS	0.08
CELL SPACING	3.50
MIRROR HEIGHT	11.80
OUTSIDE DIAMETER	94.50



FACEPLATE TEMPERATURES PREDICTED BY
SATAN THERMAL MODEL (a) 2.4-METER MIRROR
(b) 4.0-METER MIRROR

Figure 2.3.4-3

mirrors increases at a faster rate than the thermal bending moment. This suggests that the sag would be lower for the large mirrors; however, Table 2.3.4-7 shows that the sag for all three mirrors is comparable.

therefore, the effective inertia was calculated by taking the average inertia of ten different cross sections. The thermal bending moment, effective inertia, and peak-to-valley deflection for these mirrors are shown in Table 2.3.4-7.

It is noted that as mirror diameter increases, the effective inertia of the

The reason is that the peak-to-valley deflection is a function of the square of the mirror radius, which offsets the effects of inertia and thermal bending moment.

MIRROR DIAMETER (M)	EFFECTIVE INERTIA (IN. ³)	THERMAL BENDING MOMENT (LBS)	PEAK-TO-VALLEY DEFLECTION ($\lambda = 6328\mu$)
0.51	0.3484	5.086	1.257
2.54	22.5180	11.476	1.070
4.00	149.0000	23.107	0.937



Appendix A

Thermocouple Data

COMPARISON BY COUPLE NUMBER

1st and 2nd Orientation

IRRADIATION RESPONSE TESTS

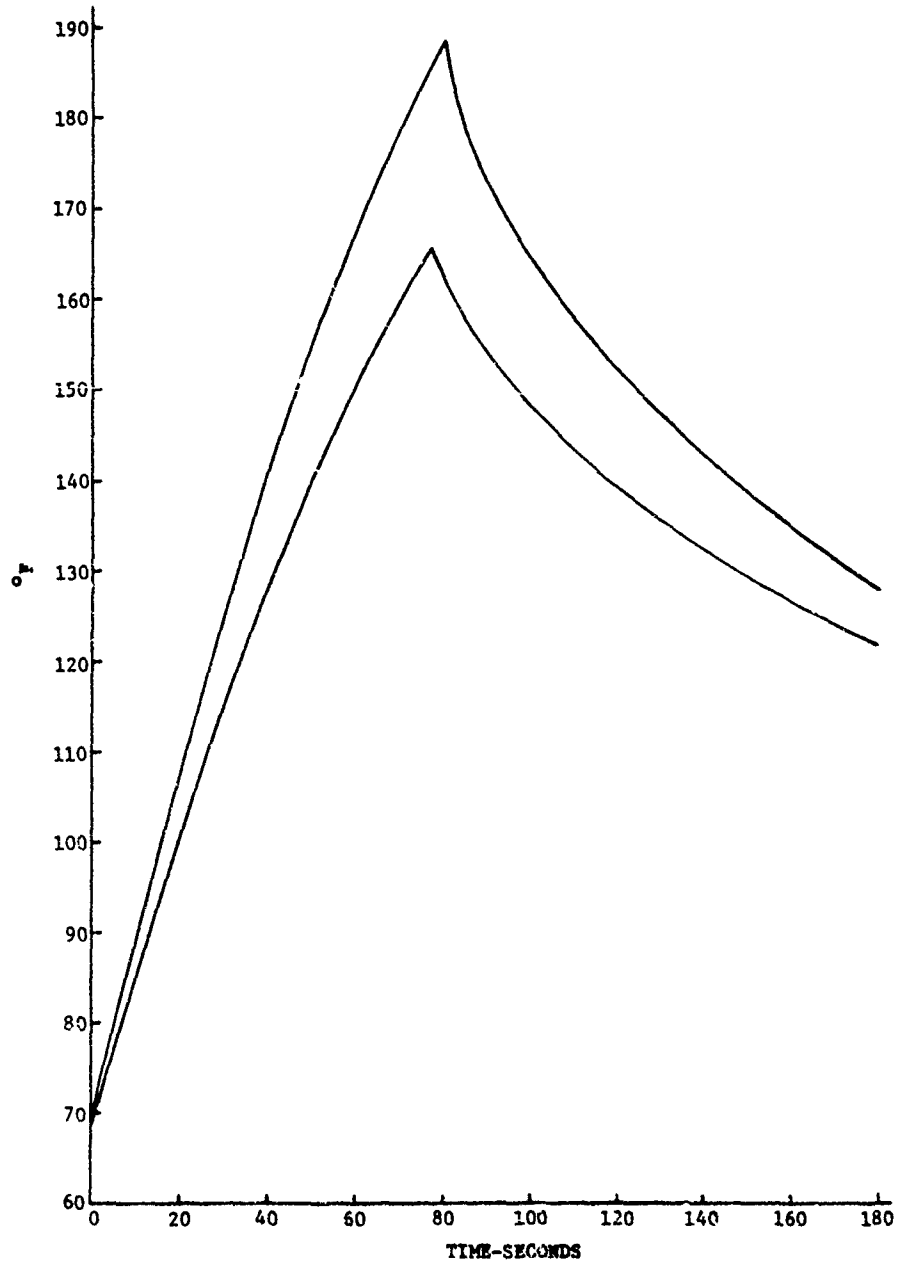


Figure A-1

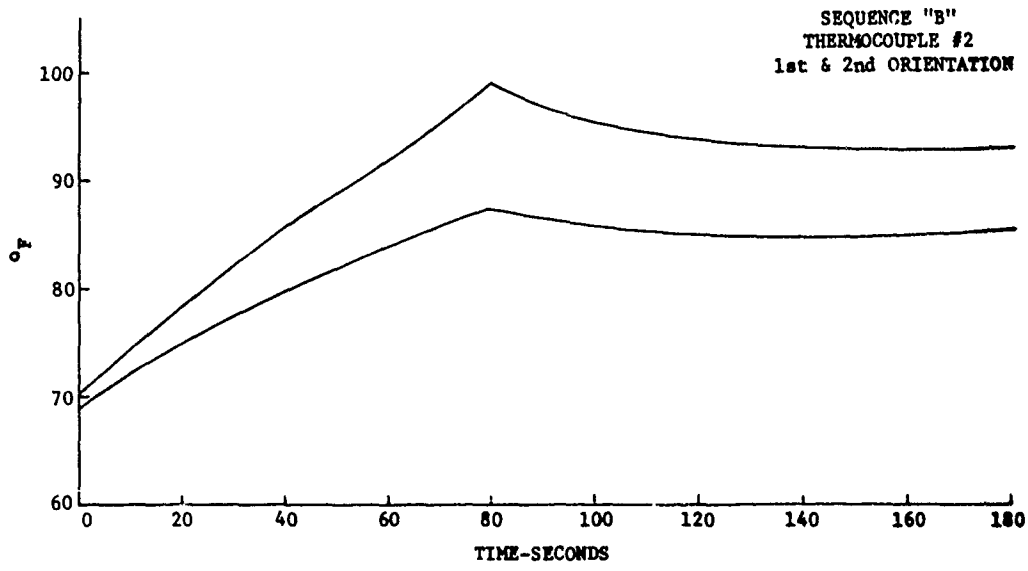


Figure A-2

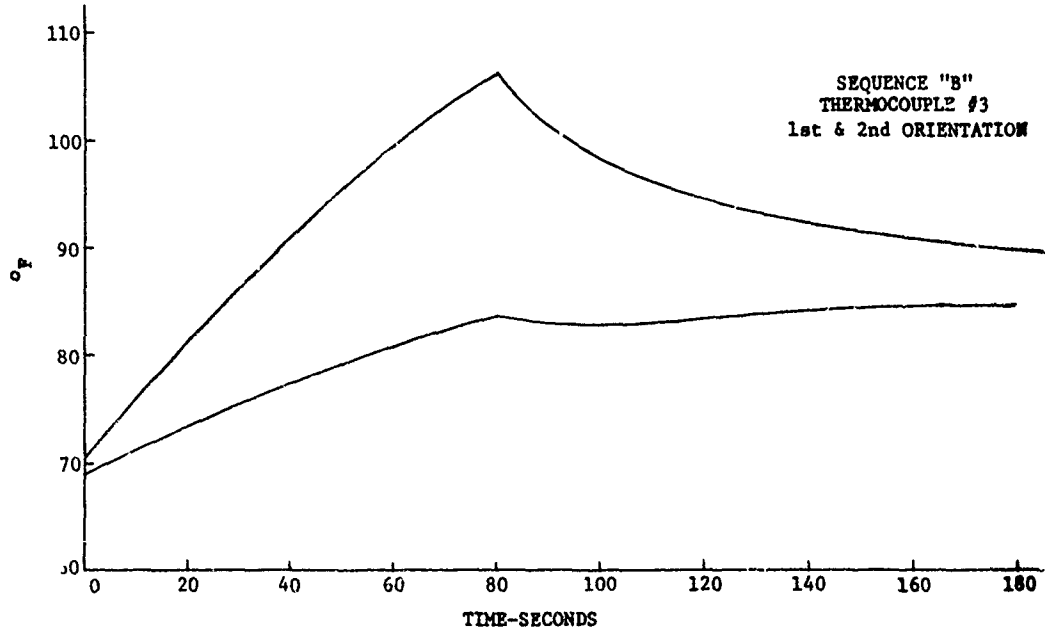


Figure A-3

RC-00348

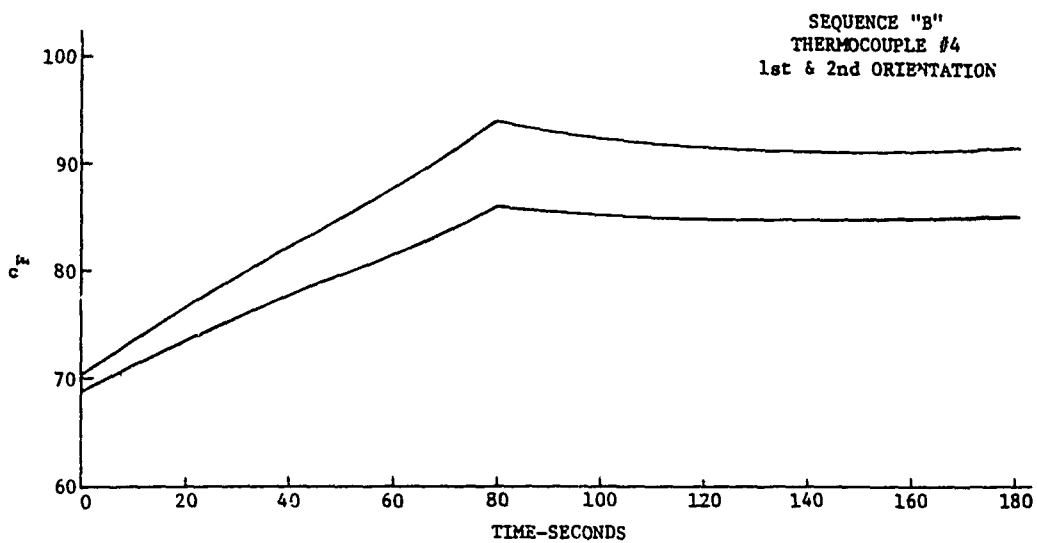


Figure A-4

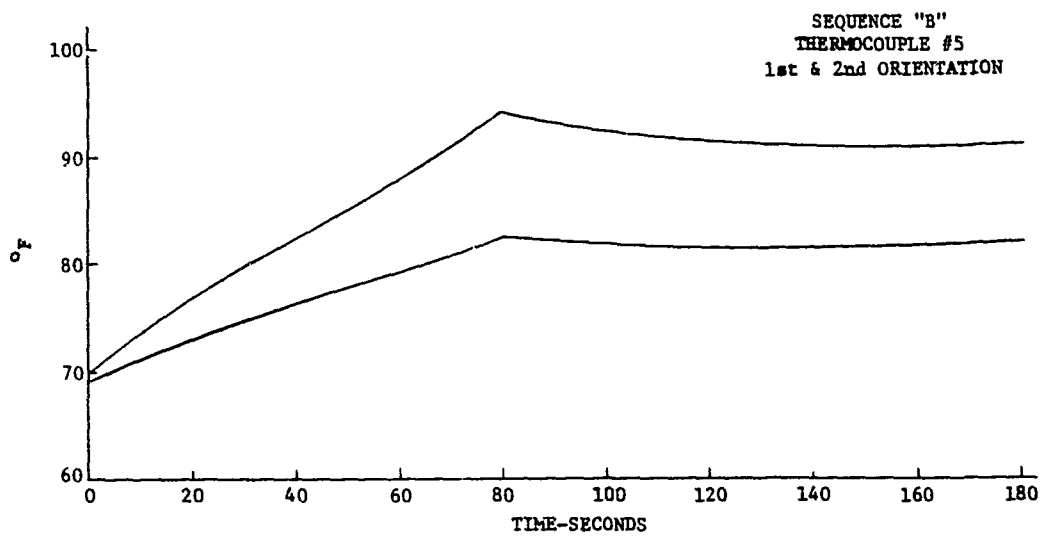


Figure A-5

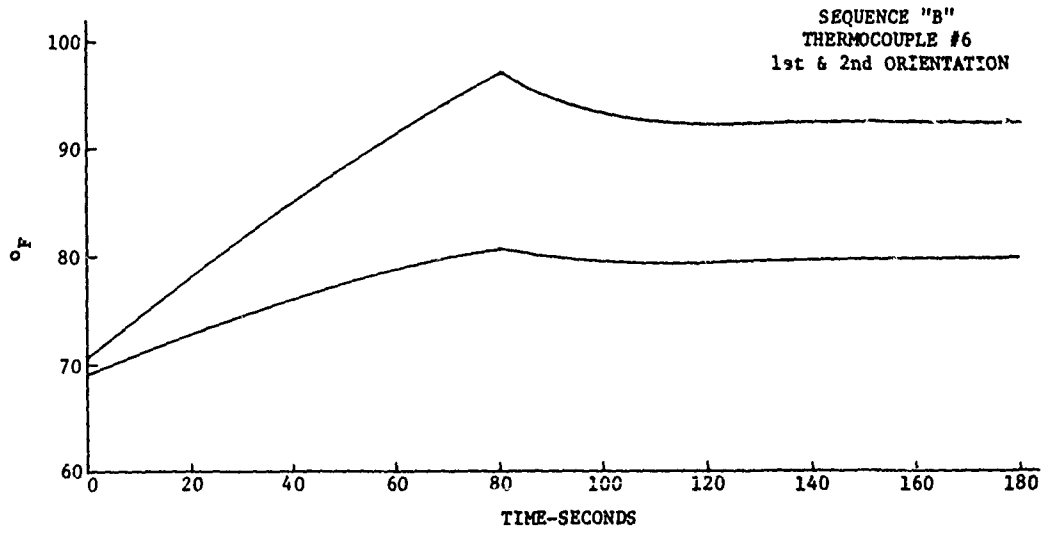


Figure A-6

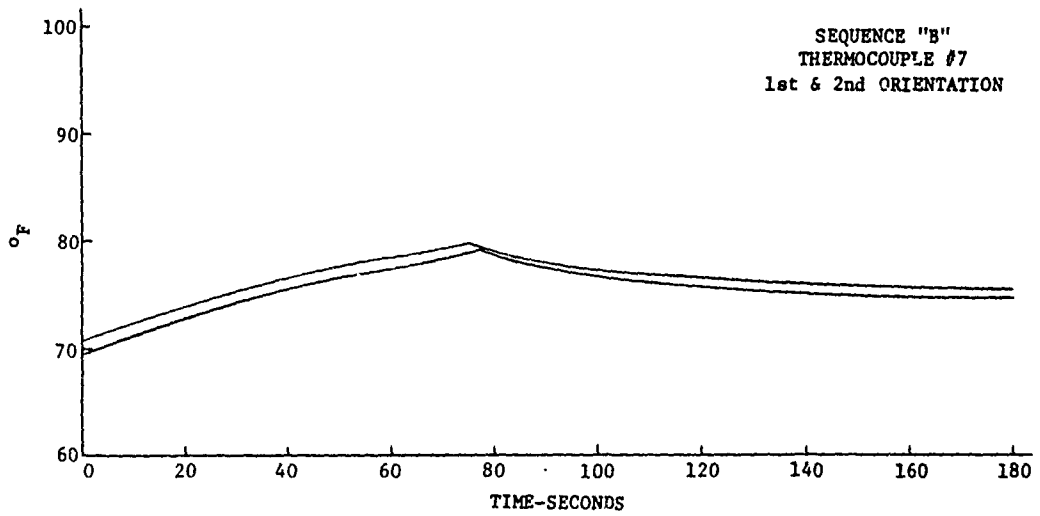


Figure A-7

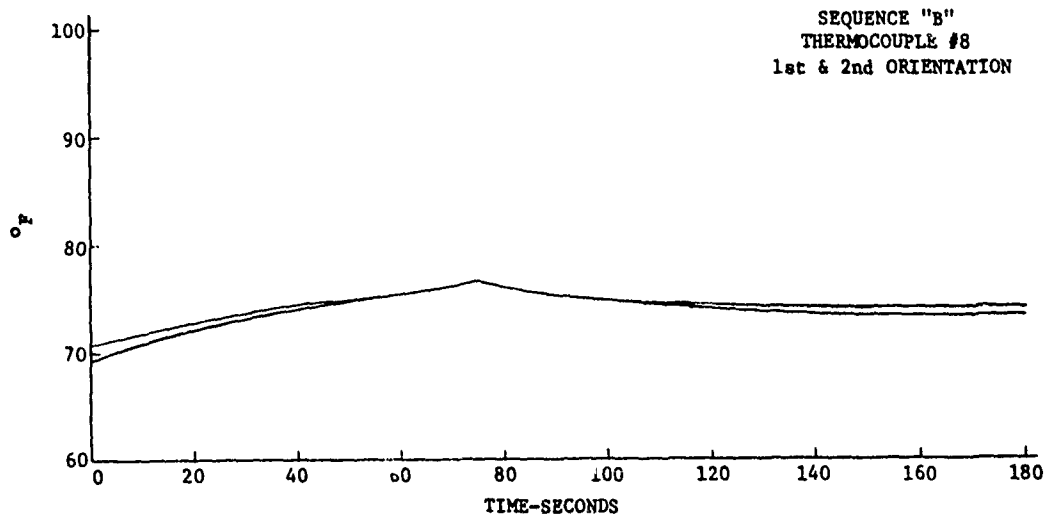


Figure A-8

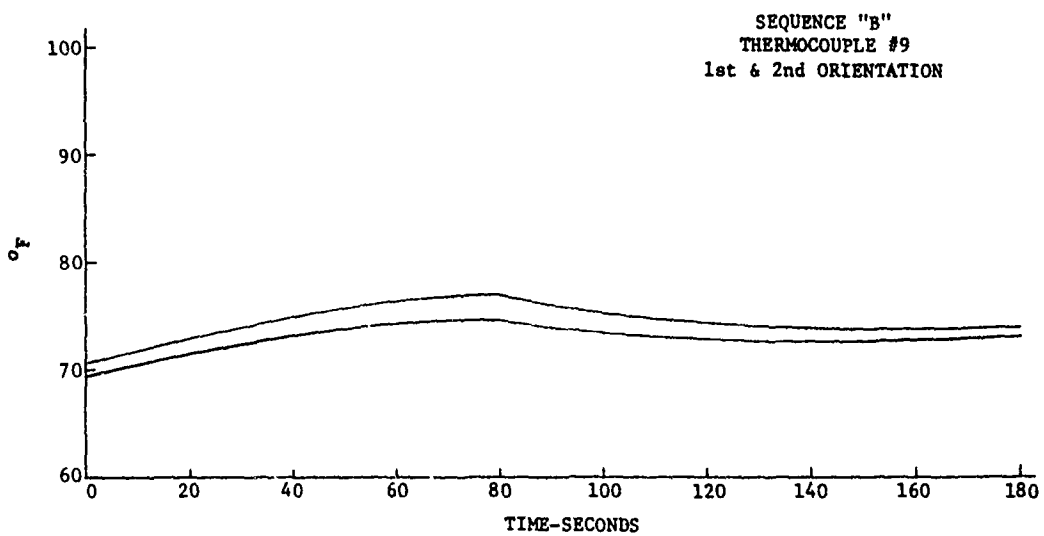


Figure A-9

RC-0034d

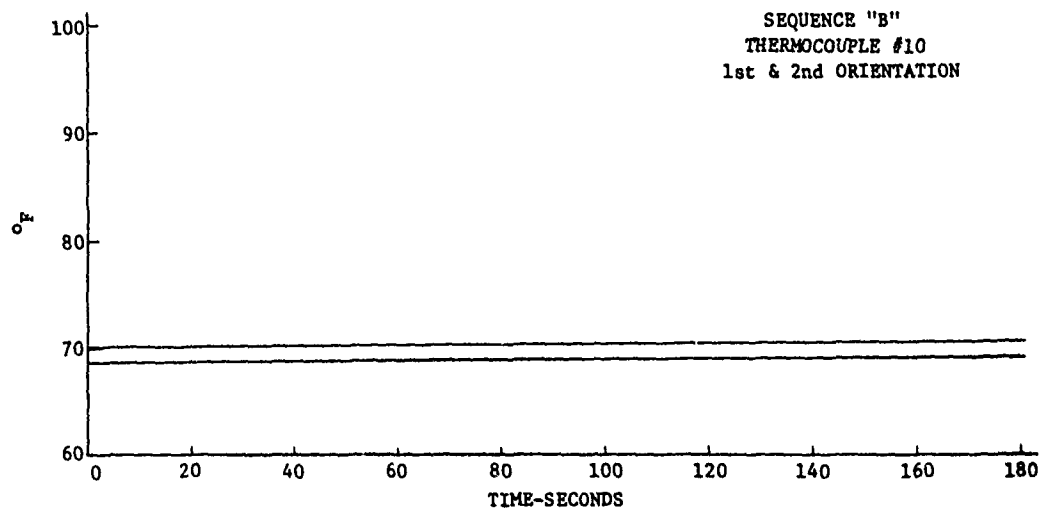


Figure A-10



Appendix B

Thermocouple Data

COMPOSITE AND INDIVIDUAL
1st Orientation

IRRADIATION RESPONSE TESTS

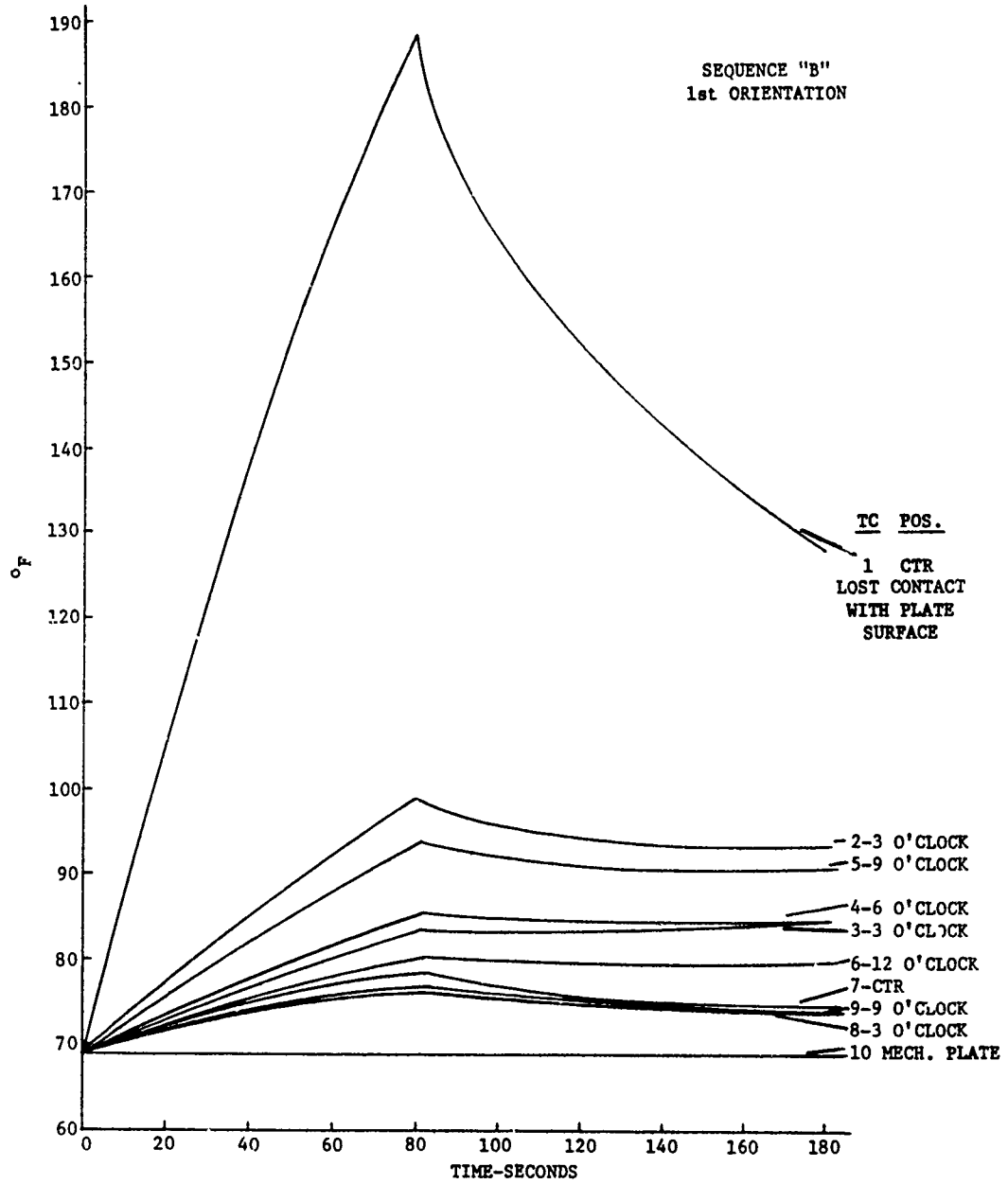


Figure B-1

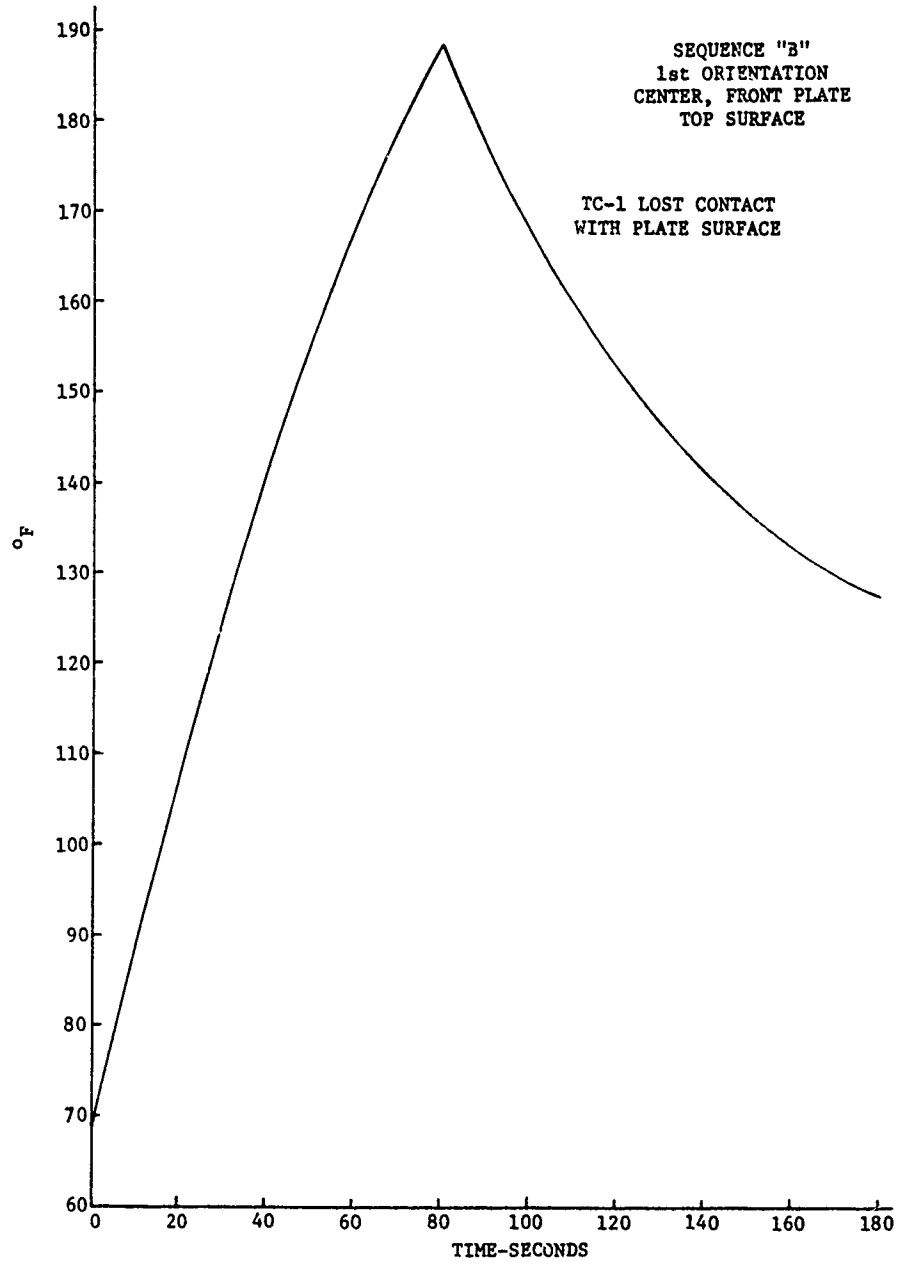


Figure B-2

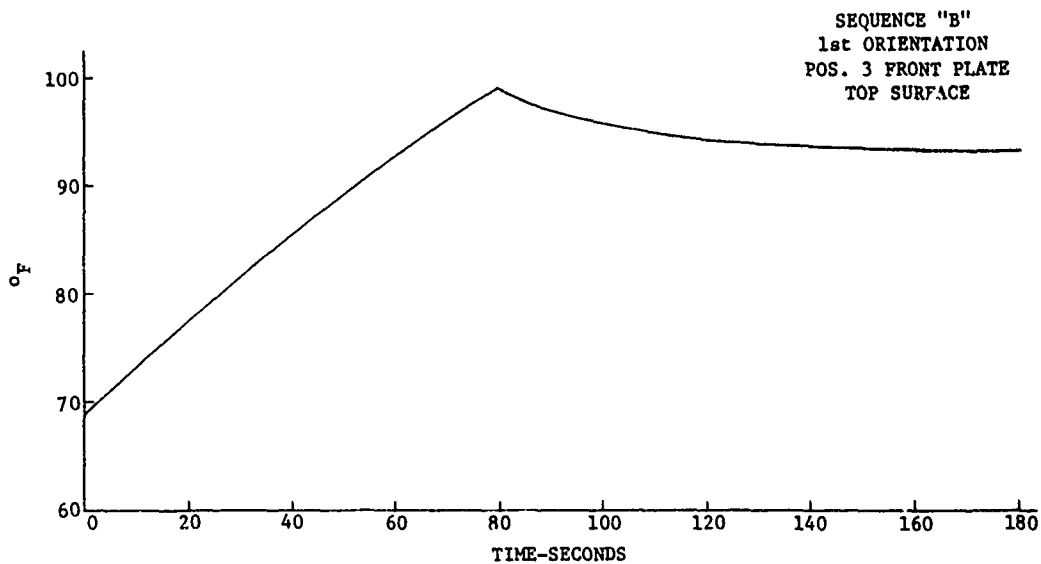


Figure B-3

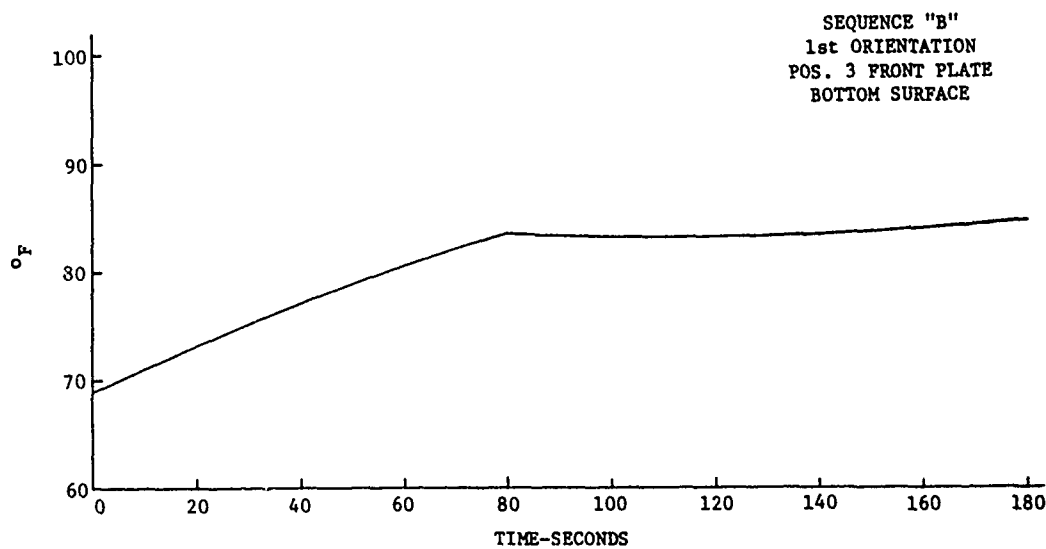


Figure B-4

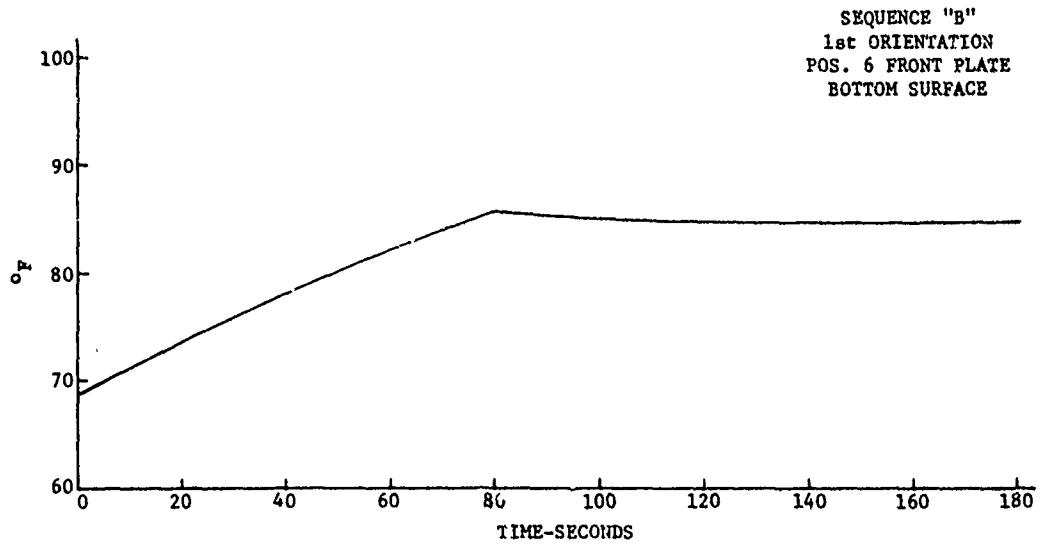


Figure B-5

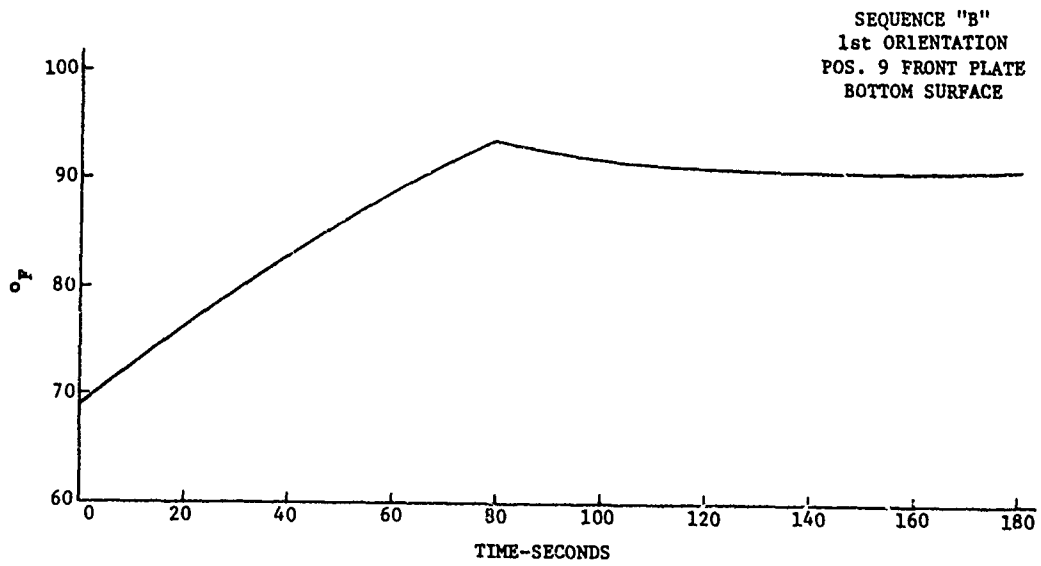


Figure B-6

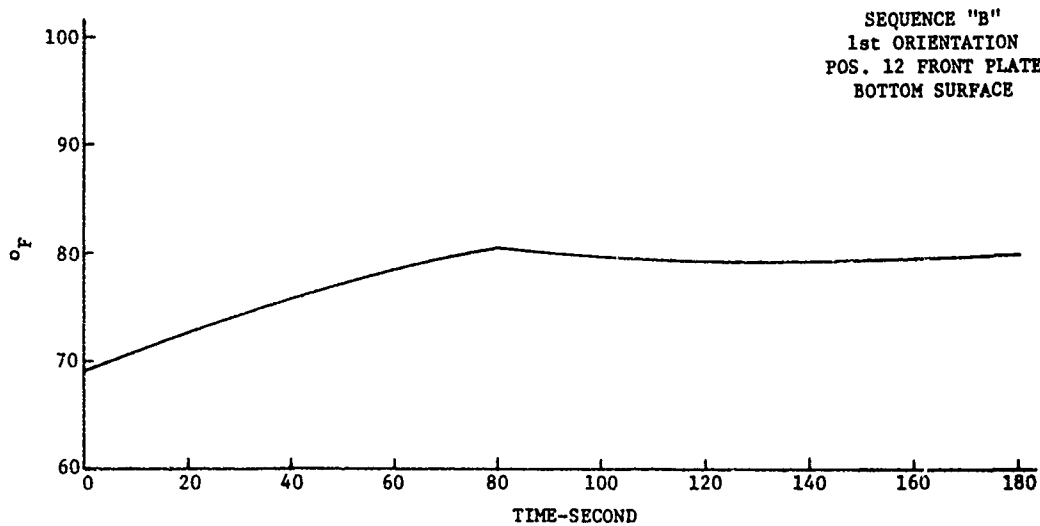


Figure B-7

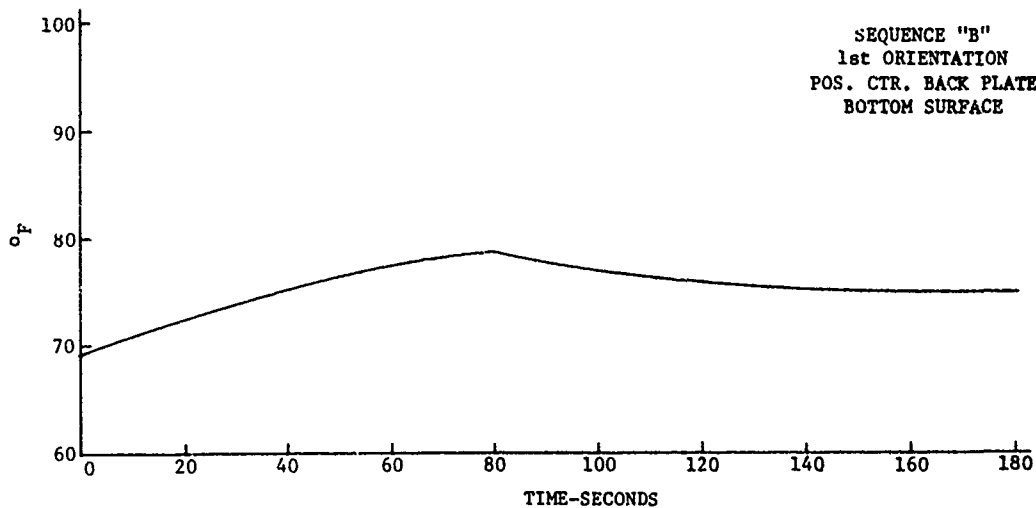


Figure B-8

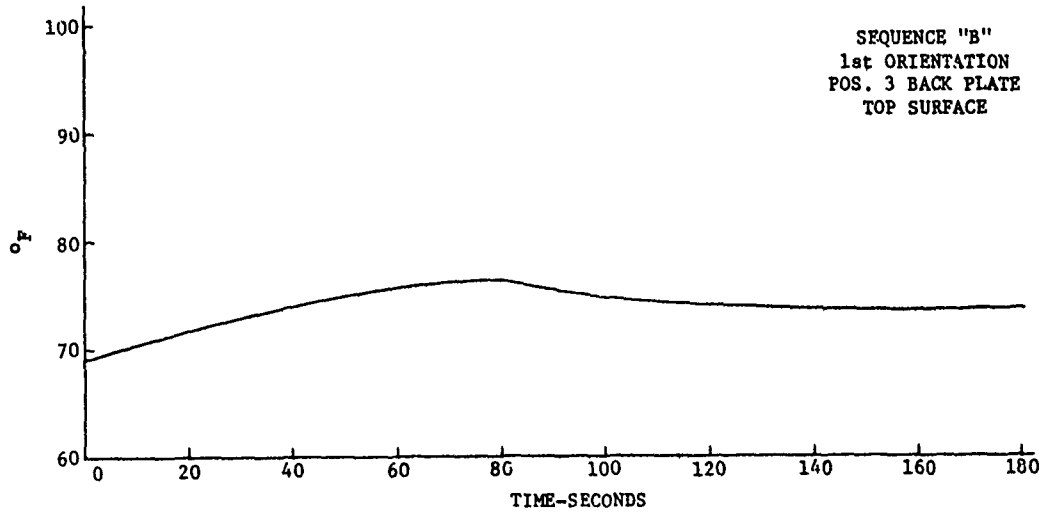


Figure B-9

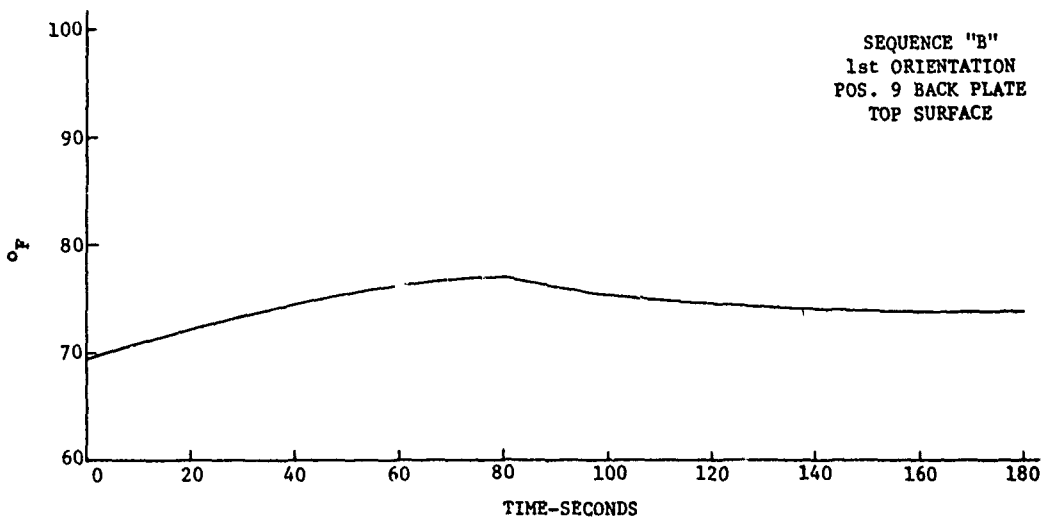


Figure B-10

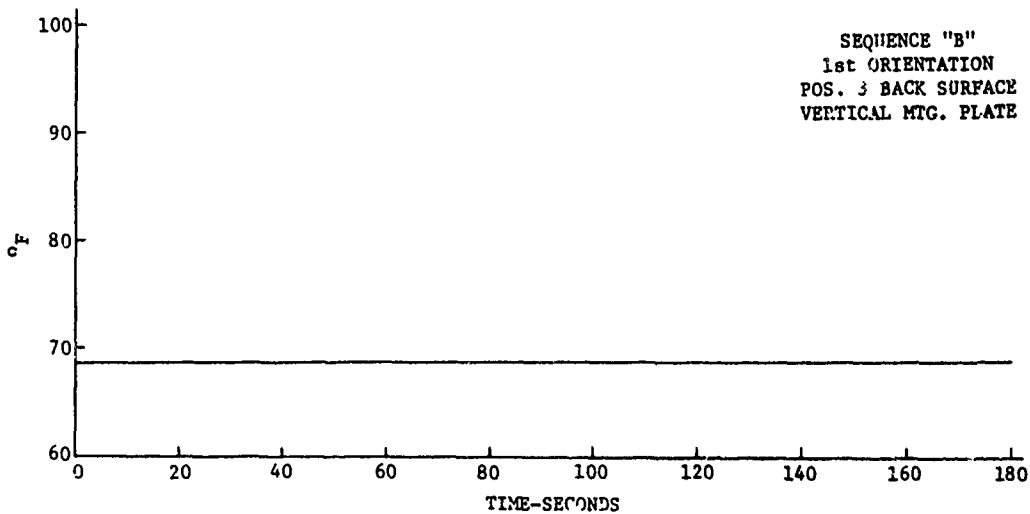


Figure B-11



Appendix C

Thermocouple Data

COMPOSITE AND INDIVIDUAL
2nd Orientation

IRRADIATION RESPONSE TESTS

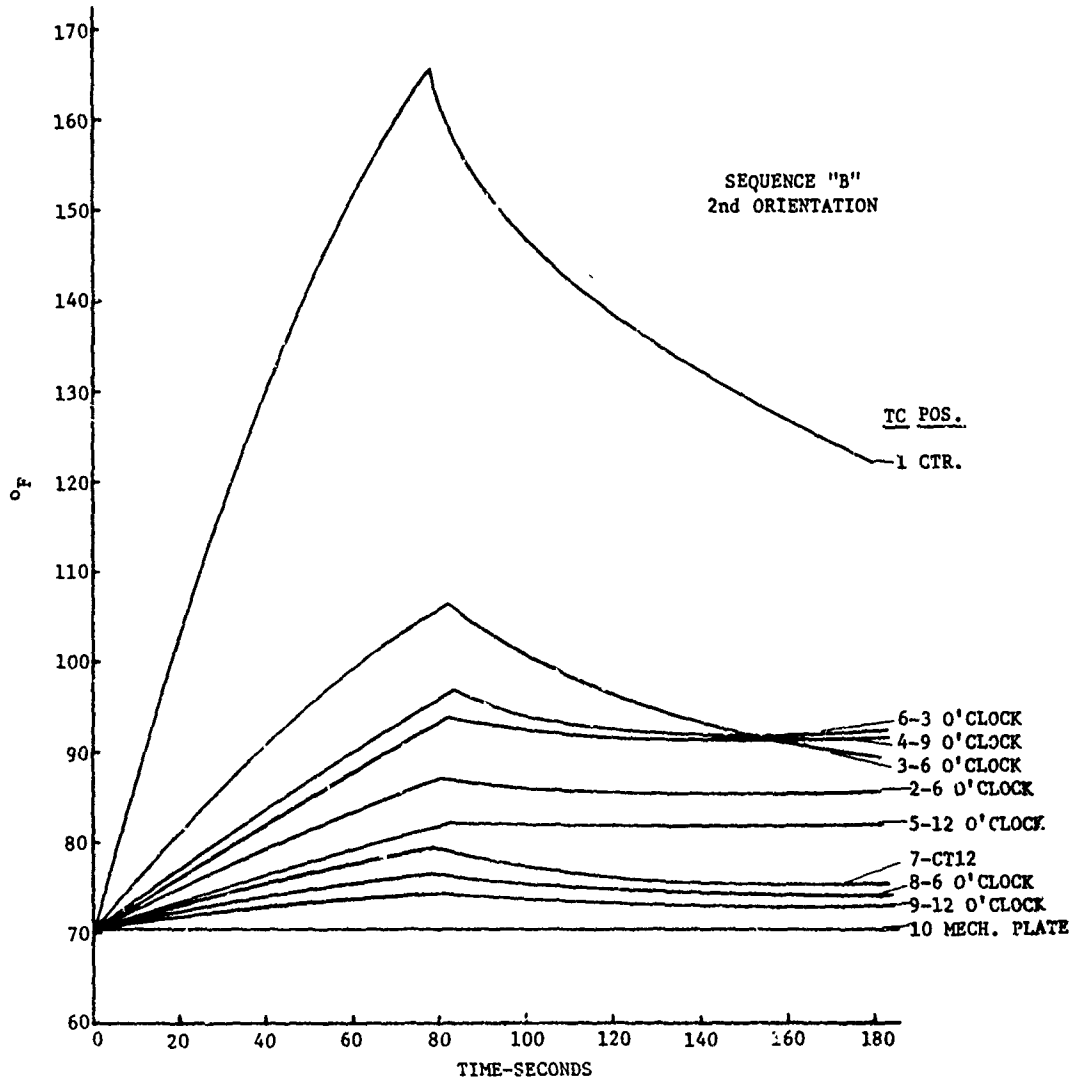


Figure C-1

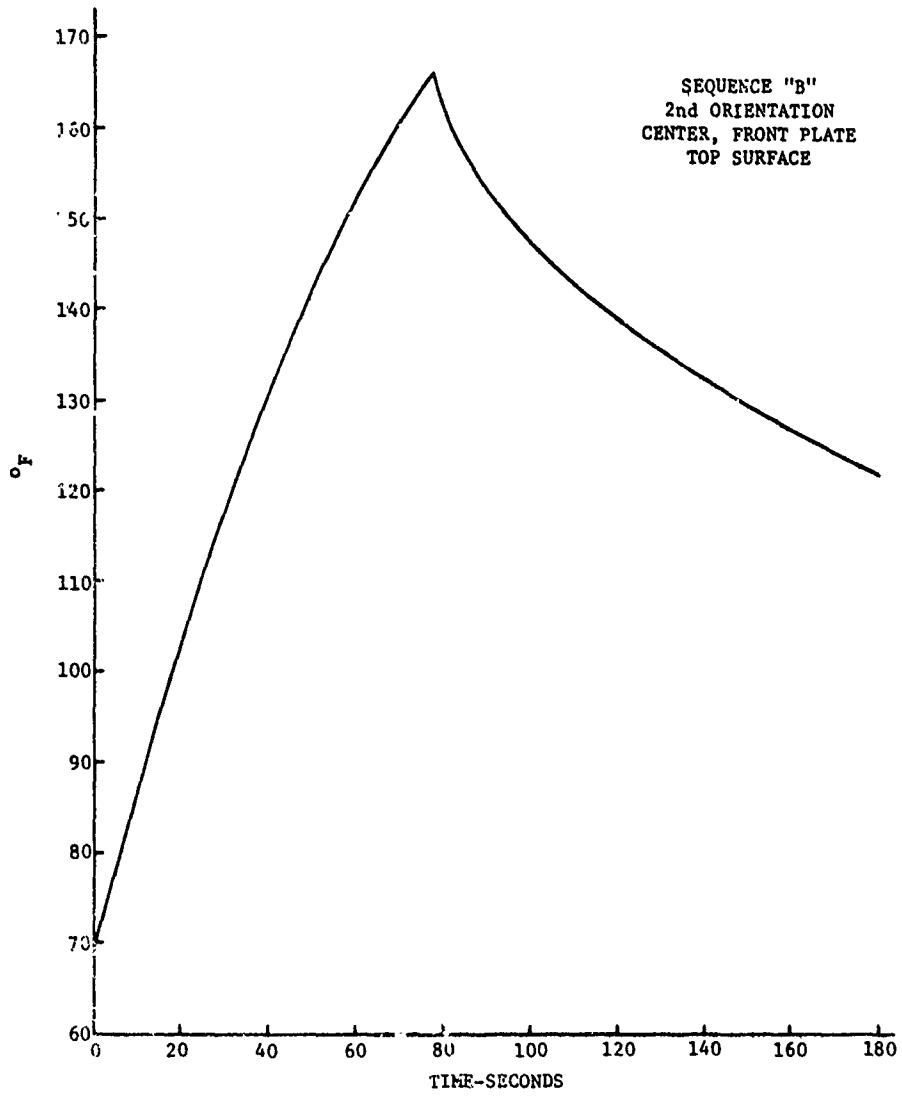


Figure C-2

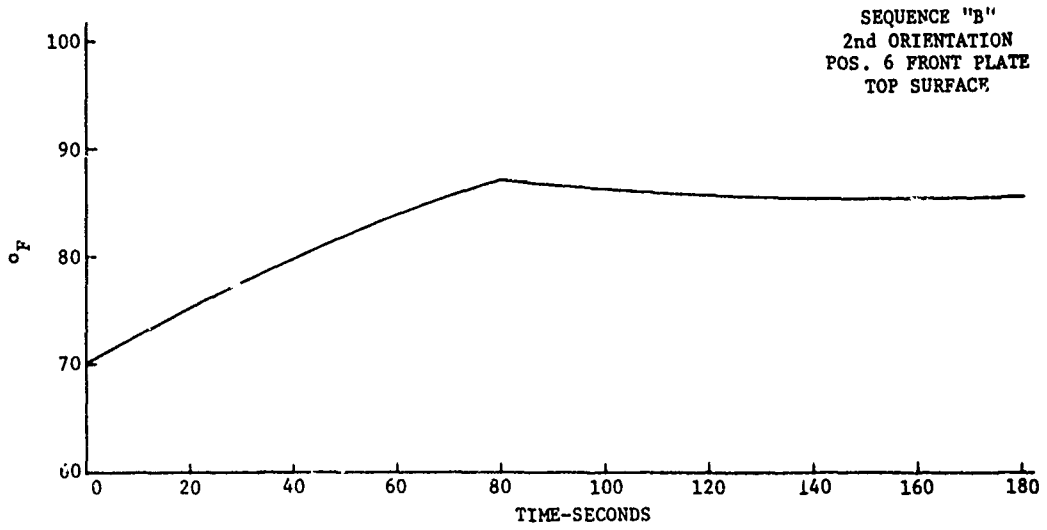


Figure C-3

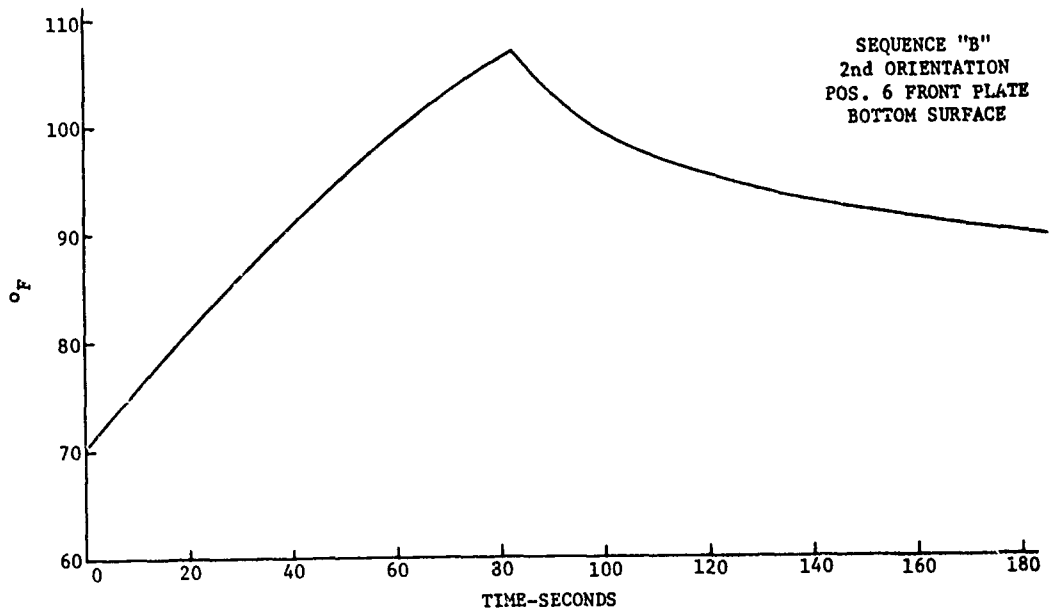


Figure C-4

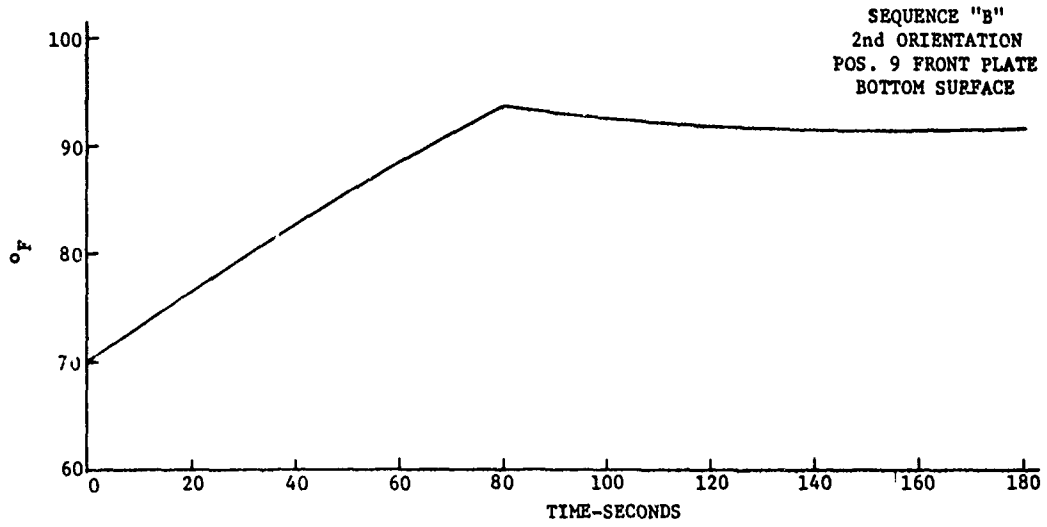


Figure C-5

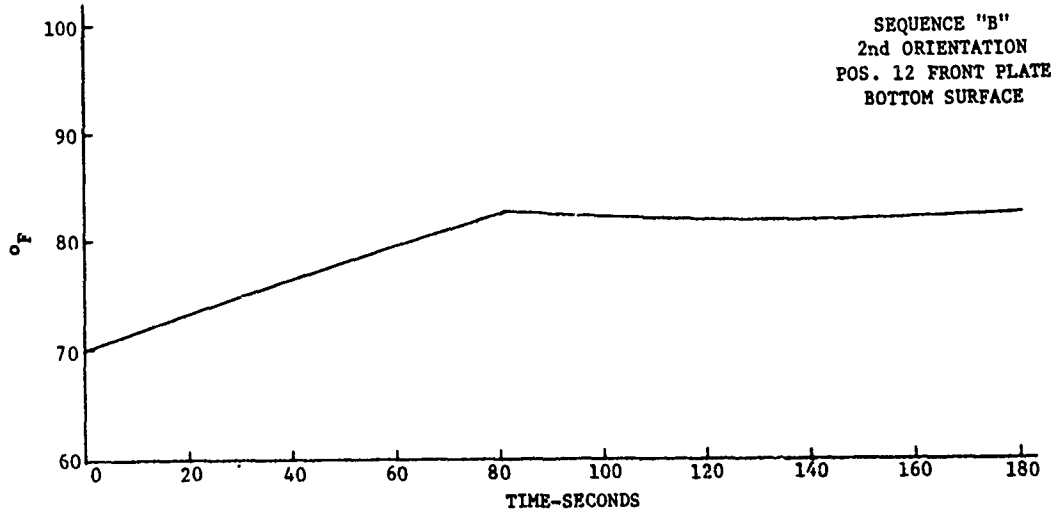


Figure C-6

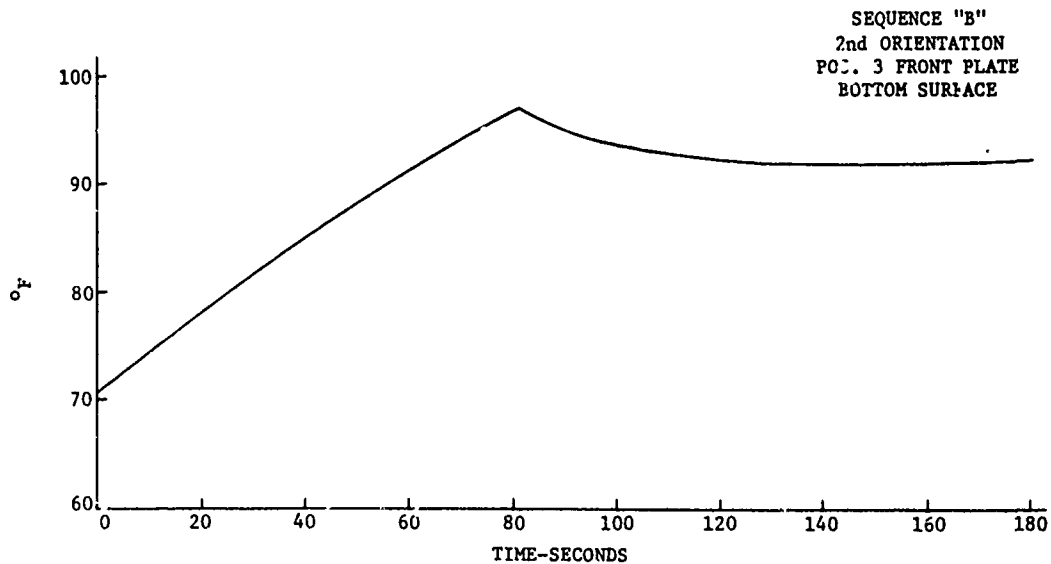


Figure C-7

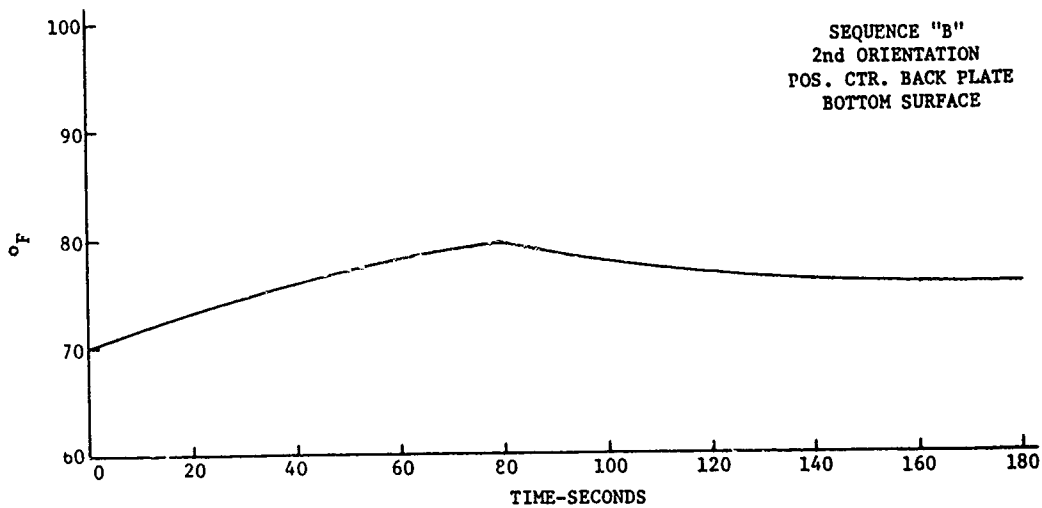


Figure C-8

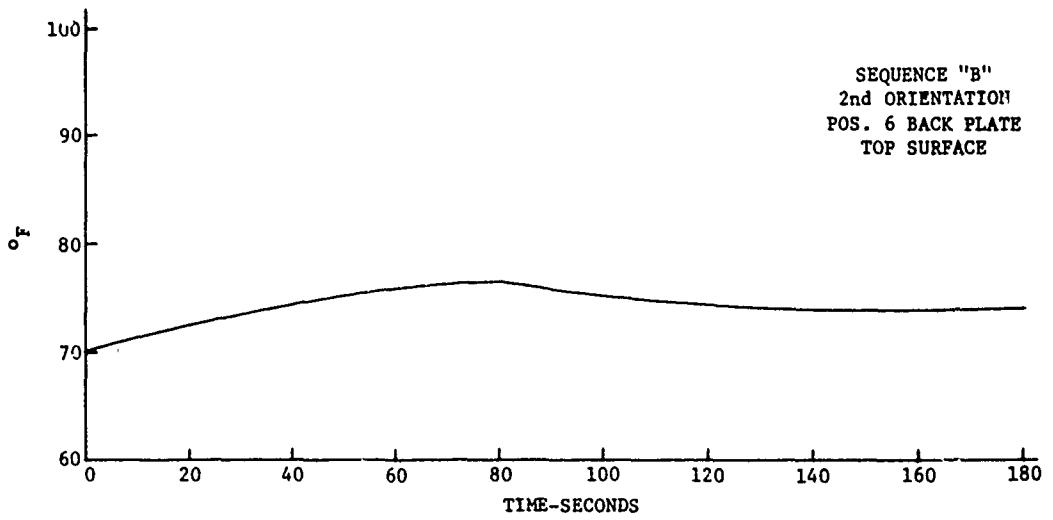


Figure C-9

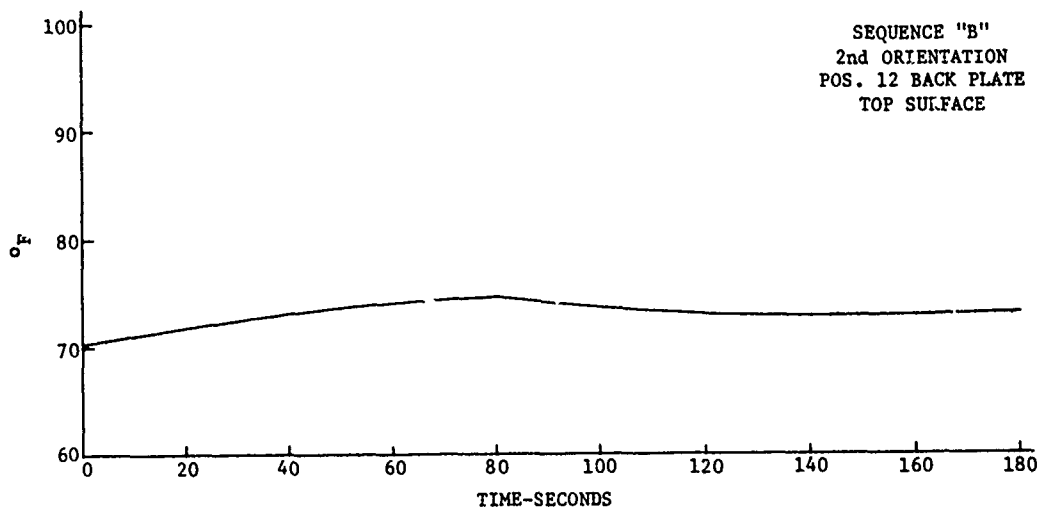


Figure C-10

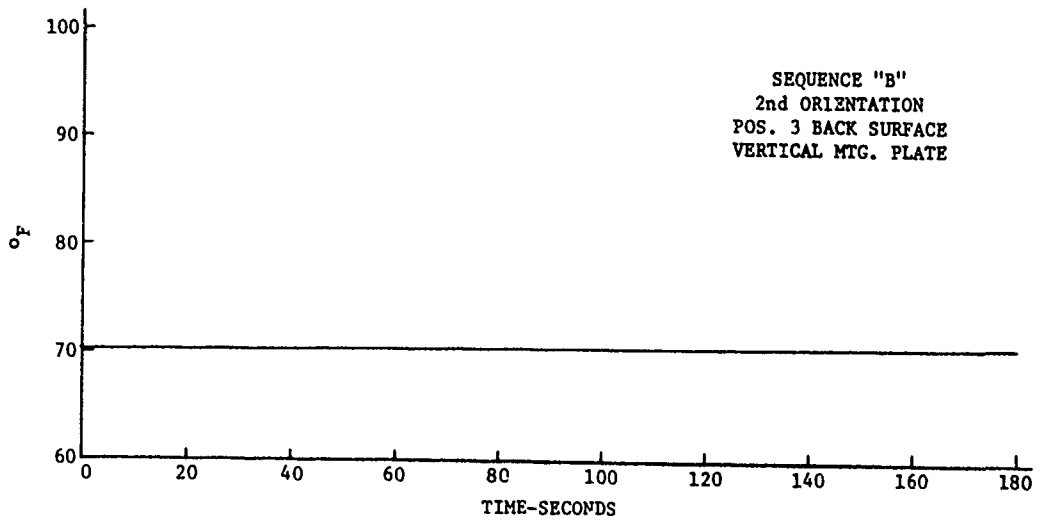


Figure C-11



Appendix D

Thermocouple Data

COMPARISON BY CLOCK POSITION

1st and 2nd Orientation

IRRADIATION RESPONSE TESTS

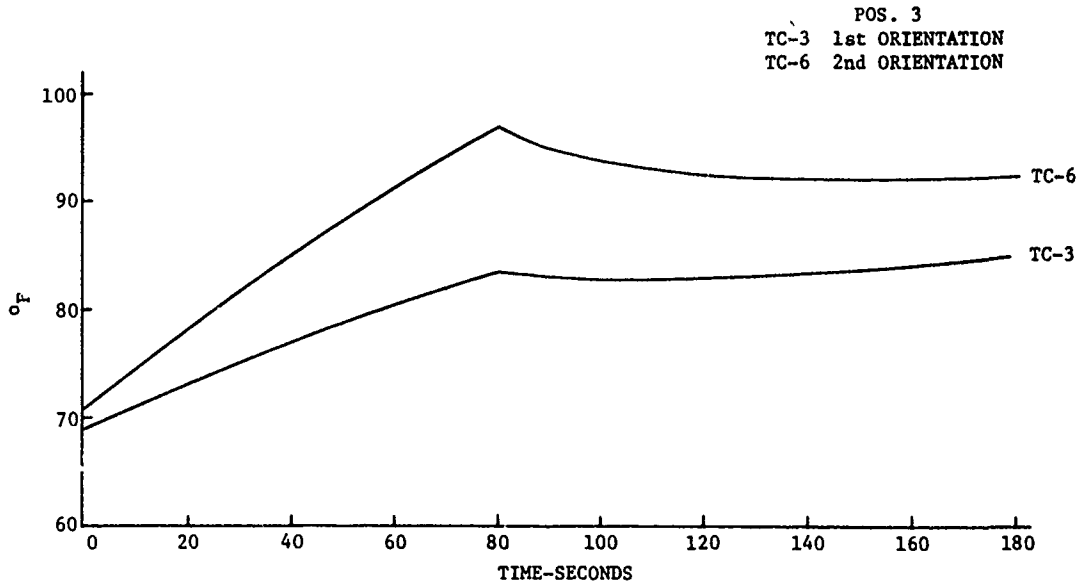


Figure D-1

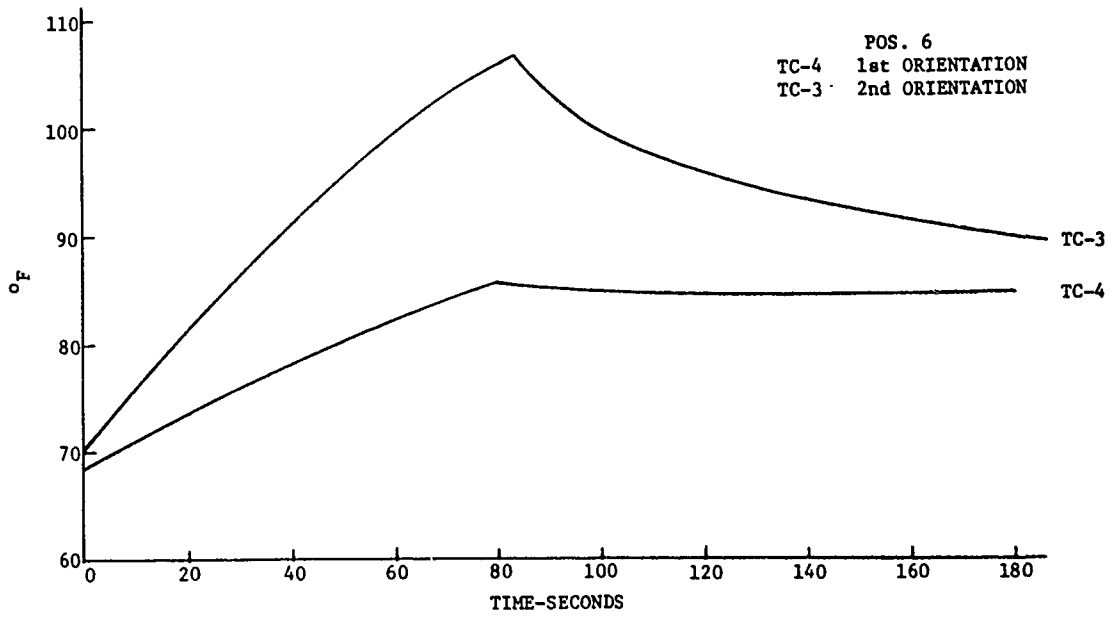


Figure D-2

RC-00348

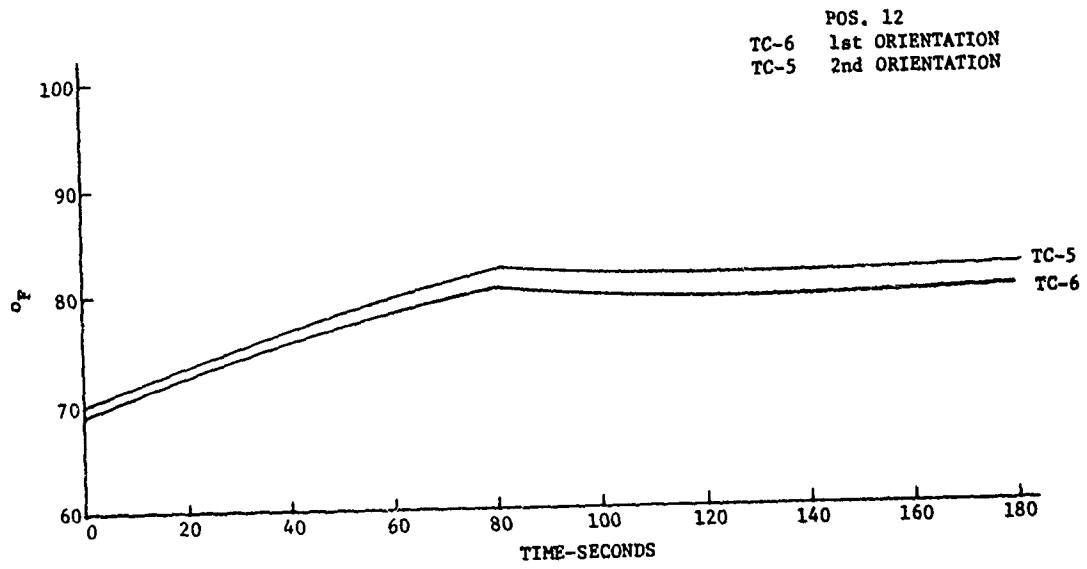


Figure D-3

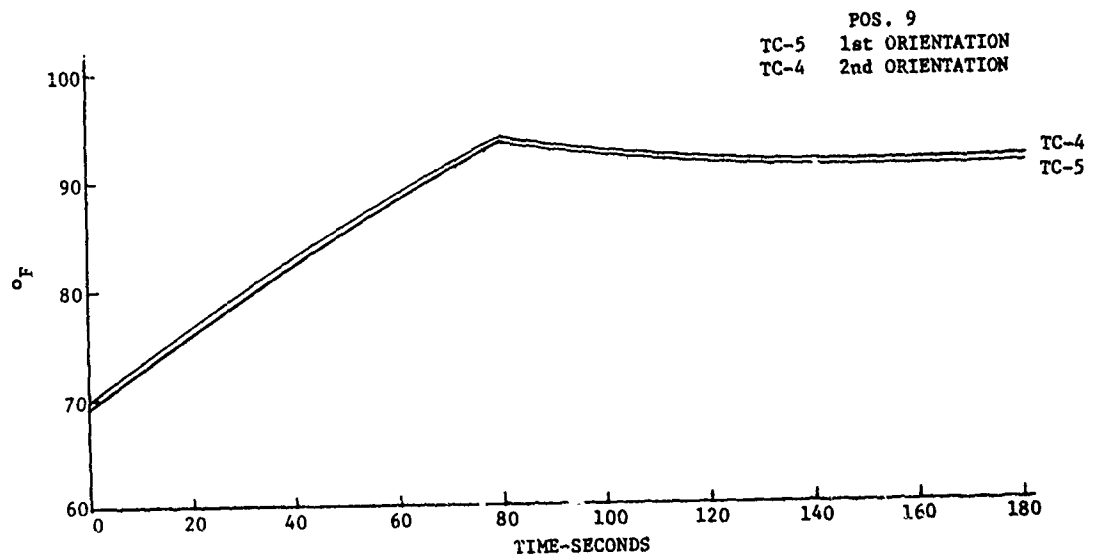


Figure D-4

Capt Doris Hamill RADC/OCSE	4	
RADC/TSLD GRIFFISS AFB NY 13441	1	2
RADC/DAP GRIFFISS AFB NY 13441	2	3
ADMINISTRATOR DEF TECH INF CTR ATTN: DTIC-DDA CAMERON SIA BG 5 ALEXANDRIA VA 22314	12	5
Eastman Kodak Co. Attn: I.C. Fitzsimmons Kodak Apparatus Division 901 Elmgrove Ave Rochester, NY 14050	5	3
AFWL/ALAO Attn: Dr. William Lowrey Kirtland AFB, NM 87117	1	4
AFWL/ARAA Attn: Dr. J. Fender Kirtland AFB, NM 87117	1	5
AFWL/ARAS Attn: Lt Col Paul Sovenkirk Kirtland AFB, NM 87117	1	6

The Aerospace Corp Attn: Dr. E.W. Silvertooth Bldg 110 MS 2339 PO Box 92957 Los Angeles, CA 90009	1	7
The Aerospace Corp Attn: J. Taylor Bldg 115 Room 1334C PO Box 92957 Los Angeles, CA 90009	1	8
Analytic Decisions Inc Attn: Emmanuel Golustein 1401 Wilson Blvd Arlington, VA 22209	1	9
BDA Corp Attn: William Gurley 1820 Randolph Rd Albuquerque, NM	1	10
BMD/ARC Attn: A. Carmichael PO Box 1500 Huntsville, AL 35807	1	11
Boeing Aerospace Co. Attn: B. Allasina PO Box 3999 Seattle, WA 98124	1	12
Charles Starke Draper Labs Attn: Frank Scammel 555 Technology Dr. Cambridge, MA 02139	1	13
Charles Starke Draper Labs Attn: Dr. Keto Soosar 555 Technology Dr MS 95 Cambridge, MA 02139	1	14

Corning Glass Works Attn: c.f. Decker Technical Products Division Corning, NY 14830	1	15
DARPA/DEO Attn: Col Ronald Prater Arlington, VA 22209	2	16
Eastman Kodak Attn: Robert Keim Kodak Aparatus Division 121 Lincoln Ave. Rochester, NY 14650	1	17
Eastman Kodak Attn: Richard Price KAD-Lincoln Park 901 Elmgrove RD Rochester, NY 14650	1	18
GRC Attn: G. Gurski 7655 Old Springhouse RD McLean, VA 22102	1	19
Hughes Aircraft Attn: Martin Flannery MS D/125 Bldg 6 Centenela & Teal Sts Culver City, CA 90230	1	20
Hughes Aircraft Attn: Dr Fred McClung MSo-E 125 Centenela & Teal Sts Culver City, CA 90230	1	21
Itek Corp Attn: Roland Plante Optical Systems Division 10 Maguire Rd. Lexington, MA 02173	1	22

Lockheed Palo Alto Research Lab Attn: Richard Feaster 0/52-03, B201 3251 Hanover St. Palo Alto, CA 94304	1	23
Lockheed Space and Missile Co. Attn: Dennis Aspinwall Dept 5203 Bldg. 201 3251 Hanover St. Palo Alto, CA 94304	1	24
Lockheed Space and Missile Co. Attn: Dick Wallner Dept 5203 Bldg 201 3251 Hanover St. Palo Alto, CA 94304	1	25
Martin Marietta Aerospace Attn: C.W. Spieth Denver Division PO Box 179 Denver, CO 80201		26
Denver Division PO Box 179 Denver, CO 80201	1	27
MIT/Lincoln Laboratory Attn: Alex Parker PO Box 73 Lexington, MA 02173	1	28
MRJ Corp Attn: Dr. Kenneth Robinson 71 Blake St. Needham, MA 02192	1	29
NASA Ames Attn: James Murphy MS 244-7 Moffett Field, CA 94035	1	30

NASA Marshall Space Flight Center Attn: Charles O. Jones Mail Code EC32 Huntsville, AL 35812	1	31
Naval Sea Systems Command Attn: Dr. Sadeg Siahatgar PMS-405 NC 1 Room 11N08 Washington, DC 20742	1	32
Naval weapons Center Attn: Dr. H. Bennett Code 0018 China Lake, CA 93555	1	33
Perkin Elmer Attn: Dr. David Dean MS 241 Main Ave Norwalk, CT 06856	1	34
Perkin Elmer Attn: Henry Dieselman 100 Wooster Heights Rd. Danbury, CT 06810	1	35
Rockwell International Attn: R. Brandenie Rocketdyne Division 6033 Canoga Ave Canoga Park, CA 91304	1	36
Rockwell International Attn: J. Murphy Space Division 12214 Lakewood Blvd Downey, CA 90241	1	37
Rockwell International Attn: R. Greenberg Space Division 12214 Lakewood Blvd Downey, CA 90241	1	38

Riverside Research Institute Attn: Dr. Robert Kappesser 1701 N Fort Myer Dr. Suite 711 Arlington, VA 22209	1	39
SD/YNS Attn: Col H.A. Shelton PO Box 92960 Worldway Postal Center Los Angeles, CA 90009	1	40
United Technologies Research Center Attn: Dr. J. Pearson Optics & Applied Technology Lab PO Box 2691 West Palm Beach, FL 33402	1	41
University of Arizona Attn: Prof Robert Shannon %Charles Peyton Administration Bldg Tucson, AZ 85721	1	42
W.J. Schaffer Assoc. Inc. Attn: Edward Borsare 10 Lakeside Office Park Wakefield, MA 01880	1	43